

AN INVESTIGATION OF THE ROLE OF SILICA SUBSTRATE  
TOPOGRAPHY ON THE TAILING AND BROADENING OF BASIC  
COMPOUNDS IN HPLC

by

Michael Antonio Legg

---

Copyright © Michael Antonio Legg 2007

A Thesis Submitted to the Faculty of the

DEPARTMENT OF CHEMISTRY

In Partial Fulfillment of the Requirements  
For the Degree of

DOCTOR OF PHILOSOPHY

In the Graduate College

THE UNIVERSITY OF ARIZONA

2007

THE UNIVERSITY OF ARIZONA  
GRADUATE COLLEGE

As members of the Dissertation Committee, we certify that we have read the dissertation prepared by Michael A. Legg entitled "An Investigation of the Role of Silica Substrate Topography on the Tailing and Broadening of Basic Compounds in HPLC" and recommend that it be accepted as fulfilling the dissertation requirement for the Degree of Doctor of Philosophy.

\_\_\_\_\_  
Mary J. Wirth

Date: 08/23/2007

\_\_\_\_\_  
John Enemark

Date: 08/23/2007

\_\_\_\_\_  
Eugene Mash

Date: 08/23/2007

\_\_\_\_\_  
Andrei Sanov

Date 08/23/2007

\_\_\_\_\_  
Mark Smith

Date 08/23/2007

Final approval and acceptance of this dissertation is contingent upon the candidate's submission of the final copies of the dissertation to the Graduate College.

I hereby certify that I have read this dissertation prepared under my direction and recommend that it be accepted as fulfilling the dissertation requirement.

\_\_\_\_\_  
Dissertation Director: Mary J. Wirth

Date: 08/23/2007

## STATEMENT BY AUTHOR

This dissertation has been submitted in partial fulfillment of requirements for an advanced degree at The University of Arizona and is deposited in the University Library to be made available to borrowers under rules of the Library.

Brief quotations from this dissertation are allowable without special permission, provided that accurate acknowledgment of source is made. Requests for permission for extended quotation from or reproduction of this manuscript in whole or in part may be granted by the copyright holder.

SIGNED: Michael A. Legg

## ACKNOWLEDGEMENTS

First and foremost, I must acknowledge and say thank you to my advisor, Dr. Mary J. Wirth. Mary took me in when I was a homeless physical chemist and provided the opportunity and equipment for me to pursue my Ph.D. in Chemistry. She introduced me to topics and ideas that I had thought that I had left behind and showed me that my gifts and interests could be applied to research topics that I had not previously considered.

I would also like to say thank you to all of the past and present members of the Wirth research group that I have worked with, post-docs, graduate students, and undergraduate students. I would especially like to acknowledge and thank Dr. Emily A. Smith and Dr. Takahira Tokimoto for training and working with me during my early days as a member of the group. Special acknowledgement must also go to Dr. Scott Long for providing me with some of the most enjoyable discussions I have ever had.

I must also thank and express my admiration and appreciation to Michael Flory and Stefanie Milam. Even though I did not remain a member of “Team Ziurys” I was always with you in spirit.

To all of those I have met and befriended during this journey but haven’t listed here, I would say thank you and wish you the best in your travels through life.

## DEDICATION

This dissertation is dedicated to my wife, Clarissa L. Embach. We met at the beginning of this journey, and I am happy and proud to have her with me here at the conclusion of this part of our lives.

The point of a journey is not to arrive.

## TABLE OF CONTENTS

LIST OF FIGURES .....	8
LIST OF TABLES .....	14
ABSTRACT .....	15
CHAPTER 1: INTRODUCTION AND OVERVIEW .....	17
Peak Tailing and Broadening of Basic Analytes in HPLC: .....	17
Chromatographic Separations: .....	21
Silica: .....	22
Modeling Chromatography: .....	24
CHAPTER 2: INSTRUMENTATION AND SPECIAL METHODS .....	25
Instrumentation: .....	25
Atomic Force Microscope: .....	25
Fourier Transform Infrared Spectrometer: .....	25
High Pressure Liquid Chromatograph: .....	26
UV-Vis Spectrophotometer: .....	26
Special Methods .....	26
Determination of Refractive Index of Silica Colloids: .....	26
Determining the Diameter of Silica Colloids Using AFM .....	36
Software Applications: .....	39
Gwyddion .....	39
ImageJ .....	39
CHAPTER 3: A REVIEW OF SINGLE-MOLECULE PROBING OF ADSORPTION AND DIFFUSION ON SILICA SURFACES .....	41
Introduction: .....	41
Chromatographic Silica Gel: .....	45
Single Molecule Measurement of Strong Adsorption: .....	53
Fused Silica versus Silica Gel .....	56
Kinetics .....	59
Topography .....	68
Conclusions: .....	72
CHAPTER 4: PROBING TOPOGRAPHY AND TAILING FOR COMMERCIAL STATIONARY PHASES USING AFM, FTIR, AND HPLC .....	73
Introduction .....	73
Sample Preparation: .....	75
Materials .....	75
FTIR .....	76
HPLC .....	76
Results and Discussion: .....	77
Conclusions .....	92
CHAPTER 5: SINTERED SILICA COLLOIDAL CRYSTALS WITH FULLY HYDROXYLATED SURFACES .....	95
Introduction: .....	95
Sample Preparation: .....	97

Results and Discussion: .....	98
Conclusions: .....	116
CHAPTER 6: DETERMINING THE TOPOGRAPHICAL AND CHEMICAL PROPERTIES OF NON-POROUS SILICA COLLOIDS USING AFM AND FTIR ...	117
Introduction: .....	117
Sample Preparation: .....	119
Silica Preparation: .....	120
Results and Discussionn: .....	122
Conclusion .....	139
CHAPTER 7: HIGH-SPEED ELECTROSEPARATIONS INSIDE SILICA COLLOIDAL CRYSTALS .....	140
Introduction: .....	140
Results and Discussion: .....	144
Conclusions: .....	150
REFERENCES .....	151

## LIST OF FIGURES

Figure 1-1	Schematic showing the isotherms for Fronting, Symmetric, and Tailing chromatographic peaks.	19
Figure 2-1	Calibration Curve of Refractive Index versus Volume Fraction of Toluene. The red line is the linear fit of the data, and the green lines are the 95th Percent Confidence Intervals.	29
Figure 2-2	Illustration showing the terms in Snell's Law and Fresnel's Transmission Equations. An incident beam strikes the interface between Medium 1 and Medium 2 and is refracted.	31
Figure 2-3	Theoretical Transmission calculated using the Fresnel Transmission Equation for light perpendicular to the sample.	34
Figure 2-4	Refractive index measurements for As Made, Calcinated, Sintered and Rehydroxylated silica colloids. The maximum %T for each of the samples is; As Made 1.454, Calcinated 1.439, Sintered 1.452, and Rehydroxylated 1.457.	35
Figure 2-5	A well-ordered region of an AFM image is rotated to provide a horizontal orientation of colloids and then cropped. This cropped region is analyzed using the ACF (autocorrelation) function in Gwyddion. The average peak-to-peak distance for several such measurements is taken to be the colloid diameter.	38
Figure 3-1	(a) Spectra for single molecules of pentacene in p-terphenyl as a function of time, illustrating spectral diffusion. (b) Intensities of single pentacene molecules in p-terphenyl as a function of time, illustrating kinetics of spectral diffusion.	42
Figure 3-2	Bursts from single molecules of fluorescein diffusing rapidly through a laser beam and detected by confocal microscopy: (a) emission from the solvent blank and (b) emission from a solution of $3 \times 10^{-10}$ -M fluorescein in water.	46



## LIST OF FIGURES – CONTINUED

Figure 3-3	(Top panel ) Schematic representation of an idealized, fully silylated silica surface and the resulting idealized chromatogram. (Bottom panel) The more realistic surface and chromatogram.	48
Figure 3-4	(a) The infrared spectra in the O-H stretching region for HF-treated versus -untreated silica gels. The inset shows spectra on an expanded scale. (b) Chromatograms for HF-treated versus-untreated silica gels for compound 2 (N,N-diethylaniline).	52
Figure 3-5	Single-molecule burst data showing many diffusion events and one strong adsorption event. The many diffusion events produce the sharp spikes. The strong adsorption event started at 888 s.	55
Figure 3-6	Chromatograms of DiI at two different pH values, illustrating how peak asymmetry and broadening typically depend on pH. The inset shows the molecular structure of DiI(C12).	57
Figure 3-7	Schematic of adsorption and desorption events in single-molecule spectroscopy. The interval between adsorption events and the duration of adsorption events both fluctuate randomly from one event to the next, in accordance with Poisson statistics.	61
Figure 3-8	(a) Cumulative fluorescence micrograph of a silylated fused silica surface. Bright spots are labeled 1–6. (b) Intensity as a function of time for two positions in the image: red trace, position of spot 1; blue trace, a position a few pixels away. (c) Analogous trace for spot 2. Numbers separated by commas in b and c refer to pixel position.	67
Figure 3-9	(a) Atomic force microscope (AFM) image and (b) fluorescence micrograph of the same region of a silylated fused silica coverslip in contact with dilute DiI solution.	69

## LIST OF FIGURES – CONTINUED

Figure 3-10	Atomic force microscopy data from Agilent's Zorbax RX silica gel. (a) The three micrographs show the 5- $\mu$ m bulk particles on three scales: 7 $\mu$ m, 1 $\mu$ m, and 100 nm. The black line on the image, drawn through a plateau, for the 100-nm scale corresponds to the height profile shown in b).	71
Figure 4-1	AFM images of each of the three materials on scales ranging over three orders of magnitude: a) Zorbax SB300, b) Symmetry 300, and c) Chromolith. The scan size and z-scales are indicated in each panel.	78
Figure 4-2	Line scans for each of the three materials. These correspond to the line segments in Figure 4-1 in the right-most panel of each series. The traces are artificially offset to facilitate comparison.	80
Figure 4-3	Normalized Diffuse Reflectance Infrared Fourier Transform (DRIFT) spectra of each of the three materials after removing them from their columns and drying them under vacuum. Each spectrum is scaled to account for surface C18 coverage and then normalized using the Symmetry methylene stretch peak intensity.	83
Figure 4-4	Chromatograms for DiI at varying concentration from 1 to 300 mM for three columns: a) Zorbax SB300 (L=15 cm), b) Symmetry 300 (L=5 cm), and c) Chromolith (L=2.5 cm). The mobile phase was 90% acetonitrile/10% water with 0.1% TFA and 0.01 M KCl. The column temperature was 20 °C. Experimental chromatograms are in blue and simulated chromatograms are in red.	85
Figure 4-5	Rescaled chromatograms from Figure 4-4 for the lowest concentration of DiI, 1 mM, for each for the three columns: a) Zorbax SB300, b) Symmetry 300, and c) Chromolith. A dashed line is drawn through the peak to illustrate peak symmetry.	86

## LIST OF FIGURES – CONTINUED

Figure 5-1	Optical micrographs of a) sintered silica colloidal crystal with three prior calcinations steps, and b) colloidal crystal with neither calcinations nor sintering, shown to illustrate cracks.	100
Figure 5-2	FTIR spectra of silica colloidal crystals made using particles with no calcination (As-Made), using calcined particles, and using calcined particles that were sintered after the crystal was formed.	101
Figure 5-3	SEM images of colloidal crystal made from a) As Made particles, and b) Calcined particles. The arrow size is the same in each panel to indicate that the particles in panel b are smaller.	105
Figure 5-4	Optical transmission measured at 589 nm for colloid slurries as a function of the refractive index of the solvent used for the slurry. Four different preparations of particles were studied, as denoted by the labels in the inset.	106
Figure 5-5	Field-emission SEM micrographs of a sintered silica colloidal crystal showing the attachment points after breaking the crystal.	107
Figure 5-6	Transmission spectra of silica colloidal crystals, including as-made, calcined and sintered, as indicated. The positions of the Bragg peaks are given.	110
Figure 5-7	SEM images at two different magnifications for a sintered colloidal crystal snapped in half. a) higher magnification to show the crystal planes, b) lower magnification to show the outlines of domain boundaries.	111
Figure 5-8	Infrared spectra for a colloidal crystal after sintering, after rehydroxylation, and after growth of a polyacrylamide brush layer, as labeled.	112
Figure 5-9	UV-visible transmission spectra for a colloidal crystal after sintering (solid line), after base treatment to rehydroxylate the surface (dashed line) and after growth of a polyacrylamide brush layer (dotted line). The small spikes, e.g., at 490 nm, are artifacts.	115

## LIST OF FIGURES – CONTINUED

Figure 6-1	AFM images of each of the three samples on scales ranging over three orders of magnitude: As Made, C3X, and Sintered. The scan size and z-scales are indicated in each panel.	125
Figure 6-2	FTIR spectra of As Made, C3X, Sintered, and Rehydroxylated silica sample showing a broad water peak at approximately 3400 $\text{cm}^{-1}$ , a broad associated silanol peak at approximately 3600 $\text{cm}^{-1}$ , and much narrower isolated silanol peak at approximately 3745 $\text{cm}^{-1}$ .	128
Figure 6-3	Expanded scale of figure 6-2 showing isolated and associates silanol peaks for As Made, C3X, Sintered, and Rehydroxylated sample.	129
Figure 6-4	Adhesive force measurement data for rehydroxylated silica colloids that had been sintered for 3 hours and 6 hours. Images a) and c) show the histograms for the raw measurement data for the 3 hour and 6 hours sintering respectively. Images b) and d) show histograms for the number of bonds formed between the AFM probe and the silica surface. The average number of bonds assumes a single bond adhesive strength of 248 pN for the 3 hour sintering sample and 174 pN for the sample sintered for 6 hours.	133
Figure 6-5	Isolated silanol spectra for samples with sintering times ranging from 0 – 9 hours. All samples were ramped from room temperature to 900 °C at 10 °C/min and held at that temperature for the time indicated before cooling to room temperature. Increased sintering time leads to a smaller isolated silanol peak.	135
Figure 6-6	Graph showing the %Transmission at 589 nm versus hours of sintering for silica colloids in a solvent with a refractive index of 1.454. This is the refractive index of fully sintered silica colloids as reported in Chapter 5. As the refractive index of the colloids approaches that of the solvent, the %Transmission approaches 100.	138

## LIST OF FIGURES – CONTINUED

Figure 7-1	Schematic. The crystal was covered tightly with a 5 mm thick PDMS sheet, into which holes for reservoirs were cut. The insert is an AFM image of the 200 nm silica spheres. An inverted fluorescence microscope monitored the migration of the dyes.	142
Figure 7-2	Separation of three DiIs through 1 mm of colloidal crystal using 90:10 MeOH:water, 0.1% TFA, and a field strength of 1000 V/cm.	143
Figure 7-3	van Deemter plots for Merck Chromolith (î) and the colloidal crystal (ç). The same mobile phase was used as for Figure 7-2.	147
Figure 7-4	Separation by (a) HPLC and (b) the silica colloidal crystal of three peptides whose structures are shown to the right. The same mobile phase as in Figure 7-2 was used for both separations.	148

## LIST OF TABLES

Table 4-1	Summary of parameters from HPLC, FTIR and AFM. From HPLC, the surface density of strong adsorption sites and $K_s$ is the partition coefficient for adsorption to the strong sites. The relative absorbance from FTIR at $3735\text{ cm}^{-1}$ corresponds to the isolated silanols. The AFM data include fractal dimension and force of adhesion, where the average ( $\bar{x}$ ), standard deviation ( $s$ ), and number of measurements ( $N$ ) are listed.	94
Figure 5-1	Summary of data for particles after the indicated treatment.	104
Figure 6-1	Summary of statistics for As Made, C3X, and Sintered particles. The AFM data include particle diameter and force of adhesion. This data is given with at the 95th percent confidence interval. The FTIR data shows frequency and abundance of isolated silanols relative to the associated silanol peak maximum near $3660\text{ cm}^{-1}$ .	126

## ABSTRACT

Atomic force microscopy, Fourier transform infrared spectroscopy, high performance liquid chromatography, and UV-vis spectroscopy were used to study commercial and locally produced chromatographic silica substrates. Previous work has correlated the presence of isolated silanols with the peak tailing and broadening of basic analytes, and studies have shown enhanced adsorption of these analytes to isolated silanols at topographic features on planar, fused silica coverslips. This work provides evidence that similar topographical features exist on chromatographic substrates.

This work is the first, to our knowledge, to provide nanoscale, topographic data on commercial silica. Three products; by Agilent, Merck, and Waters all have surface features that are similar in size and shape to the features on planar coverslips. The Agilent product also has seams where the individual colloids are fused together to form the bulk particle. These seams may not be fully silylated due to steric hindrance. Neglecting these features, the bulk of the silica surface is as smooth as fused silica.

The AFM, FTIR, and HPLC data all indicate that the Waters silica had roughly twice the abundance of isolated silanols as the Merck product. The HPLC data for the Agilent material exhibited fronting and could not be modeled, but the FTIR data indicated that it had the same isolated silanol abundance as the Merck product.

These same methods were used to characterize nonporous silica particles produced in our laboratory to be used as substrates for a variety of separation techniques. From the initial silica particles to the final colloidal crystal, AFM, FTIR, and UV-Vis data used to characterize these materials is presented. A method to determine the refractive index of

the silica particles was developed and the changes in refractive index as the material is processed are also shown.

Separation of three dye species and another separation of three peptide chains was done on a 2D colloidal crystal of these silica particles. The colloidal crystal outperformed a commercial, silica monolithic product both in terms of peak asymmetry and in resolving the analytes. This preliminary work shows the promise of this material as a substrate for chromatographic separations.



## CHAPTER 1: INTRODUCTION AND OVERVIEW

### Peak Tailing and Broadening of Basic Analytes in HPLC:

Chromatographic peak tailing and broadening, especially for basic solutes, has been a problem since the advent of reversed phase liquid chromatography. Illustrating that this is a long standing issue, this concentration dependent tailing and broadening on a saturated column can be seen in Karger's 1973 textbook<sup>1</sup>. Within a few years of the availability of a commercial liquid chromatograph, it was being used in the pharmaceutical industry for separations and quantitative analysis<sup>2</sup>. Because HPLC has become such a widely used analytical technique within the pharmaceutical industry, this issue is an especially pressing problem because an estimated 85% of drugs have basic functional groups<sup>3</sup>. Neglecting issues external to the chromatographic column itself or voids or irregularities in the packing material, it is the shape of the adsorption isotherm that determines the chromatographic peak shape. Peak tailing occurs when surface sites become saturated, at which point, the analyte concentration in the stationary phase can no longer increase linearly with increasing concentration in the mobile phase. Peak fronting occurs when there is a disproportionate increase in surface concentration with increasing analyte concentration in the mobile phase, and this occurs when the analytes interact attractively with one another. Symmetric peaks occur when the analyte concentration in the stationary phase is linearly proportional to the concentration in the mobile phase.

This concept is illustrated by an isotherm, where the concentration of analyte in the stationary phase is plotted as a function of the analyte concentration in the mobile phase. The three cases; symmetric, fronting, and tailing are shown in Figure 1-1.

This phenomenon of peak tailing has been extensively studied<sup>3-8</sup> and is caused by mixed mode retention where rare, strong adsorption sites become saturated at low analyte concentration and produce an isotherm where surface concentration is no longer a linear function of the mobile phase concentration. This effect can be described using the bi-Langmuir isotherm shown in Equation 1-1.

$$\Gamma = \Gamma_{sat,weak} \cdot \frac{K_{weak} \cdot c}{1 + K_{weak} \cdot c} + \Gamma_{sat,strong} \cdot \frac{K_{strong} \cdot c}{1 + K_{strong} \cdot c} \quad (1-1)$$

The mobile phase and stationary phase analyte concentrations are  $c$  and  $\Gamma$ , and  $\Gamma_{sat,weak}$  and  $\Gamma_{sat,strong}$  are the number of intended, weak and unintended, strong absorption sites respectively. As long as  $K \cdot c \ll 1$  for both the strong and weak sites, the denominator in both terms are effectively equal to 1, and the surface concentration is a linear function of the mobile phase concentration, that is:

$$\Gamma = (\Gamma_{sat,weak} \cdot K_{weak} + \Gamma_{sat,strong} \cdot K_{strong}) \cdot c.$$

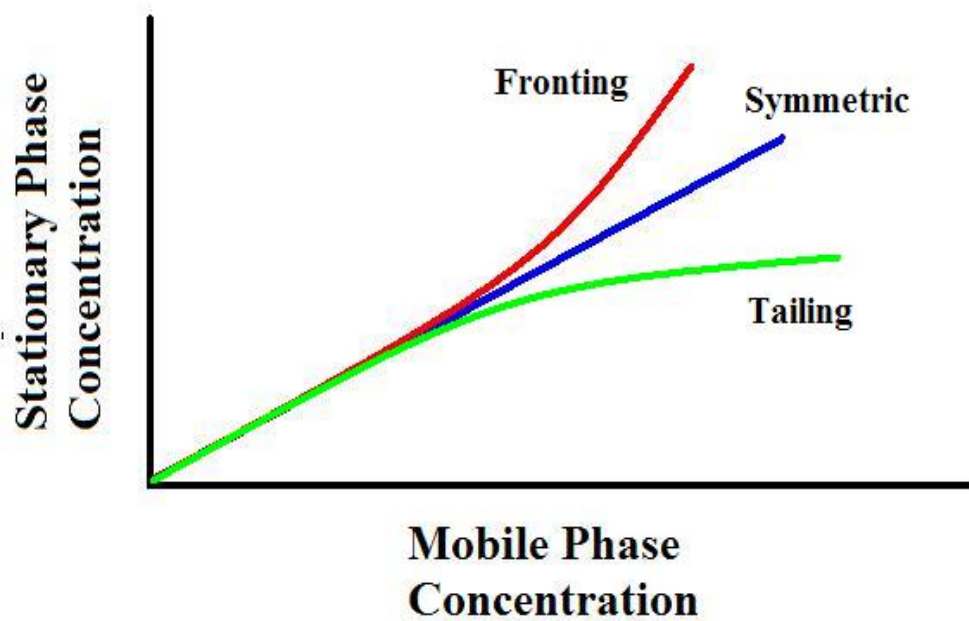


Figure 1-1 Schematic showing the isotherms for Fronting, Symmetric, and Tailing chromatographic peaks.

Mixed mode retention leads to peak broadening and tailing. In the ideal case, there is only a single possible interaction and that is between the analyte and the C18 alkyl chain attached to the silica surface. This is the desired, “weak” interaction in Eq 1-1, but this situation is not what occurs in reality. Unreacted silanols remain on the surface regardless of efforts to completely remove them. If the remaining silanols are isolated, they do not share hydrogen bonds with other nearby silanols, they provide a second adsorption site for the analytes, and the hydrogen bonding between these isolated silanols and basic analytes is stronger than the interaction between the C18 chains and the analyte. It is this second, undesired, strong interaction that leads to the tailing of basic analytes. The causes and effects of mixed mode retention are discussed in greater depth in Chapter 3.

Surface features and topography have been investigated as a possible source of isolated silanols. By comparing atomic force and fluorescent microscopy data of the same region of a planar, C18 modified fused silica surface, Wirth and coworkers showed that a cationic fluorescent dye, 1,1'-didodecyl-3,3,3',3'-tetramethylindocarbocyanine perchlorate (hereafter referred to as simply DiI), adsorbed strongly at topographical features such as lines and pits, suggesting that isolated silanols correlated with irregular topographic features<sup>9</sup>. In our work on commercial silica products, we concluded that isolated silanols were likely hidden in seams between the ~100 nm silica colloids that combine to form the micron sized silica gel particles and in nanometer scale basins and plateaus on the silica surface<sup>10</sup>. This work is discussed in detail in Chapter 4. Kamiya et. al. used FTIR to show the effect of particle size on silica<sup>11</sup>. As the particles decrease in

diameter, the isolated silanol peak, which is not present at all in the spectrum of 230 nm particles, increases until it is very prominent in the 8 nm particle spectrum. These works provide evidence that surface topography plays an important role in the formation of isolated silanols.

#### Chromatographic Separations:

Russian botanist, Mikhail Tswett began the development of chromatographic separations in the early years of the twentieth century. In an effort to separate the green chlorophylls from the yellow carotenoids, he dissolved a sample in a small amount of organic solvent and placed it at the top of a column filled with powdered calcium carbonate. He washed the sample through the column by adding fresh solvent at the top while letting solvent drip out of the bottom of the column.

This type of chromatographic separation is achieved because the solutes partition between the stationary and mobile phases, and the partitioning is not the same for each solute. A solute that preferentially partitions into the mobile phase will move down the column faster than one that spends more time adsorbed to the stationary phase, so it will exit the bottom of the column first. As Tswett's sample moved through the column, the different components separated into distinct bands; and it was because of these colored bands that he called this technique "chromatography."

Normal phase chromatography is the name given to Tswett's original system of a polar stationary phase and a non-polar mobile phase, and reversed phase liquid chromatography is the term applied to a system with a non-polar stationary phase and a polar mobile phase. Reversed phase liquid chromatography is used almost exclusively

today since polar solvents produce faster elution times, polar contaminants in the solute do not have as great an effect, and tailing is greatly reduced because strongly polar moieties, such as hydroxyls, on the stationary substrate are blocked by the non-polar alkyl chains attached to the surface.

The history and development of chromatography is detailed in Ettre and Zlatkis's, *75 Years of Chromatography: A Historical Dialogue*<sup>12</sup> and shorter history can be found in Scott's *Techniques and Practice of Chromatography*<sup>13</sup>. A detailed description of the mathematics and thermodynamics behind chromatographic separations can be found in Giddings's book *Unified Separation Science*<sup>14</sup>.

Silica:

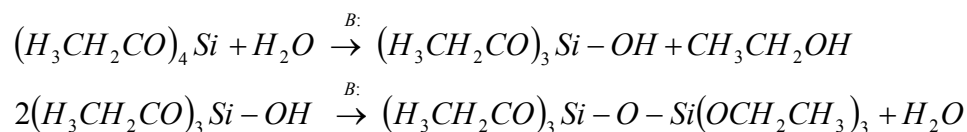
Silica is the most abundant compound in the Earth's crust<sup>15</sup>, and its importance to mankind can hardly be overstated. Wikipedia's list of applications where silica is used include: manufacturing glass for windows, silica gel for desiccants, ceramics such as porcelain, the NASA space shuttle's heat protection tiles, and glass fiber optic cables among other uses<sup>16</sup>.

In 1968, Stöber, Fink, and Bohn<sup>17</sup> introduced a solution based method to make monodisperse silica particles ranging in size from 0.050 to 2.0  $\mu\text{m}$ . The method involved the hydrolysis of alkyl silicates followed by the condensation of silicic acid in an alcoholic solution. The initial concentrations of the starting materials; a tetraalkyl silicate, tetraethoxysilane (TEOS) for example, an alcohol such as ethanol, ammonia or ammonium, and water determined the resulting particle diameter. In 1988, Bogush, Tracy, and Zukoski<sup>18</sup> expanded on the work of Stöber, Fink, and Bohn. They claimed

that at  $T = 25\text{ }^{\circ}\text{C}$ , the upper limit of the Stöber method was particles 800 nm in diameter, and monodispersity was difficult to maintain as the particles neared this upper limit. Bogush and coworkers developed a “seeded growth” technique that could be used to create particles between 1 and 2  $\mu\text{m}$ , with high monodispersity, by adding additional TEOS and water in a 1:2 mole ratio. In 2005, Nozawa and coworkers<sup>19</sup> made another improvement on the Stöber-Fink process by using a single recipe and controlling particle size with the rate at which reactants are added together rather than the initial concentrations of the reactants.

All of these methods are a combination of base catalyzed hydrolysis and condensation reactions. The initial step is the conversion of an ethoxy group on the silane to an alcohol. This is followed by conversion of  $-\text{OH}$  groups on adjacent silanes to siloxane bonds, linking the two monomers. As these steps continue, the siloxane lattice continues to grow and bulk silica particles are formed.

These steps can be written:



Hydrolysis and condensation continue simultaneously removing material from and adding material to the surface of particles until equilibrium is reached and the size of the colloids becomes fixed.

Initial fabrication of uniform silica spheres to act as chromatographic substrates is a relatively straightforward process, but the simple fabrication does not lead to a material with suitable chromatographic properties.

### Modeling Chromatography:

Georges Guiochon has devoted much of his research career to the mathematical modeling of chromatography, especially preparative scale chromatography. Excellent reviews of his work can be found in two books; *Theoretical Advancement in Chromatography and Related Separation Techniques*<sup>20-22</sup> and *Modeling for Preparative Chromatography*<sup>23</sup>. This prep scale modeling is particularly relevant to the pharmaceutical industry since they must do separations and purification on mixtures of large volumes and high concentrations.

It was computer code provided by Guiochon that enabled our group to determine the equilibrium constants and relative abundance of strong adsorption sites on commercial HPLC columns<sup>10, 24</sup>.

Our computer modeling of experimental chromatograms provided quantitative insight into the molecular scale interactions that occur in chromatographic separations.



## CHAPTER 2: INSTRUMENTATION AND SPECIAL METHODS

### Instrumentation:

#### Atomic Force Microscope:

The AFM used for this study was a Digital Instruments Bioscope, based on the Nanoscope IV controller, consisting of a Dimension 3100 SPM head mounted on a Nikon Eclipse TE2000-U inverted microscope.

The AFM probes used in this study were all obtained from MikroMasch. For general tapping mode images, NSC15 AIBS or NSC35 AIBS “Ultrasharp” tips were used. For contact mode imaging as well as all adhesive force measurements, CSC38 tips were used. These general use tips (NSC15, NSC35, CSC38) have reported radii of curvature of  $< 10$  nm. Where extremely high resolution images were required, DP-18 HiRes tips and DP-15 HiRES-W tips, which have a reported radius of curvature of  $< 1$  nm, were used. Both the DP-15 and DP-18 start with the basic “UltraSharp tip construction, but the DP-18 HiRES has a high aspect ratio carbon spike attached to the tip and the DP-15 HiRES-W has a high aspect ratio tungsten spike attached to the tip.

#### Fourier Transform Infrared Spectrometer:

Transmission FTIR spectra were obtained using a computer controlled Nicolet 4700 FT-IR spectrometer with a Harrick Brewsters Angle Sample Holder set to  $55^\circ$  with respect to the incident plane, and a 25 mm diameter, manual polarizer set to  $90^\circ$ .

The DRIFTS spectra were collected using the same Nicolet 4700 FT-IR spectrometer with a Harrick “Praying Mantis” DRIFTS module. Measurements were taken using the 3 mm sampling cup with FTIR grade KBr from Alfa Aesar. All spectra were collected using the same parameters, one thousand twenty four scans at a resolution of  $2\text{ cm}^{-1}$ . Prior to all measurements, the instrument was purged with dry air for 10 minutes to minimize the atmospheric carbon dioxide and water vapor signals.

#### High Pressure Liquid Chromatograph:

The chromatograph used in these studies was an Agilent 1100 with a quaternary pump, vacuum degasser, thermostatted column, and diode array absorbance detector. The mobile phase used in the work described in Chapter 4 was 90/10 (v/v) acetonitrile/water with 0.1% trifluoroacetic acid (TFA) with the ionic strength adjusted to 0.01 with KCl.

#### UV-Vis Spectrophotometer:

The UV-Vis spectrophotometer used in this work was a computer controlled Agilent 8453.

#### Special Methods

##### Determination of Refractive Index of Silica Colloids:

During the course of this work, it was necessary to develop a method to accurately measure the refractive index of the silica colloids.

Nussbaumer and co-workers developed a method to determine the refractive index of rough, transparent materials<sup>25</sup>. They measured the refractive indices of quartz glass, crown glass, and poly(vinylidene fluoride) (PVDF) films using a method that was based on the well known phenomenon of a transparent material becoming invisible when submerged in a liquid with the same refractive index. They measured the %Transmission at 589 nm for each material submerged in a series of 15 solvents with a range of refractive indices from 1.3333 to 1.6165. The data points were fit using several functions to determine the maximum %Transmission. The refractive index corresponding to the point of maximum %Transmission was the refractive index of the solid sample.

The method used by Nussbaumer et. al. was not appropriate for measuring the refractive index of silica colloids. In their work, they were able to wet the bulk surfaces of their samples with each of the different solvents, but silica colloids can not be adequately wetted by highly non-polar solvents and would not remain in suspension long enough to make an accurate measurement of the refractive index.

In order to get around this limitation, ethanol ( $n = 1.36$ ) and toluene ( $n = 1.50$ ) were mixed in volume fractions of toluene ranging from 0 to 1, and a calibration curve of refractive index at 589 nm versus volume fraction of toluene was constructed. This resulting calibration curve is shown in Figure 2-1, and the linear fit of the data indicates that toluene and ethanol mix in an ideal manner, and the refractive index varies directly as a function of the volume fraction of toluene.

Samples of the silica colloids were suspended in solvents with different ratios of toluene and ethanol, and the %Transmission at 589 nm was measured using the Agilent

UV-Vis spectrophotometer. It was important to make the %Transmission measurements at this wavelength, since, within a given material; refractive index varies with wavelength of the incident light. The 589 nm Sodium D line is the standard for measuring and reporting refractive index values, so all of our measurements were done at this wavelength. By varying the composition of the solvent, the point where %Transmission reached 100% could be approached with any degree of accuracy desired, and the refractive index of the silica colloids could be determined with precision.

This is a definite advantage over the Nussbaumer method where measurements were taken at predetermined refractive indices, and the maximum was determined by fitting functions to the data. Data fitting is not necessary in our method since the solvent refractive index can be made arbitrarily close to that of the silica colloids.

The physical principles behind this method of determining the refractive index can be explained using Snell's Law (Eq. 2-1) and Fresnel's transmission equations (Eq. 2-2,3):

$$n_i \sin(\theta_i) = n_t \sin(\theta_t) \quad (2-1)$$

$$t_{\perp} = \frac{4 n_i n_t \cos(\theta_i) \cos(\theta_t)}{(n_i \cos(\theta_i) + n_t \cos(\theta_t))^2} \quad (2-2)$$

$$t_{\parallel} = \frac{4 n_i n_t \cos(\theta_i) \cos(\theta_t)}{(n_t \cos(\theta_i) + n_i \cos(\theta_t))^2} \quad (2-3)$$

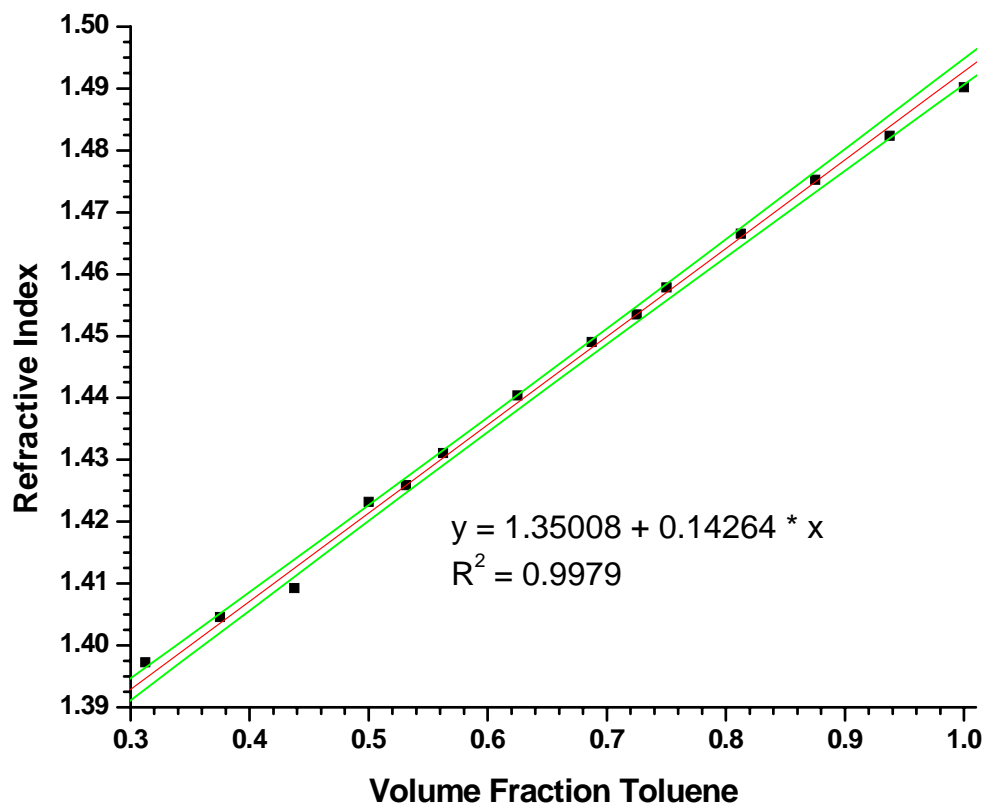


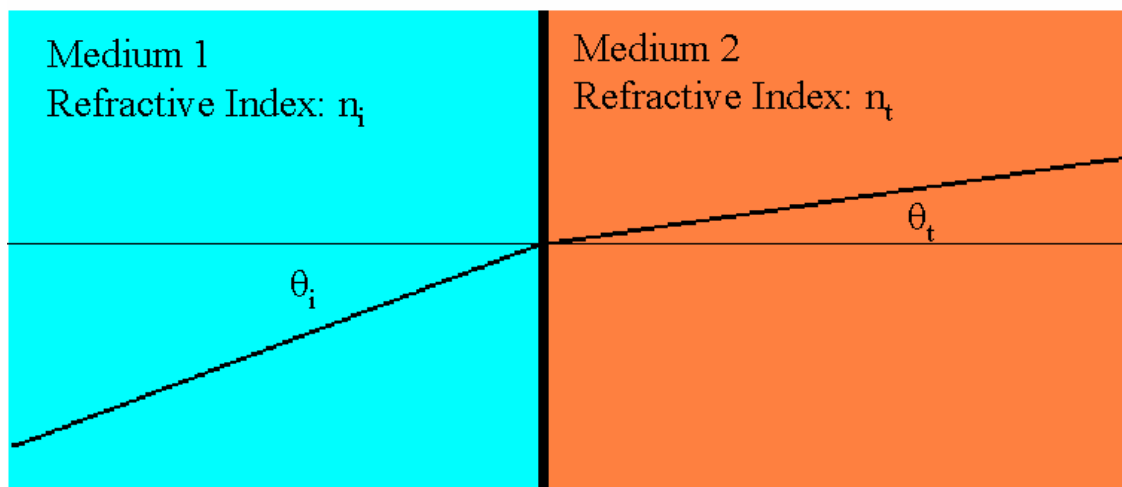
Figure 2-1. Calibration curve of Refractive Index versus Volume Fraction of Toluene. The red line is the linear fit of the data, and the green lines are the 95th Percent Confidence Intervals.

Figure 2-2 illustrates this situation. A light beam passes through Medium 1 and strikes the interface with some angle  $\theta_i$  with respect to the normal to the interface. The beam is refracted and passes through Medium 2 at angle  $\theta_t$  with respect to the normal. As the incident and refracted beams are shown in this figure,  $n_i$  must be less than  $n_t$  since  $\theta_i$  is greater than  $\theta_t$ .

Equations 2-2 and 2-3 are used to calculate the fraction of light transmitted through an interface of materials with refractive indices  $n_i$  and  $n_t$ , and they are for light polarized perpendicular and parallel respectively to the incident plane of the material. The transmission of non-polarized light is  $\frac{(t_{\perp} + t_{\parallel})}{2}$ , the mean of the polarized values.

Two special cases are of particular interest in this work; when the incident beam is perpendicular to the colloid surface and when the indices of refraction of the solvent and silica are exactly matched. In the first case  $\theta_i = 0$ , so by Snell's Law,  $\theta_t = 0$ , and the beam is not refracted. Additionally, equations 2-2 and 2-3 reduce to  $\frac{4n_i n_t}{(n_i + n_t)^2}$ . In the second case  $n_i = n_t$ , so  $\theta_i = \theta_t$  regardless of the value of  $\theta_i$ , and 100% of the incident light is transmitted through the colloid.

The second case is the condition used to determine whether the indices of refraction are matched. Since all of the light is transmitted through the colloid, there is no reflected light, and the colloids are invisible. With regards to the incident light, the suspension is homogeneous.



**Figure 2-2. Illustration showing the terms in Snell's Law and Fresnel's Transmission Equations. An incident beam strikes the interface between Medium 1 and Medium 2 and is refracted.**

The colloids in this study were large enough that the incident light was not always perpendicular to the incident plane but struck the colloids at a distribution of angles. If this were not the case, that is, the colloids were small enough that the light waves were always, in effect, perpendicular to the interface; this method could not be used to determine the silica refractive index with any degree of accuracy. If the incident beam were always perpendicular to the sample surface, Figure 2-3 shows what a plot of %Transmission versus the solvent index of refraction, where the silica colloid refractive index of 1.459 is assumed, would look like. The %Transmission only varies by 3 parts in 10000 over the refractive index range shown. The UV-Vis spectrophotometer can not make measurements with such precision. Compare this case to the actual experimental measurements shown in Figure 2-4. This data will be discussed in detail in Chapter 5. Even though the refractive index range is identical to that of Figure 2-3, the %Transmission range varies by 15%, which is easily measurable by the spectrophotometer.

In the Nussbaumer work, they were forced to abrade the surfaces of their samples to roughen them enough that a distribution of  $\theta_i$  values resulted. They show that even very large differences in solvent and sample refractive indices do not result in distinguishable levels of transmittance for very smooth samples. The transmittance peak becomes progressively sharper as the ratio of the surface correlation length to the RMS roughness of the surface gets smaller, and progressively smaller differences in refractive indices result in greater differences in the transmittance.



The sharpness of the experimental peaks in this work indicates that there is a large distribution of  $\theta_i$  values, and multiple refractions occur as the incident beam passes through the sample cell.

There are a number of issues that limit the usefulness of this method. The solvents must be miscible with one another to ensure complete mixing. The refractive indices of the solvents must bracket the expected value for the colloids so that some possible ratio of the solvents will have the same refractive index as the colloids. The solvents cannot be so volatile that they evaporate appreciably during the course of the measurements. The solvents must be compatible enough with the colloids that they remain in suspension long enough for accurate %Transmission measurements to be made.

In this work, the colloids came out of suspension in pure toluene very quickly, so the suspension had to be thoroughly sonicated immediately before being added to the UV-Vis cell, and the measurement had to be made immediately. This was not an issue for any solution where the volume fraction of toluene was less than 1.

Providing a suitable pair of solvents can be found, this method should be applicable for measuring the refractive index of suspensions of small particles of any shape. In fact, this method would actually work better for irregularly shaped particles since the incident angle distribution would be that much greater.

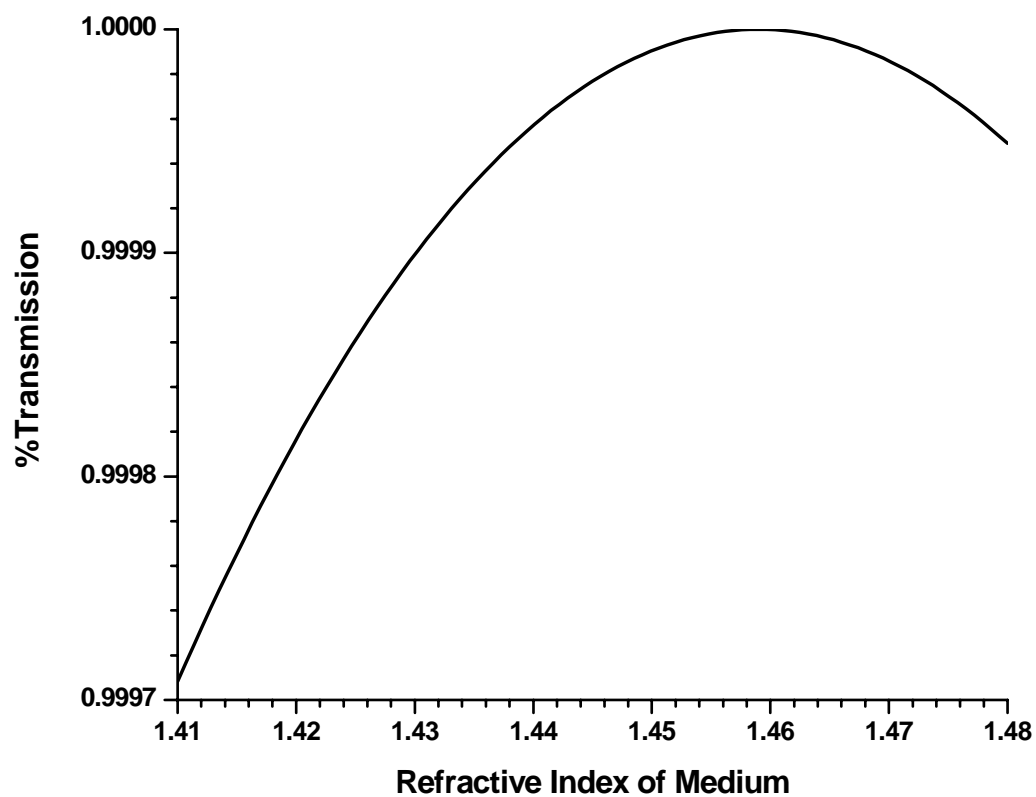


Figure 2-3. Theoretical Transmission calculated using the Fresnel Transmission Equation for light perpendicular to the sample. A refractive index of 1.459 is assumed for the silica particles in suspension.

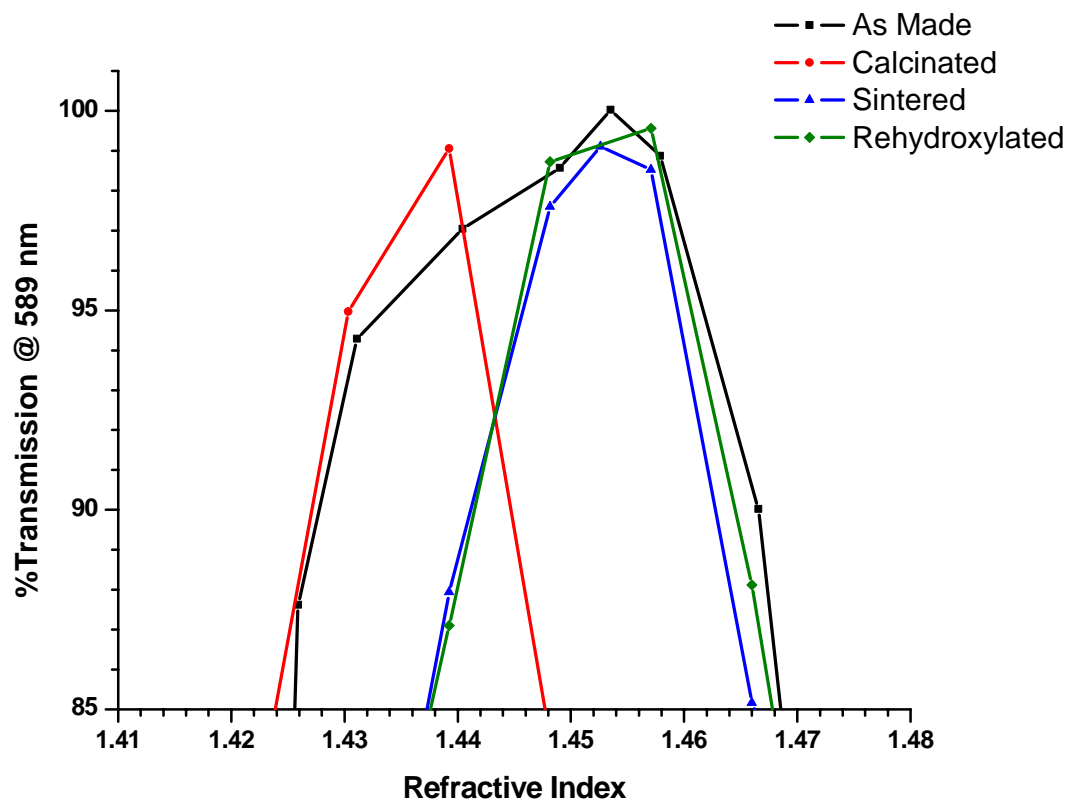


Figure 2-4. Refractive index measurements for As Made, Calcinated, Sintered and Rehydroxylated silica colloids. The maximum %T for each of the samples is; As Made 1.454, Calcinated 1.439, Sintered 1.452, and Rehydroxylated 1.457.

### Determining the Diameter of Silica Colloids Using AFM

Determination of silica colloid diameter and monodispersity has frequently been accomplished by measuring “hundreds” of individual particle diameters from SEM images<sup>17-19</sup>. The software package Gwyddion, which is described in the *Software Applications* section of this chapter can be used with AFM images to determine the size distribution of a silica colloid sample without resorting to the time consuming procedure of making multiple measurements of individual particles.

This method requires that the particles be deposited as a well-ordered, colloidal crystal on a substrate suitable for AFM analysis. After an AFM image of a suitably ordered region is obtained, it is rotated by whatever angle is necessary to align the silica colloids either horizontally or vertically, and then the image is cropped so that only the properly packed and aligned colloids remain. Gwyddion can then analyze this smaller image using its built in, autocorrelation function (ACF) and produce a graph with a series of peaks. The distance between these peaks is taken to be the colloid center-to-center distance, which corresponds to the diameter of a single colloid. Rather than the laborious process of measuring individual particles, this method can be used to characterize numerous particles with a single measurement. Figure 2-5 shows a series of images illustrating this procedure and the resulting autocorrelation graph.

With regards to silica and other non-conducting materials, this method is superior to SEM because it does not require the sample be coated with gold. Because the silica does not conduct electrons very well, they build up charge on the surface during SEM analysis and this excess charge appears as bright spots in the SEM image. This charging effect

can be reduced by sputter coating the silica with a layer of gold, but this layer is typically several nanometers to tens of nanometers thick. If this layer is not applied uniformly on the particles, errors in the autocorrelation measurement could result. Also, from a topographical standpoint, this gold coating would mask or distort any nanoscale features on the silica surface.

This method illustrates the usefulness of AFM in determining the size distribution as well as surface topography of our silica particles.

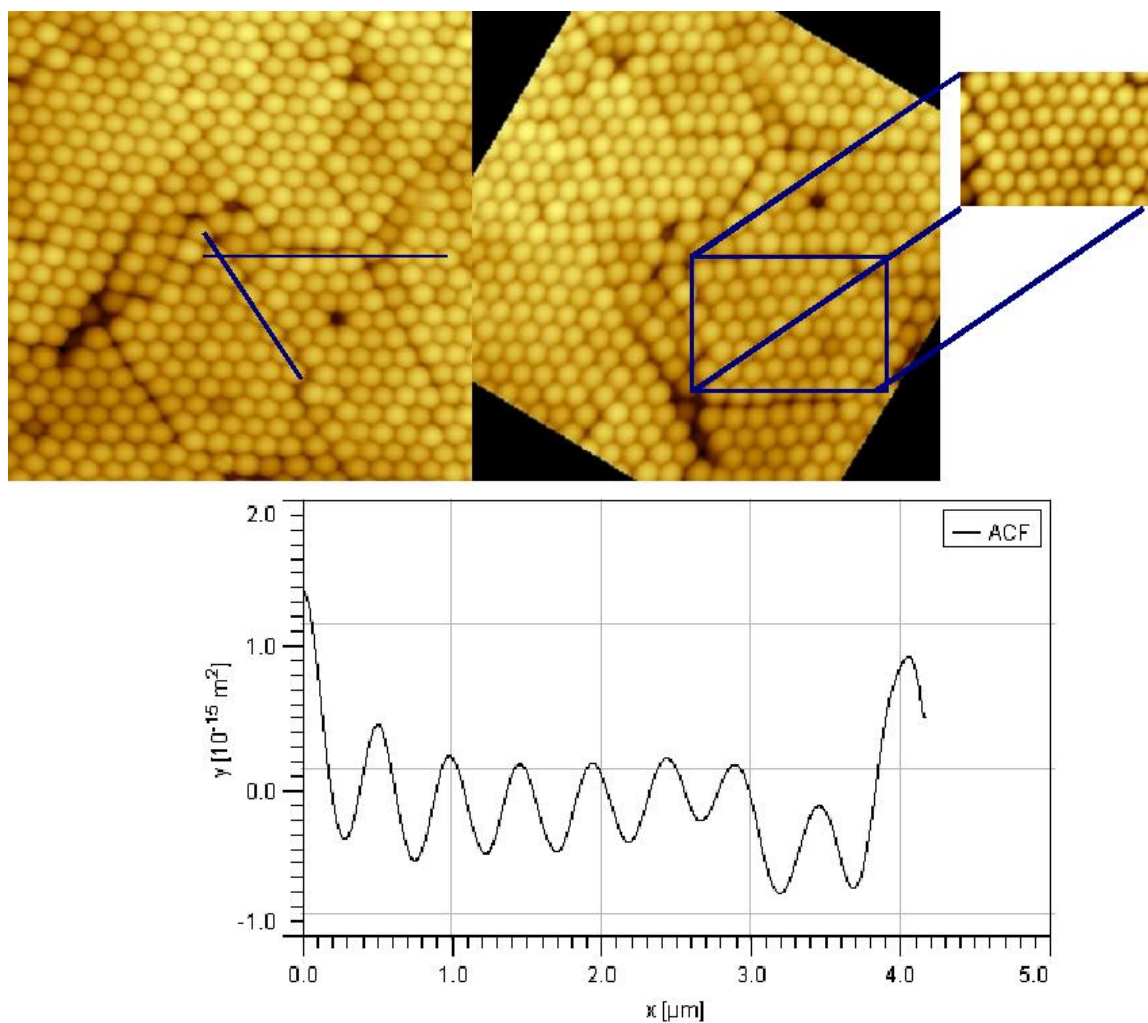


**Figure 2-5.** A well-ordered region of an AFM image is rotated to provide a horizontal orientation of colloids and then cropped. This cropped region is analyzed using the ACF (autocorrelation) function in Gwyddion. The average peak-to-peak distance for several such measurements is taken to be the colloid diameter.

## Software Applications:

### Gwyddion

Gwyddion<sup>26</sup>, a free software package from the Czech Metrology Institute designed specifically for SPM data analysis, was used as the primary image processing tool for AFM images. All measurement data, such as particle size, fractal dimension, and line scan profiles were determined using utilities included in Gwyddion.

Gwyddion is especially useful for AFM data analysis since it was designed for exactly that purpose, and it will open the native Nanoscope data files. Prior to using Gwyddion, the AFM data files were exported as formatted text files and then opened in ImageJ as “text images.” This required the user to input pixel counts and scan sizes in order to get distance measurements in the ImageJ software; because it could open the Nanoscope files directly, Gwyddion could handle this issue automatically.

### ImageJ

ImageJ<sup>27</sup>, a free software package available from NIH was used extensively in this work. It was used to view AFM and fluorescence microscopy images.

A particularly useful feature allowed for the creation of 3-D versions of the AFM images that included lighting and shadows. By including the lighting and shadows surface features that were only a few nanometers high could be distinguished from the bulk of the surface. On a flat surface, the height scale of the AFM can simply be adjusted to show such features, but many of the AFM images in this work were taken on spherical silica particles ranging from hundreds of nanometers to five microns, so the height scale

had to be adjusted accordingly. The height range for many of the images taken in this work varied by many tens or even hundreds of nanometers, and surface features only a few nanometers high would be indistinguishable in such an image.

All quantitative data was collected from the planar AFM image, before converting them to 3D and adding lights and shadows.



## CHAPTER 3: A REVIEW OF SINGLE-MOLECULE PROBING OF ADSORPTION AND DIFFUSION ON SILICA SURFACES

### Introduction:

Single-molecule spectroscopy is a useful tool for unraveling heterogeneous systems. It enables the observation of one member of an ensemble at a time, allowing the construction of sorted sub-ensembles through multiple measurements of the individual events. This is illustrated in Figure 3-1, the first example of a detailed physical study by single-molecule spectroscopy: pentacene undergoing spectral diffusion in *p*-terphenyl crystals at low temperature<sup>28</sup>. Figure 3-1*a* shows the excitation spectrum of a single pentacene molecule changing over more than 1 hour of data acquisition time. The jumps in the excitation spectrum are from an abrupt change in the arrangement of the *p*-terphenyls surrounding the pentacene molecule. In this small subset of spectra, one can see repeating features as the system evolves in time. Each spectrum represents the sub-ensemble of molecules in one configuration, and the entire set of spectra is the ensemble one would observe in a conventional spectroscopic experiment. Figure 3-1*b* shows the temporal information in a different way. Two single molecules were each monitored at fixed excitation wavelengths, and the fluorescence emission disappears and reappears as the resonance frequency of the molecule jumps on the timescale of tens of seconds.

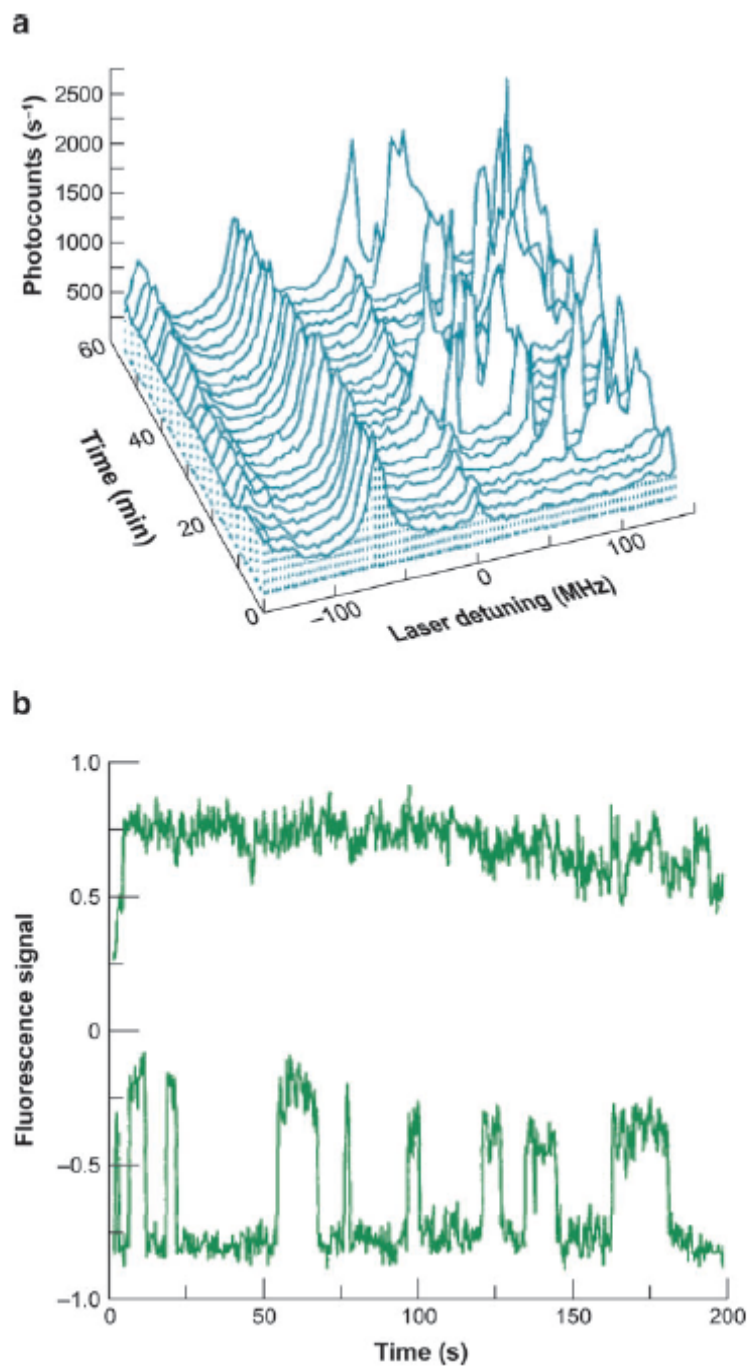


Figure 3-1. (a) Spectra for single molecules of pentacene in *p*-terphenyl as a function of time, illustrating spectral diffusion. (b) Intensities of single pentacene molecules in *p*-terphenyl as a function of time, illustrating kinetics of spectral diffusion. Figure taken from Ambrose et. al. 1991<sup>28</sup>.

The trace at the top of Figure 1*b* is for a molecule in a stable site, and the lower trace is for a molecule whose site fluctuated significantly. These data also represent the first measurement of kinetic behavior for single molecules. The average interval between bursts of fluorescence in the lower trace of Figure 3-1*b* is related to the rate at which the site achieves the configuration that puts the pentacene molecule into resonance. The duration of the fluorescence burst is related to the rate at which the site loses this configuration. Such information about the dynamic exchange of sites cannot be obtained from ensemble measurements, and it illustrates how single-molecule spectroscopy can probe dynamic equilibria.

While some researchers were working on these single-molecule studies in cryogenic crystals, several other research groups were developing the ability to detect single molecules at room temperature in fluid solutions<sup>29-32</sup>. The instrumental challenge was to reduce the contribution of the solvent background to the emitted light intensity, where this background is mainly from Raman emission. The first bursts of fluorescence from single rhodamine 6G molecules that were well above the solvent blank were seen using a tightly focused laser beam to minimize the excitation volume and time-windowing to reject Raman emission further from the solvent<sup>31</sup>. The fruits of these efforts have greatly expanded the scope of single-molecule spectroscopy.

This new ability to detect single molecules of a commonly used moiety in fluorescence labeling provided enormous promise for the wide applicability of single-molecule spectroscopy, which was subsequently applied to the study of molecular diffusion<sup>33-38</sup>.

Near-field microscopy demonstrated the concept of enhancing the signal-to-noise ratio for single-molecule detection by reducing even further the contribution to the emission from the solvent<sup>35, 39-44</sup>. This technique is used less often today in single-molecule spectroscopy because of the very low light levels tolerated by the optical fibers and the difficulties in routinely making reproducible optical fibers for near-field microscopy.

The introduction of confocal microscopy provided a more practical way of reducing the background contribution to improve the signal-to-noise ratio<sup>45, 46</sup>. Figure 3-2 illustrates the data for the first single-molecule measurements using confocal microscopy. The bursts of fluorescence are from single molecules diffusing rapidly through the beam. These results show that data from single molecules can readily be obtained on the millisecond timescale.

As an alternative to confocal microscopy, imaging cameras have been used since the early years of microscopy<sup>33, 34, 36-38</sup>. Over the years, their capabilities have steadily improved to the present level of 90% quantum efficiency.

Ultimately, single molecules undergoing both diffusion and adsorption to surfaces could be probed<sup>47, 48</sup>.

Although signal-to-noise ratios are now very high, there are still phenomena that make single-molecule spectroscopy challenging, such as blinking<sup>49-53</sup>, which results when a fluorophore is temporarily trapped in a triplet state, and photobleaching.

These pioneering studies enabled today's applications of single-molecule spectroscopy to many interesting chemical systems, including materials science, chemical

biology, and DNA sequencing. This chapter describes one such important application within materials science: the use of single-molecule spectroscopy to study defects on silica surfaces.

#### Chromatographic Silica Gel:

High-performance liquid chromatography (HPLC) illustrates the success of translating concepts and methods from materials science and nanoscience, to widespread commercial practice. Very high-quality silica gel with controlled pore size on the nanoscale has been available for more than a decade, and monolithic silica with a bimodal distribution of pore sizes has now emerged as a valuable material for HPLC<sup>54</sup>. HPLC has become an indispensable tool in the pharmaceutical industry, and it is widely used both to separate complex peptides in proteomics and to analyze proteins. Additionally, it is widely used as a preparative tool, allowing the isolation of a desired protein or product of a chemical synthesis. In biotechnology, proteins such as human insulin, one of the most medically important proteins, are purified on the production scale by HPLC<sup>55</sup>. Despite the successful applications of HPLC, there is a large demand for better materials.

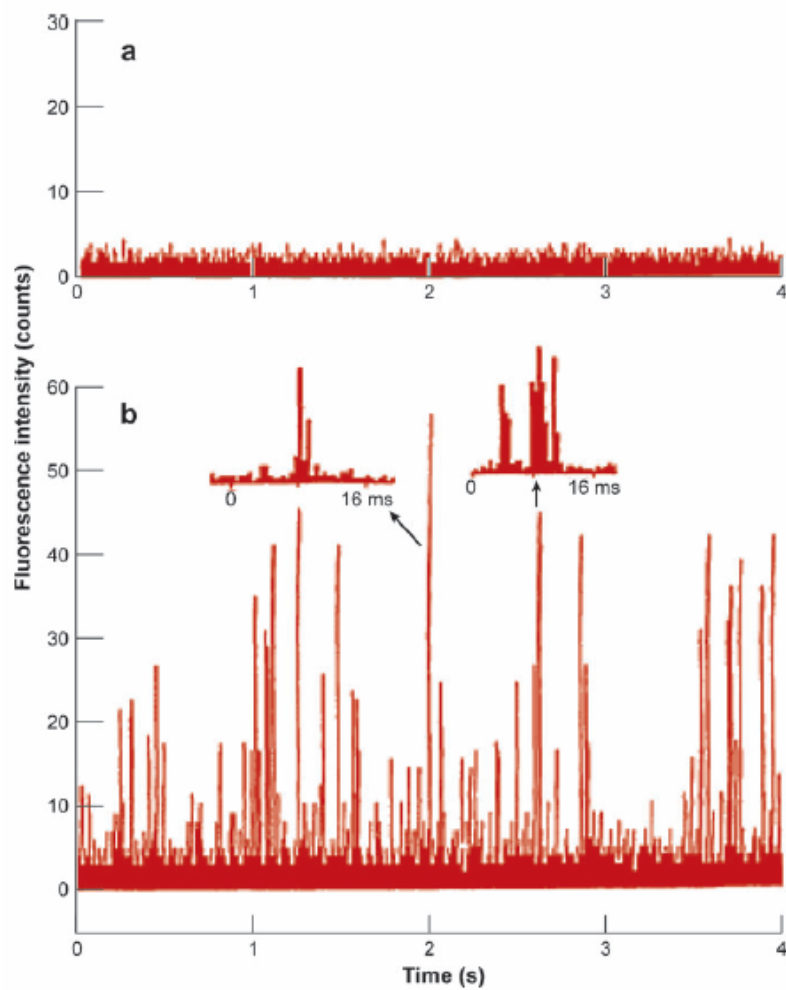


Figure 3-2. Bursts from single molecules of fluorescein diffusing rapidly through a laser beam and detected by confocal microscopy: (a) emission from the solvent blank and (b) emission from a solution of  $3 \times 10^{-10}$ -M fluorescein in water. Figure taken from Nie, et. al. 1994<sup>45</sup>.

The silica used for HPLC has one major problem: The surface is intended to be homogeneous, yet it is heterogeneous. Even when silylation reactions are run exhaustively, some exposed silica always remains. This is illustrated schematically in Figure 3-3, which depicts an ideal, fully silylated silica surface. The silane layer is made up of dimethyloctadecylsiloxane, which is the most commonly used monolayer in HPLC. To the right, on the top panel, is a chromatogram with a narrow, symmetric peak that would be obtained for this idealized surface. The bottom half of the figure illustrates reality: The monolayer has a hole, exposing the silica surface, which has both silanol groups ( $\text{SiOH}$ ) and dissociated silanols ( $\text{SiO}^-$ ) that are present at intermediate pH owing to the acidity of silanols. These exposed silanols and  $\text{SiO}^-$  groups are problematic because proteins, peptides, and many pharmaceuticals have amino groups which are protonated at neutral pH. Protonated amines can hydrogen bond with the silanols or undergo Coulombic interaction with the dissociated silanols. In the bottom right corner of Figure 3-3, the chromatographic peak for the heterogeneous surface is shifted to a longer elution time, and is both broadened and asymmetric. Thus, longer analysis times are required and fewer components can be completely resolved in the mixture. The phenomenon of peak asymmetry is of intense interest, and different columns, mobile phases, additives, and analytes have been studied to try to understand this phenomenon<sup>3, 56-59</sup>. There are many ways to reduce the effects of this exposed silica, such as further silylation with a smaller reagent (referred to as endcapping), the use of lower pH or higher ionic strength, and the addition of amine additives.

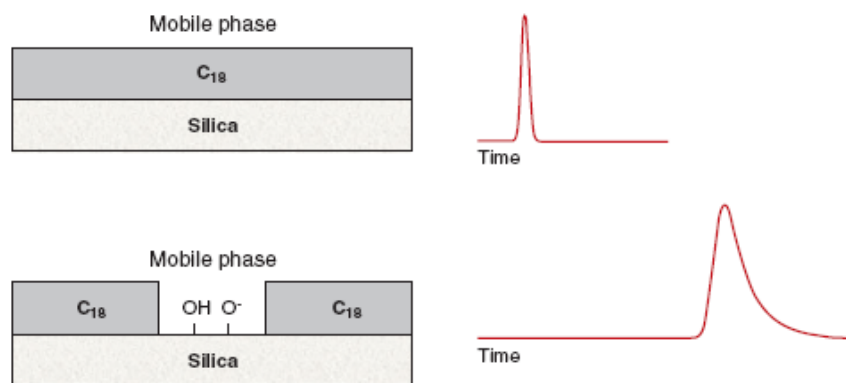


Figure 3-3 (*Top panel*) Schematic representation of an idealized, fully silylated silica surface and the resulting idealized chromatogram. (*Bottom panel*) The more realistic surface and the experimental chromatogram.



These approaches have been discussed extensively in other reviews<sup>4, 5, 60</sup>. The presence of exposed silanols in hydrocarbon monolayers continues to pose a considerable problem in the practice of HPLC. Other materials have been developed to replace silica, but they perform more poorly, so, improving silica may be the most promising approach to improving chromatography.

Peak broadening from silanols is well understood to result from slower desorption kinetics<sup>14</sup>. The underlying causes of peak asymmetry and later elution time can be explained from the adsorption isotherm. We can describe adsorption in the presence of two different types of functional groups on the surface by the bi-Langmuir adsorption isotherm shown in Eq. 1-1:

$$\Gamma = \Gamma_{sat,weak} \cdot \frac{K_{weak} \cdot c}{1 + K_{weak} \cdot c} + \Gamma_{sat,strong} \cdot \frac{K_{strong} \cdot c}{1 + K_{strong} \cdot c}$$

We use concentration,  $c$ , rather than activity because the concentrations are typically low. The second term in Equation 1-1 describes the increased retention depicted in Figure 3-3. The severe peak asymmetry of Figure 3-3 occurs when  $c \geq 1/K_{strong}$ , which makes the denominator term in Equation 1-1 deviate significantly from unity. Manufacturers of silica gel would like to produce a commercial product where  $\Gamma_{sat,strong}$  approaches zero, but the methods that can be employed to achieve this are still unknown.

Advances in the simulations of chromatographic peaks allow one to determine the parameters of Equation 1-1 from experimental measurements of the concentration dependence of chromatograms<sup>6-8, 61</sup>. One such study yielded important and insightful information<sup>24</sup>. The solute DiI(C12), an amphiphilic organic cation, was used because of

its chromatographic properties and because it is amenable to single-molecule spectroscopy. The results showed that  $K_{strong} = (5.1 \pm 0.1) \times 10^4$ , which explains why peak asymmetry is significant for DiI at a concentration of  $10^{-4}$  M. For the chromatographic column used for that study, if all of the surface silanols were this strongly adsorptive, the estimated retention time would be 1 week. Instead, the retention time at 18 min is 1000-fold shorter because  $\Gamma_{sat, strong}$  composes only 0.1% of the surface silanols<sup>24</sup>. The concept of Figure 3-3 is thus inaccurate: Not all exposed silica causes a problem; only a tiny fraction of the silanols compose the strong adsorption sites. Eliminating the strong sites requires identifying them and understanding why they arise.

Köhler et al.<sup>62</sup> achieved a breakthrough in the understanding of strong adsorption when they showed evidence that the strong sites are isolated silanols. Most silanols are sufficiently close to one another to hydrogen bond, whereas isolated silanols are not and remain available to hydrogen bond to pharmaceuticals, peptides, and proteins. The infrared spectra and chromatograms reported by Köhler et al.<sup>62</sup> showed that a blue shift in the infrared spectrum for the isolated silanols correlates with increased chromatographic peak asymmetry. They further showed that treatment of the silica with HF or a strong base red-shifts the spectrum for the isolated silanols and reduces chromatographic peak asymmetry<sup>63</sup>. The evidence is shown in Figure 3-4a, which compares the infrared spectra for treated versus untreated silicas. There is a sharp peak for isolated silanols in the vicinity of  $3740\text{ cm}^{-1}$ . The inset in Figure 3-4a has an expanded scale showing that the treated and untreated silica have isolated silanol peaks at  $3738$  and  $3741\text{ cm}^{-1}$ , respectively. Figure 3-4b compares the chromatograms, showing that the untreated silica

has profoundly more peak broadening and asymmetry for the compound 2 (N,N-diethylaniline), which is particularly sensitive to the quality of the silica gel. The conclusion is that the most blue-shifted silanols, which correspond to the most isolated silanols, are the strong adsorption sites. Figure 3-4*a* shows the spectrum for the silica gel before silylation. It is interesting to note, however, that the peaks from these isolated silanols disappear into the baseline noise after silylation. This is consistent with the chromatographic data for DiI, which indicate that the strong sites are rare. Therefore, the actual strong adsorption sites are not directly detected, and the identification of the strong sites as isolated silanols is inferred from a correlation, albeit a convincing one.

These studies led to the creation of today's modern silica gel through base treatment, which alone has enabled high-performance separations of pharmaceuticals, peptides, and proteins. These studies led to human insulin being separated by process-scale HPLC and reduced the cost of its production.

This theory does not explain why some isolated silanols persist despite treatment with base. Today, enough strong adsorption sites remain on even the highest-quality silica gel to double the retention time for DiI compared with what it would be without strong adsorption sites<sup>24</sup>. This presents both an opportunity to improve chromatography and a challenge because the surface concentration of strong sites is extremely small. Only 1 in 1000 surface silanols is problematic, and any experiment to probe them directly must sense this one silanol and report why it is there. Single-molecule spectroscopy is ideally suited for such problems because it allows one to watch individual events in isolation.

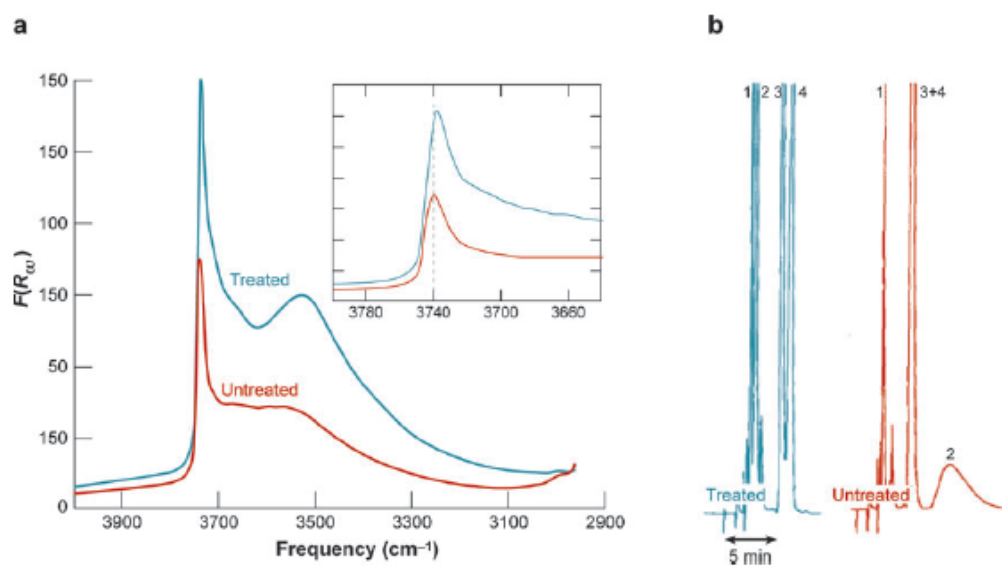


Figure 3-4. (a) The infrared spectra in the O-H stretching region for HF-treated versus -untreated silica gels. The inset shows spectra on an expanded scale. (b) Chromatograms for HF-treated versus-untreated silica gels for compound 2 (N,N-diethylaniline). Figure taken from Kohler and Kirkland 1987<sup>63</sup>.

### Single Molecule Measurement of Strong Adsorption:

In the past, our group explored strong adsorption on silyated fused silica by using single-molecule spectroscopy to test whether a tiny subset of highly adsorptive sites exists, consistent with the idea of rare isolated silanols, and, if so, whether we could observe anything that helps explain why these sites persist. We used DiI(C18), which had been used previously in single-molecule spectroscopy<sup>42, 43</sup>. This dye is similar to the DiI(C12) used in the chromatographic studies discussed above<sup>24</sup> but with octadecyl instead of dodecyl chains. The basic idea of the single-molecule experiment is that, although most amphiphilic DiI molecules will diffuse rapidly at the interface of the hydrocarbon stationary phase and polar mobile phase (Figure 3-3), every great once in a while a DiI molecule will stop at a rare, strong adsorption site.

Confocal microscopy showed bursts of fluorescence as the single molecules traversed a laser beam of 10  $\mu\text{m}$  in diameter, focused onto the interface. Most data sets had only bursts of fluorescence resulting from single molecules rapidly diffusing through the beam. Blinking occurs on the timescale of 1 ms or shorter, so, to avoid significant effects from blinking, the acquisition time for these experiments was set to 4 ms. The experiments readily proved that diffusing molecules existed in dynamic equilibrium with rare, strongly adsorbed molecules. Figure 3-5 shows an example of a data set in which strong adsorption occurred<sup>48</sup>. The varying heights of the bursts are a result of the changing positions of the molecules in the Gaussian beam as they underwent Brownian motion. A strong adsorption event started at 888 s and lasted 200 ms. Strong adsorption can be distinguished from diffusion because strong adsorption causes the molecule to

remain in the same position in the Gaussian beam, thus giving a constant intensity within the shot noise for the duration of its binding. This event began and ended with diffusion, as shown by the spikes on either end of the burst. Overall, 1% of the 2048 molecules observed in the experiment underwent strong adsorption, so the phenomenon of strong adsorption is rare on fused silica.

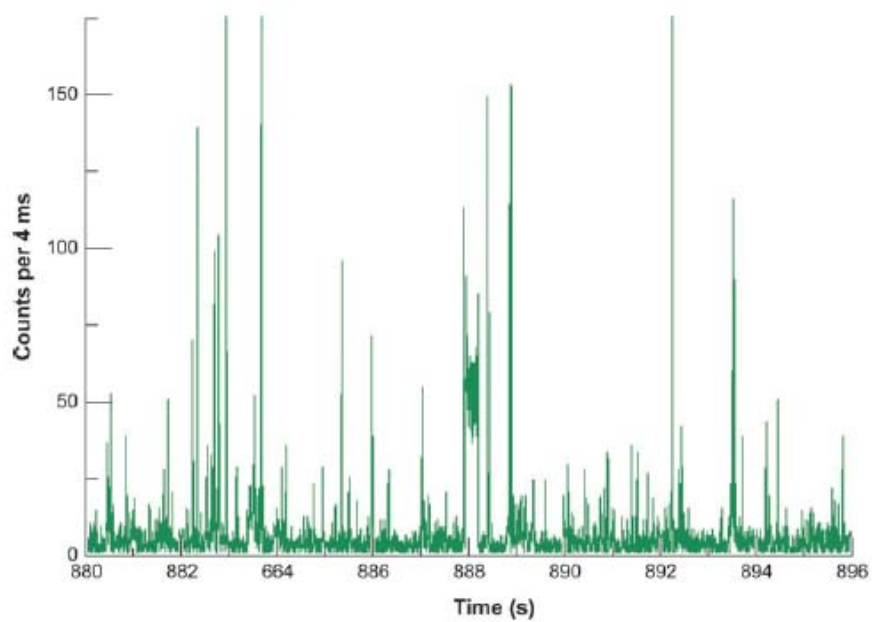


**Figure 3-5. Single-molecule burst data showing many diffusion events and one strong adsorption event. The many diffusion events produce the sharp spikes. The strong adsorption event started at 888 s. Figure taken from Wirth and Swinton 1998<sup>48</sup>.**

### Fused Silica versus Silica Gel

Fused silica was used in the single-molecule experiments as a mimic of silica gel because its highly polished surface enables fluorescence microscopy to be performed with diffraction limited optical resolution. The fused silica surface was fully hydroxylated and then silylated in the same way chromatographic silica gel is treated<sup>48</sup>. Furthermore, the same step used to reduce strong adsorption in chromatography, (i.e., reducing the number of residual silanols by reacting them with a smaller silane, chlorotrimethylsilane) was also used to reduce the number of strong adsorption events in the single-molecule experiment. These experiments were performed at neutral pH.

A serious contradiction arose between the results of the single molecule experiments and current knowledge regarding chromatography. The use of a mobile phase at pH 2 was thought to greatly reduce strong adsorption, as evidenced by less peak asymmetry and less peak broadening in chromatography. Illustrating the dramatic effect of pH on chromatography, Figure 3-6 shows chromatograms of DiI(C12) at neutral pH versus pH 2. Peak broadening and asymmetry decrease inordinately at pH 2. By contrast, the single-molecule experiment showed that low pH gave no reduction in the number of strong adsorption events. After much troubleshooting, investigators confirmed that the only effect of lowering the pH to 2 was to cause the single molecules to diffuse faster.



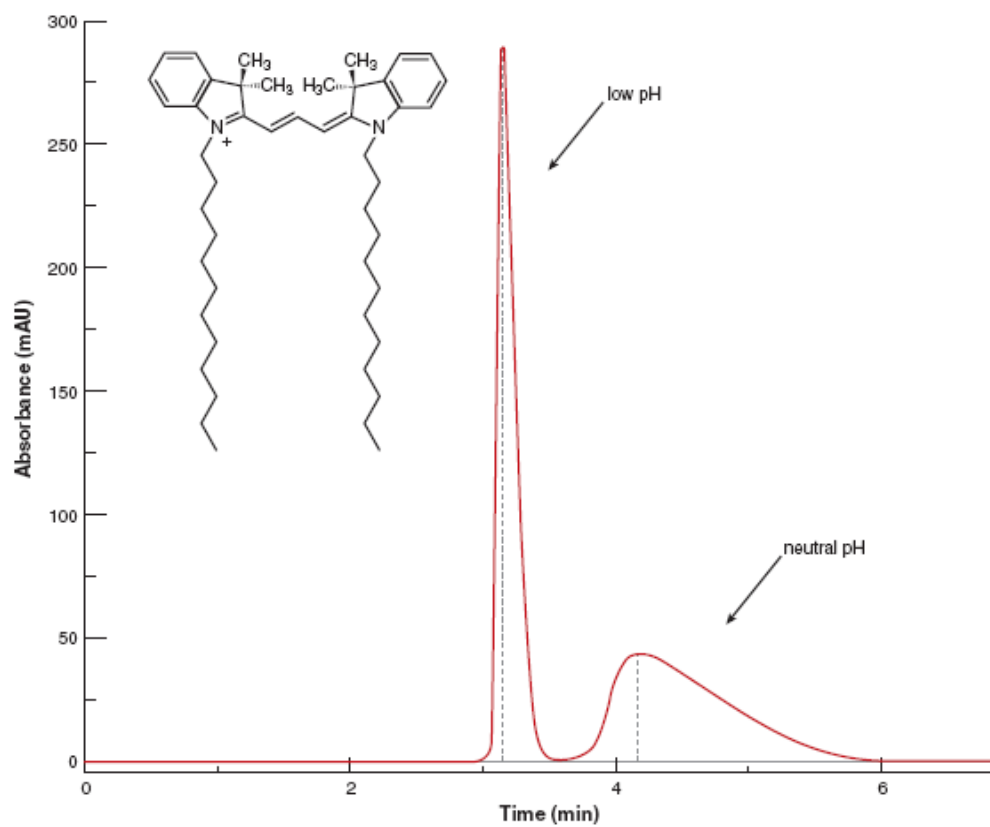


Figure 3-6. Chromatograms of DiI at two different pH values, illustrating how peak asymmetry and broadening typically depend on pH. The inset shows the molecular structure of DiI(C12). Figure taken from Wirth et. al. 2003<sup>64</sup>

Evidence such as in Figure 3-6 always led to the assumption that the strong adsorption sites for organic cations are the dissociated silanols, the  $\text{SiO}^-$  groups, whose population approaches zero at pH 2. Any remaining peak asymmetry at pH 2 was presumed to be a result of unusually acidic isolated silanols. The looming contradiction between this theory and the single-molecule result demanded explanation. By studying the concentration dependence of chromatograms at a series of pH values and using the bi-Langmuir adsorption isotherm of Equation 3-1 as the model, researchers tested for the first time the assumption that the pH dependence of peak asymmetry is caused by a change in the number of strong adsorption sites<sup>65</sup>. The results revealed that the number of strong adsorption sites changed negligibly with pH. If anything, the number of strong adsorption sites increases slightly as the pH is reduced. Thus the results of the single-molecule experiment are in full agreement with those of chromatography, and the widely held belief that strong adsorption sites are necessarily  $\text{SiO}^-$  groups turns out to be incorrect. The sites are neutral.

The question remained, why did the chromatography improve significantly at lower pH even though the number of strong adsorption sites remains nearly constant? The answer is simple physical chemistry. The strong adsorption sites become even stronger when they are surrounded by dissociated silanols that impart a Coulombic attraction for the organic cation. This is illustrated in Equation 3-1, which shows that  $K_{strong}$  is amplified by the Coulombic attraction:

$$\Delta G_{strong}^0 = \Delta G_{SiOH}^0 + \Delta G_{coul}^0 = RT \cdot \ln(K_{strong} \cdot K_{coul}). \quad (3-1)$$

The adsorption isotherm is thus more nonlinear at high pH at which the prevalent silanols are dissociated, thus giving more peak asymmetry. Without the single molecule experiment to question the chromatographic interpretation, it may not have been discovered that the strong adsorption sites are neutral in charge.

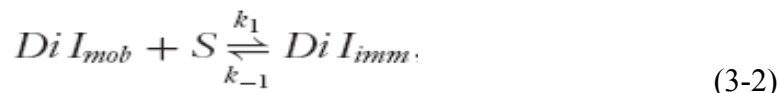
Another question is why do the single molecules diffuse faster at lower pH and higher ionic strength? Although these conditions were not studied separately, this result is presumed to be a result of the surface charges exerting a force to draw the molecules closer to the substrate, where the slower moving atoms of the silanes are located. Lower pH and higher ionic strength reduce this Coulombic force to allow faster diffusion.

The chromatographic studies, as well as the dependences on pH and ionic strength, support the relevance of the single-molecule experiments, even though the latter are performed on fused silica, whereas chromatography is performed on silica gel.

### Kinetics

The chromatographic studies discussed above also reveal that DiI has a desorption rate constant of  $80 \text{ ms}^{-1}$  at  $20^\circ\text{C}$ . Single-molecule experiments reveal kinetic information (see Introduction, this chapter) that enables a comparison of fused silica with chromatographic silica gel. One would assume that the two materials have different surface concentrations of strong adsorption sites because they are made differently. However, if the adsorption and desorption kinetics from the strong adsorption sites on the two materials vary, then strong adsorption would arise from two different chemical species and the single-molecule results would not be relevant to chromatography.

Currently, two ways to analyze single-molecule data for kinetic information are known. Consider the adsorption and desorption equilibrium of Equation 3-2,



where  $S$  is the strong adsorption site, and the DiI molecule is either mobile or immobile. Figure 3-7 illustrates one way to measure these rate constants. The adsorption interval fluctuates randomly from one event to the next, in accord with Poisson statistics, and the average interval between adsorption events,  $\langle \tau_{int} \rangle$ , is inversely proportional to the adsorption rate constant,  $k_1$ . This interval is related to the conventional, ensemble description of adsorption kinetics through the second-order rate expression,

$$-\frac{dC_{site}}{dt} = k_1 C_{mob} \cdot C_{site}; \quad \frac{C_{site}}{C_{site}(t=0)} \exp(-k_1 t \cdot C_{mob}) = \frac{C_{site}}{C_{site}(t=0)} \exp(-t/\langle \tau_{int} \rangle). \quad (3-3)$$

The dependence of the interval on the concentration of mobile DiI, which is denoted  $C_{mob}$ , allows calculation of the adsorption rate constant, where  $\langle \tau_{int} \rangle = 1/(k_1 \cdot C_{mob})$ . Measuring the adsorption rate constant with single-molecule spectroscopy requires knowing the concentration of freely diffusing analyte,  $C_{mob}$ , on the surface. This concentration, which is less than one molecule per  $(10 \text{ } \mu\text{m})^2$ , can be determined quantitatively by counting molecules<sup>66</sup>.

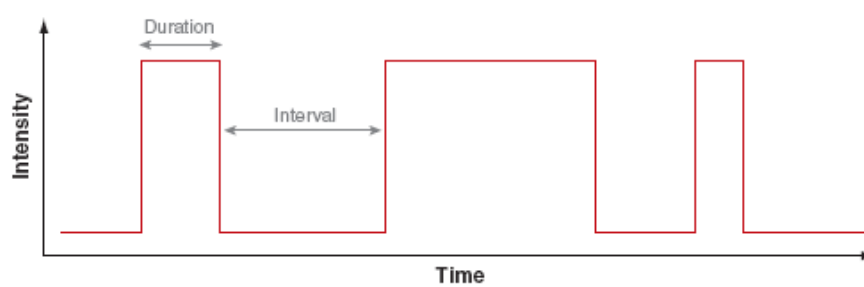


**Figure 3-7. Schematic of adsorption and desorption events in single-molecule spectroscopy. The interval between adsorption events and the duration of adsorption events both fluctuate randomly from one event to the next, in accordance with Poisson statistics.**

Similarly, as shown in Figure 3-7, measurement of the average duration time of adsorption events,  $\langle\tau_{dur}\rangle$ , yields the desorption rate constant,  $k_{-1}$ :

$$-\frac{dC_{imm}}{dt} = k_{-1}C_{imm}, \quad \frac{C_{imm}}{C_{imm}(t=0)} \exp(-k_{-1}t) = \frac{C_{imm}}{C_{imm}(t=0)} \exp(-t/\langle\tau_{dur}\rangle) \quad (3-4)$$

Knowing these rate constants yields the adsorption equilibrium constant,  $K$ :

$$K = \frac{\langle\tau_{dur}\rangle}{\langle\tau_{int}\rangle C_{mol}} \quad (3-5)$$

The disadvantage of this approach is that many events must be measured to calculate precise averages for the interval and durations of adsorption events. An analysis program would have to account for the possibilities that two molecules can be in the beam simultaneously and the baseline noise can obscure the start or end times of events. Despite its limited practical utility, one can use this approach to extract information about adsorption and desorption kinetics from single-molecule data (Figure 3-7).

The second way of analyzing single-molecule data, which is less prone to error, is autocorrelation analysis. This technique, called fluorescence correlation spectroscopy, was a precursor to single-molecule spectroscopy<sup>67-69</sup> and has been used to detect diffusing single molecules<sup>70-76</sup>. Fluorescence correlation spectroscopy can accommodate the presence of many molecules within the beam simultaneously, which avoids the need to work at near-infinite dilution. The greater number of molecules in the beam inherently produces information faster. Fluorescence correlation spectroscopy was designed for the study of binding phenomena in the presence of diffusion. The principle behind it is

elegant: There are statistical fluctuations in the concentrations of mobile and immobile analyte (i.e., molecular shot noise exists), and the correlation of this shot noise is related to the kinetics. Figure 3-7 depicts the molecular shot noise. The pioneers of fluorescence correlation spectroscopy recognized that one could describe the concentration fluctuations in the frequency domain,  $\tilde{C}(\nu)$ , instead of the time domain,  $C(t)$ , to linearize the mathematical relations between concentration and rate constants<sup>67-69</sup>. The differential of the frequency domain concentration with respect to the autocorrelation variable,  $\tau$ , is a simple analytic expression:

$$\frac{\partial \tilde{C}_i}{\partial \tau} = \sum_j M_{ij} \delta \tilde{C}_j. \quad (3-6)$$

The matrix elements,  $M_{ij}$ , express the kinetic parameters:

$$\mathbf{M} = \begin{vmatrix} -(\nu^2 D_{site} + k_1 \tilde{C}_{mob}) & -k_1 \tilde{C}_{site} & k_{-1} \\ -k_1 \tilde{C}_{mob} & -(\nu^2 D_{mob} + k_1 \tilde{C}_{site}) & k_{-1} \\ k_1 \tilde{C}_{site} & k_1 \tilde{C}_{site} & -(\nu^2 D_{imm} + k_{-1}) \end{vmatrix}. \quad (3-7)$$

Elson & Magde<sup>67</sup> solved this in the limit of frequent binding, applicable to protein interactions in biology. Our group<sup>77</sup> solved this in the limit of rare binding interactions, applicable to the study of rare defects on surfaces, resulting in a simple sum of decay terms in the autocorrelation function,  $G(\tau)$ :

$$G(\tau) = \frac{\varepsilon_B Q_B f_B}{1 + \tau \frac{D}{s^2}} + \sum_i \varepsilon_{C,i} Q_{C,i} f_{C,i} \cdot \exp(-k_{-1,i} \tau). \quad (3-8)$$

The first term is the familiar decay of the autocorrelation owing to molecular diffusion, where  $D$  is the diffusion coefficient, and the second term is a sum of exponentials owing to the desorption kinetics.  $f$  is the fraction of molecules undergoing each type of behavior, and  $\epsilon$  and  $Q$  are the molar absorptivity and quantum efficiency of the fluorophor, respectively. This equation enables one to determine the desorption kinetics by using a simple autocorrelation, fit to the function of Equation 3-8, rather than the tedious and error-prone analysis of each of the single-binding events.

Why then should one bother with single-molecule spectroscopy if fluorescence correlation spectroscopy is the better way to analyze the data? Even though for most experiments single-molecule spectroscopy is not worth the great effort it requires, it uniquely enables an interpretation by providing direct observations of single events.

Autocorrelation of many data sets for bursts, such as the data set shown in Figure 3-5, provides a double-exponential decay plus a rapid decay component owing to diffusion, with  $D = 6.5 \times 10^{-6} \text{ cm}^2 \text{ s}^{-1}$ . The short component of the double-exponential decay was 100 ms. Within the uncertainty in the temperature differences of the two experiments, this result is in reasonable agreement with the 80-ms desorption time that was obtained from the chromatographic studies. The longer decay component was 2.6 s. It was discovered that this measurement was artificially shortened by photobleaching, and later experiments revealed the accurate value of the second decay component to be 8 s. The agreement on the scale of 100 ms suggests that the strong adsorption sites for the two materials may be the same, but it raises the question of why the fused silica has an additional 8-s decay component that is not evident in the chromatography. A separate



study was undertaken in which the DiI solution remained in contact with the silica gel over 10 min, rather than just the brief period of 10 s allowed in the chromatography experiments. These results showed that an 8-s decay component was also present for the chromatographic silica gel<sup>78</sup>. In addition, both materials had a third type of adsorption site with very slow desorption kinetics. For the fused silica, the decay constant was in excess of 2 min, with the determination of its value limited by photobleaching, whereas for chromatographic silica gel, the value was determined by a measurement not affected by photobleaching to be 4 min. The longer decay constants of the two sites do not contribute to the chromatographic peak shape because their adsorption and desorption kinetics are too slow. They are valuable in showing that both materials have three types of strong adsorption sites with indistinguishable desorption kinetics, which means that fused silica is a good model for chromatographic silica gel.

Long adsorption times are ideal for single-molecule imaging because they light up a pixel for an extended period of time, seconds in this case. Diffusion, by contrast, causes the molecules to spread over many pixels. Using an imaging camera, researchers found that the silylated fused silica surface in contact with dilute DiI solution surface had occasional bright spots against a dim background (Figure 3-8a)<sup>79</sup>. Figure 3-8b shows the intensity as a function of time for the position of one spot in contrast to a position a few pixels away. Single molecules are clearly adsorbing and desorbing at the pixel for one spot, but not in the nearby pixels, which directly establishes that the strong adsorption sites are at fixed and rare positions on the surface. Figure 3-8c shows the analogous trace for another spot, which shows that the signal does not reach baseline, indicating there are

multiple molecules undergoing adsorption at this spot. Figure 3-8 shows how strong adsorption sites are thus normally clustered together; they are not just randomly sprinkled over the surface. Discovering this clustering of sites was possible because of single-molecule resolution; fluorescence correlation spectroscopy alone would have reported only the decay constants. From a surface science viewpoint, whatever is causing one strong adsorption site must typically cause many strong adsorption sites to be present. If these sites are, in fact, a result of very isolated silanols, something promotes these isolated silanols to concentrate within tiny submicroscopic regions on the surface.

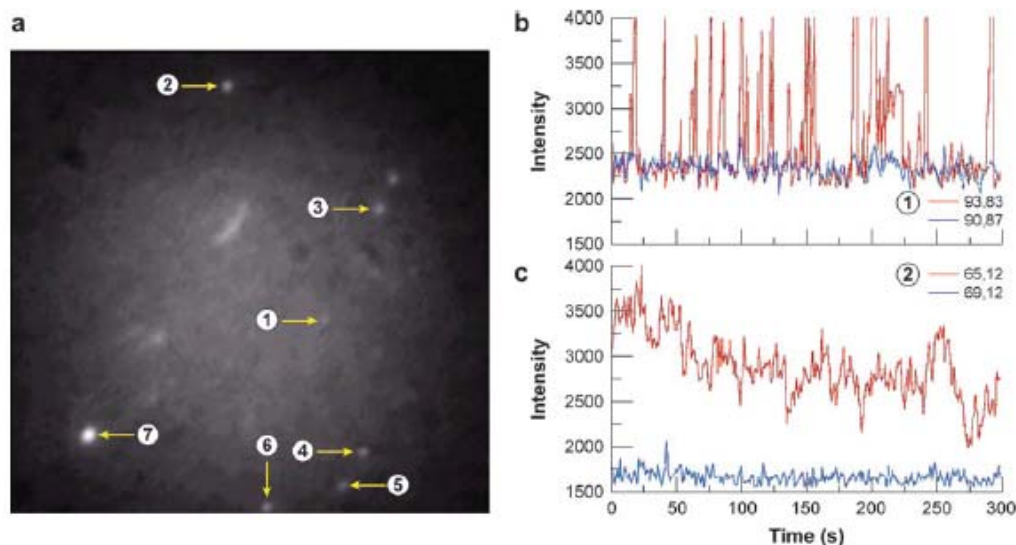


**Figure 3-8.** (a) Cumulative fluorescence micrograph of a silylated fused silica surface. Bright spots are labeled 1–6. (b) Intensity as a function of time for two positions in the image: red trace, position of spot 1; blue trace, a position a few pixels away. (c) Analogous trace for spot 2. Spots 3–6 display similar behavior (i.e., multiple molecules are adsorbing at any one time). Thus spots 2–6 are brighter than spot 1, even though they are further from the center of the beam. Spot 7 had no fluctuations; its intensity simply saturated the pixel at the maximum output of 4095 at all times. Autocorrelation of the sum of intensities from all fluctuating spots showed the same 2.6-s decay constant that was obtained for the fused silica in the confocal measurement for the same laser power. The behaviors of spots 2–7 revealed that typically there are multiple strong adsorption sites within a 200-nm pixel. Numbers separated by commas in b and c refer to pixel position. Figure taken from Ludes and Wirth 2002<sup>79</sup>.

## Topography

Comparison of fluorescence microscopy data with atomic force microscopy (AFM) data provides a hint about the cause of clustering of strong adsorption sites. AFM images of polished fused silica show that topographical marks are mostly submicroscopic divots, with occasional scratches<sup>80</sup>. The divots occur where polishing particles adhered to the surface and then peeled off a small amount of silica with them when they were washed away. The polishing particles are suboptical, which explains the suboptical sizes of the divots. The scratches are from polishing particles that are slightly larger than the mean of the size distribution, which imparts excessive force during the polishing process resulting in a scratch. Figure 3-9 shows a fluorescence image for DiI adsorbed to silylated fused silica and an AFM image of the same region<sup>9</sup>. The two images correspond remarkably well, revealing that the strong adsorption of DiI correlates with rough nanoscale topography. On a simple geometric basis, one could speculate that nanoscale surface curvature that is convex-up moves the surface silanols further apart to promote more isolated silanols, thereby explaining why the isolated silanols are spatially clustered: A polishing mark gives multiple points of surface curvature. However, current nanotechnology tools are insufficient to test this idea by direct observation.

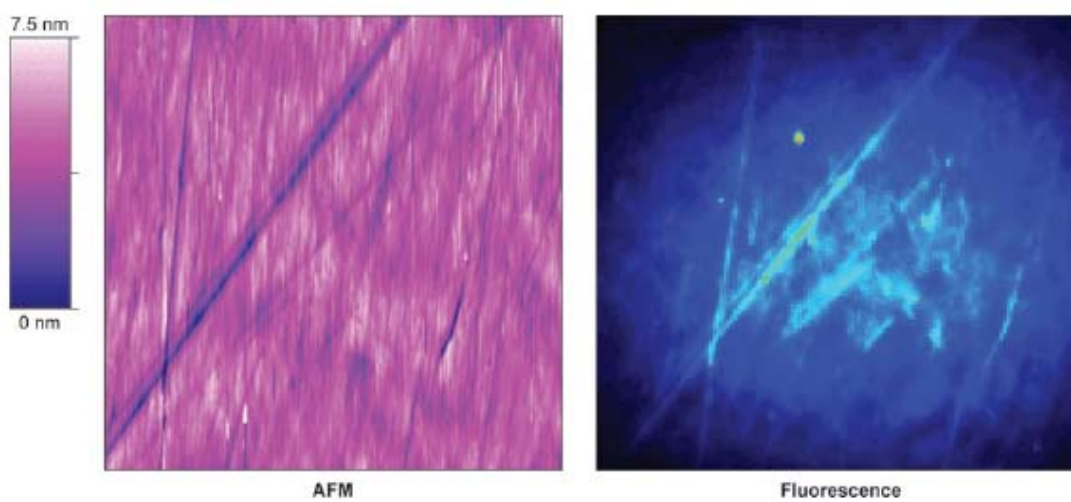
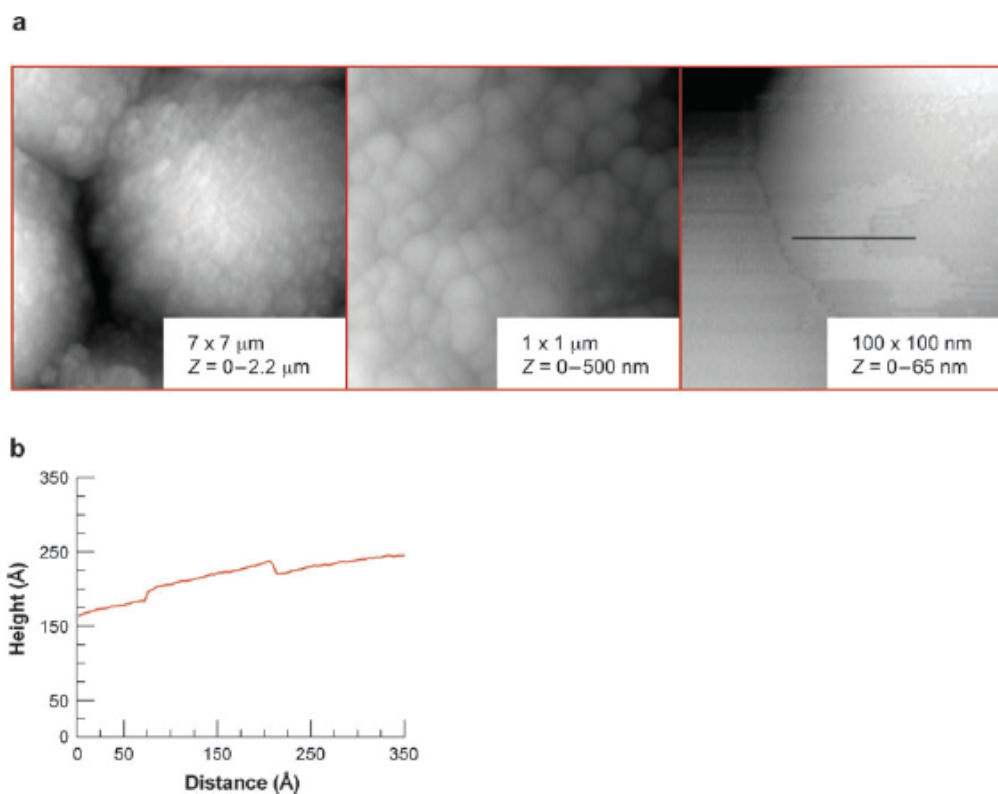


Figure 3-9. (a) Atomic force microscope (AFM) image and (b) fluorescence micrograph of the same region of a silylated fused silica coverslip in contact with dilute DI solution. An unusual region was chosen for the pair of intersecting scratches, making the correlation between the two images easy to detect. Figure taken from Wirth et. al. 1999<sup>9</sup>.

It is reasonable to ask if the topography of polished silica is at all relevant to that of silica gel. From the chromatographic data, it is known that strong adsorption sites are rare on silica gel, so if topography were the factor promoting isolated silanols, then one would have to argue that silica gel should be as smooth as fused silica, with rare topographical defects. Using an ultrasharp atomic-force-microscope tip, we<sup>10</sup> probed such materials. Figure 3-10 shows a series of AFM images of a high-quality silica gel, Agilent's Zorbax RX. This is the same material used for the chromatographic studies of DiI. This material consists of 100-nm silica colloids fused together at 900°C to form 5- $\mu$ m particles. The images in Figure 3-10 show that high-quality silica is quite smooth on the molecular scale. Thus silanols may become isolated by being on the edge of the plateau, and future studies will explore this possibility as force microscopy improves.

Chromatographic silica gel, itself, was probed by single-molecule spectroscopy, specifically using confocal microscopy to study spatially the dynamic equilibrium of single molecules of rhodamine 6G, a cationic dye<sup>81</sup>. Strong adsorption events were directly observed to be rare, and their average duration was 61 ms for this cationic dye. Over a long period of observation, virtually every pixel showed a strong adsorption event. This is in contrast to the fused silica measurements and is a result of the beam probing a much higher surface area for the porous particles. Improving chromatographic silica gels requires understanding the formation of silica in the sol-gel process. Single-molecule spectroscopy has been used extensively to probe the microheterogeneity of the adsorptivity and diffusion of dye molecules in thin films of silica and silicates<sup>82-87</sup>. These studies will be valuable in the design of future silica-based materials.



**Figure 3-10.** Atomic force microscopy data from Agilent's Zorbax RX silica gel. (a) The three micrographs show the 5- $\mu\text{m}$  bulk particles on three scales: 7  $\mu\text{m}$ , 1  $\mu\text{m}$ , and 100 nm, which is on the order of the size of the individual colloids. On the 7- $\mu\text{m}$  scale, the overall particle size is 5  $\mu\text{m}$ , and the constituent colloids can be distinguished. On the 1- $\mu\text{m}$  scale, the constituent colloids can be easily seen. On the 100-nm scale, the two colloids are fused together, showing that the colloids are extremely smooth. The black line on the image, drawn through a plateau, for the 100-nm scale corresponds to the height profile shown in b. The plateau has a height of 20 Å and a width at this point of 100 Å. The plateau is flat across the top on the molecular scale, as is the rest of the colloid. Figure taken from Legg and Wirth 2006<sup>10</sup>.

## Conclusions:

A series of instrumental and technological advances by many researchers made it possible to probe single molecules in dynamic equilibrium at surfaces. The results of the single-molecule experiments described above support the idea that the deleterious defects on chromatographic silica are isolated silanols. The single-molecule measurements revealed new information to add significantly to the understanding of these strongly adsorptive sites. Specifically, the experiments show that strong adsorption sites are at particular locations that can be spatially remote from one another, rather than uniformly distributed. This supports the idea that most silanols are not involved in strong adsorption. The single-molecule experiments further revealed that the strong adsorption sites are neutrally charged, rather than negatively charged from dissociated silanols, reinforcing the idea that these sites are isolated silanols. The single-molecule experiments revealed that the rare, strong adsorption sites are preferentially located at topographical irregularities rather than in smooth regions. This last finding poses a possible means to improve silica gel by controlling the smoothness of the silica surface in the processing of the silica gel. Topography is a new variable that had not been previously considered in improving silica gel.



## CHAPTER 4: PROBING TOPOGRAPHY AND TAILING FOR COMMERCIAL STATIONARY PHASES USING AFM, FTIR, AND HPLC

### Introduction

The purpose of this work was to apply AFM to investigate the nanoscale topography of chromatographic silica gel, to compare the adhesive force measured by AFM to isolated silanols measured by HPLC and the concentration of strong adsorption sites measured by nonlinear HPLC.

Previous studies of isolated silanols on silica were done on planar, fused silica coverslips. As was discussed in Chapter 3, the adsorption and desorption kinetics for the fused silica coverslips and chromatographic silica gel were the nearly identical. However, there was no data describing the surface topography of silica gel with nanometer scale surface characterization. If physical topography was indeed a factor influencing the formation of isolated silanols, one would expect similar features to exist on the commercial silica gel products.

Three high-quality commercial materials were chosen for this study because they have quite different morphologies from one another: Zorbax SB300, Symmetry 300, and Chromolith. The Chromolith is a monolithic silica while the Zorbax and Symmetry materials are 5  $\mu\text{m}$  spherical particles. The Zorbax and Symmetry materials have a reported pore size of 300 Å, and the Chromolith material has a pore size of 130 Å. Recently, Cabral and coworkers used AFM to determine pore size of a monolithic silica used for electrochromatography<sup>88</sup>, but to our knowledge, this is the first report of AFM

being applied to study a chromatographic bonded phase to determine the relationship between topography and chromatographic tailing.

The analyte, DiI, was chosen because of its high molar absorptivity of 150,000, L/mol-cm, which allows very low injected concentrations for assessing the nonlinear adsorption isotherm. It has a cationic group that is associated with tailing on silica-based materials; therefore, it is expected to adsorb to isolated silanols. The dye tails at analytical concentrations, and its tailing is reduced by lower pH, higher ionic strength, and endcapping, all of which are characteristic of basic drugs. Its permanent cationic charge allowed its use in studying the pH dependence<sup>65</sup>, and the prior knowledge about the tailing of this dye makes it a suitable choice for these studies.

Characterizing the roughness and topography of an irregular surface such as chromatographic silica gel is not straightforward. Scanning electron microscopy has been used in the past to characterize the bulk shape and size of silica particles. However, it is unfeasible to achieve nanometer resolution for silica gel even using field-emission SEM because of charging effects. The charging effects can be countered by coating the silica with gold, but this gold coating is on the order of 10 nm thick and completely masks any features smaller than that. Also, SEM is an imaging technique that does not provide quantitative height information.

These issues make AFM much more attractive than SEM as a tool to characterize nanometer scale surface features on silica gel. AFM probes with tips having a radius of curvature of 1 nm are commercially available, and they can be used to image features of

roughly the same size. It is features of this size, similar to the polishing marks and pits on fused silica coverslips, where we would expect the isolated silanols to be located.

#### Sample Preparation:

#### Materials

The three columns, Agilent Zorbax SB300-C18 ( $L = 15$  cm), Waters Symmetry 300 C18 ( $L = 5$  cm) and Merck Chromolith C18 ( $L = 2.5$  cm), were each purchased from the manufacturer. For AFM and FTIR, the materials were obtained by unpacking the chromatographic columns. Since the columns were used to obtain the HPLC data, the packing materials were rinsed and sonicated three times with methanol and dried under vacuum to remove any residual organics.

For AFM imaging, the samples of the chromatographic materials were attached to glass cover slips using double-sided scotch tape, and excess sample was blown off using compressed air. A series of images and adhesion force measurements were obtained at several sites on each sample. Each sample was moved several times to collect images and conduct adhesion force measurements at widely separated points. The measured adhesion force is dependent on the cantilever spring constant and deflection sensitivity. In this study, the spring constant was set to the median value reported by the manufacturer, and the deflection sensitivity was set based on the cantilever deflection when in contact with a hard surface.

All AFM images were exported as text files and then formatted; using an application written in C++, into a file that could be imported into ImageJ. The Surface Plot 3D plug-

in was used to create three-dimensional images with lighting and shadows to accentuate the surface structures. The fractal dimension was calculated using the “Cube Counting” method in Gwyddion

### FTIR

A sample of each chromatographic material was mixed with an appropriate amount of KBr using a mortar and pestle. The KBr was FTIR grade that was purchased from Alfa Aesar and used without further purification. The FTIR spectra were collected using a Nicolet 4700 FT-IR spectrometer with a Harrick “Praying Mantis” DRIFTS module. Measurements were taken using the 3 mm sampling cup. One thousand twenty four scans at a resolution of  $4\text{ cm}^{-1}$  were collected for each spectrum.

### HPLC

The solute used in this study was a cationic dye, 1,1'-didodecyl-3,3,3',3'-tetramethylindo – carbocyanine perchlorate (DiIC12 or simply DiI). It was obtained from Molecular Probes and was used without further purification. The solvent system used was 90/10 acetonitrile/water (v/v) with 0.1% trifluoroacetic acid (TFA) and 0.01M KCl, and it was used to make six DiI samples at 1.10, 10.2, 27.6, 78.5, 214, and 320 mM. The injection volume was 10  $\mu\text{L}$ , and the temperature was maintained at 20  $^{\circ}\text{C}$ . The acetonitrile came from EMD and was HPLC grade, and the water was purified to 18.0 MW using a Barnstead E-Pure water system. For each new column, the highest concentration sample was run repeatedly until the retention time stabilized, and then a

single run for each of the six samples was made to collect chromatograms for the entire series.

#### Results and Discussion:

Figure 4-1 presents atomic force micrographs for the three materials, each on scales spanning three orders of magnitude. On the largest scale, which spans 7  $\mu\text{m}$ , the 5  $\mu\text{m}$ , spherical particles are plainly seen for the Zorbax and Symmetry materials, while the monolithic character of the Chromolith material is obvious. At this scale, the nominally 2  $\mu\text{m}$  holes that allow mobile phase flow through the Chromolith material can be seen. The 5  $\mu\text{m}$  Zorbax particles are made by the fusion of nearly monodisperse colloidal silica spheres, and one can already begin to see these colloidal spheres on the largest scale. These individual colloids can be clearly seen in the middle image of Figure 4-1, and they are on the order of 100 nm in diameter. The tiny regions between the colloids are pores where analyte molecules can diffuse into and out of the silica gel. The Symmetry and Chromolith materials have a rougher and more irregular appearance on the 1  $\mu\text{m}$  scale than does the Zorbax material.

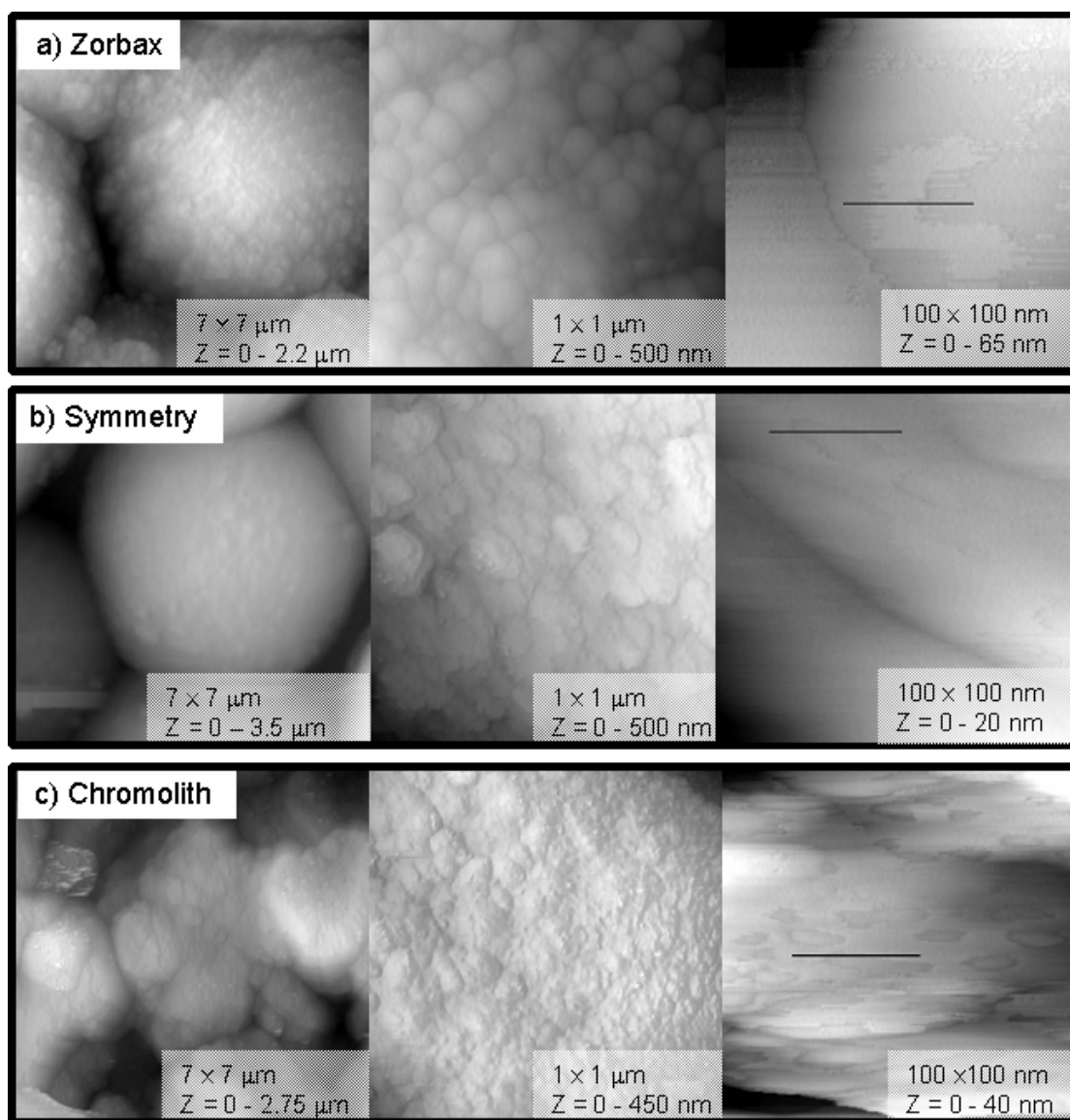


**Figure 4-1.** AFM images of each of the three materials on scales ranging over three orders of magnitude: a) Zorbax SB300, b) Symmetry 300, and c) Chromolith. The scan size and z-scales are indicated in each panel.

The materials are the most interesting on the 100 nm scale, which is the rightmost image in Figures 4-1a, b, and c. The materials are all as smooth as glass on this scale, and the fractal dimension of each material is measured to be 2.1, within the small errors listed in Table 4-1 (at the end of the chapter). The widely discussed view that silica gel is nearly three dimensional all the way down to the molecular scale is summarily dismissed by these images. At the 100 nm scan size, it is easy to see large, featureless regions, but even on this scale there is some structure. There are raised plateaus on the Zorbax material, and pock marks on both the Symmetry and Chromolith materials. A line scan of each of these materials across such features, spanning a range of 350 Å, is shown in Figure 4-2 with individual scans offset for comparison. For the Zorbax material, the slight curvature over the colloid is evident on this scale, and the raised feature is about 20 Å high. This would correspond to just a few silica tetrahedra. For the Symmetry material, the curvature is also evident, and the pockmark is about 10 Å deep. For the Chromolith material, slight curvature is evident, and the pockmark is about 30 Å deep. Even with these interesting features present, the materials are remarkably smooth, even smoother than the fused silica used previously to mimic silica gel surfaces<sup>9</sup>. The previous work demonstrated adsorption of a cationic dye to polishing marks on the fused silica surface, and the raised features on the Zorbax and pockmarks on the Symmetry and Chromolith products are surprisingly similar in size and shape to those polishing marks. This is an indication that the previous studies of adsorption and topography for fused silica are also relevant for chromatographic materials.

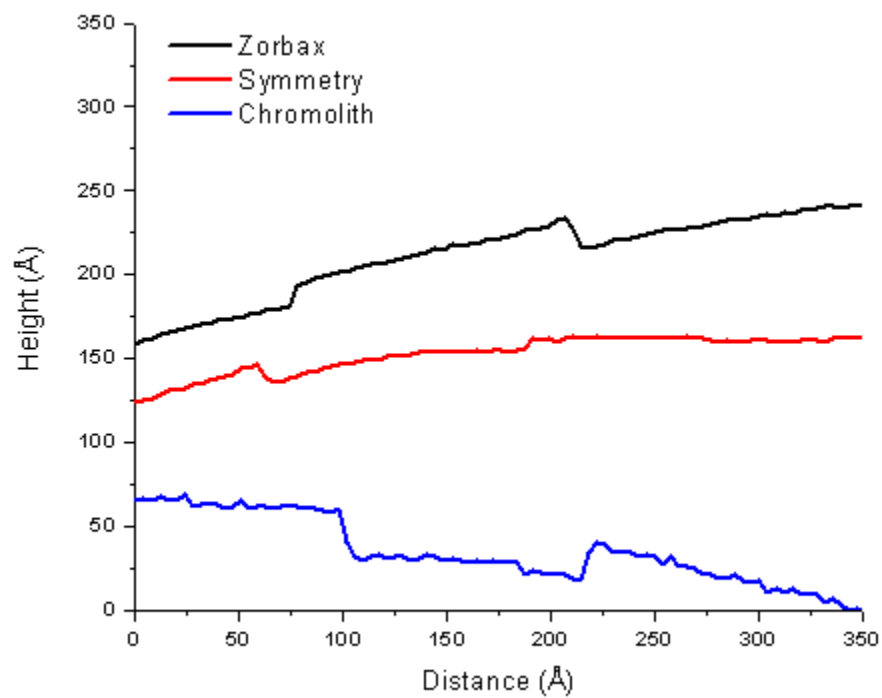


Figure 4-2. Line scans for each of the three materials. These correspond to the line segments in Figure 4-1 in the right-most panel of each series. The traces are artificially offset to facilitate comparison.



The extraordinary flatness at the 100 nm scale affords an opportunity to use an additional technique: chemical force microscopy. The AFM is used to measure the force required to pull a silicon tip from the silica surface after they have come into contact. The silicon tip has silanols on its surface, and they can be expected to hydrogen bond well to the isolated silanols on the chromatographic materials. Flat regions of the materials were deliberately chosen for the adhesive force measurements to avoid topographical contributions to the adhesive force through a higher area of contact. Multiple measurements were taken within a localized region, and measurements were taken at other, distant regions to obtain sufficient data for good statistics. Due to the irregular topographical surface features, it is not possible to collect an entire adhesive force map, on any size scale, to compare with the topographical image. However, the tip for adhesive force measurements has a radius of curvature of less than 100 Å, and this allows it to measure the adhesion for the flat regions of the materials.

The average adhesion force and standard deviation for several, spatially localized measurements are summarized in Table 4-1. The high precision among the multiple measurements of the surfaces indicates that the adhesive forces among the three materials are statistically distinguishable. The Symmetry material has a larger force of adhesion than does the Chromolith material, and the Zorbax material has a force of adhesion that is much smaller than either the Symmetry or the Chromolith.

Figure 4-3 shows the infrared spectrum for each of the materials. The methylene stretches from the hydrocarbons of the silanes absorb in the range of 2800 to 3000  $\text{cm}^{-1}$ . Each spectrum is scaled so that its asymmetric methylene stretch at 2920  $\text{cm}^{-1}$  is

proportional to the chain coverage of its surface. These coverages, obtained from the manufactures, are  $3.6 \mu\text{mol}/\text{m}^2$  for the Chromolith and Symmetry materials, and  $2.2 \mu\text{mol}/\text{m}^2$  for the Zorbax material. The differing amounts of overlap with the  $-\text{OH}$  stretching region were accounted for by interpolating the baseline around the methylene stretch region. The Symmetry spectrum, which is the tallest, had its maximum normalized to unity and the others were scaled with this same normalization constant. The peak for the isolated silanols is at  $3735 \text{ cm}^{-1}$ , and the spectra show that it is a small shoulder on the peak for hydrogen bonded silanols, which is the broad peak around  $3670 \text{ cm}^{-1}$ . This spectrum illustrates well that the isolated silanols are a small fraction of the total silanols. The spectra reveal that the Zorbax material has more hydrogen bonding among its silanols, as shown by the greater spectral intensity near  $3650 \text{ cm}^{-1}$  compared to  $3700 \text{ cm}^{-1}$ . This material is designed this way, where the lower silane coverage is intended to allow more hydrogen bonding and fewer isolated silanols. Adsorbed water gives a very broad peak centered at  $3400 \text{ cm}^{-1}$ , and the Zorbax material has more adsorbed water, as shown by the greater spectral intensity near  $3400 \text{ cm}^{-1}$  relative to the silanol spectral intensity near  $3650 \text{ cm}^{-1}$ . A comparison of the isolated silanol peak at  $3735 \text{ cm}^{-1}$  shows that the Symmetry material has a factor of two more isolated silanols than the Chromolith and Zorbax materials. The relative peak heights for the isolated silanols are listed in Table 4-1.

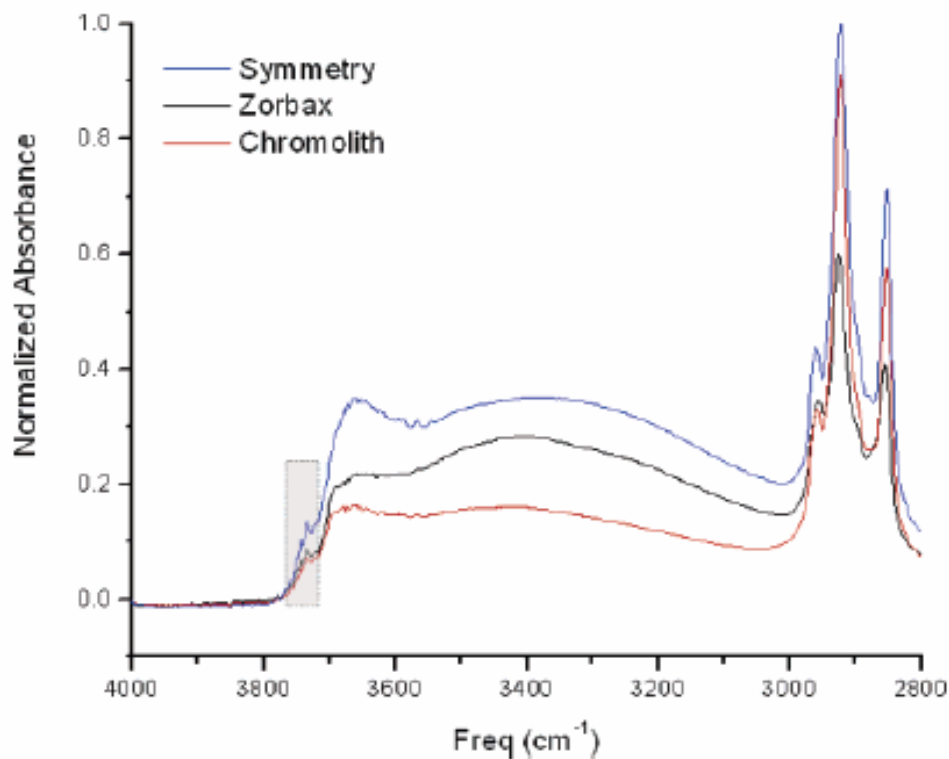


**Figure 4-3** Normalized Diffuse Reflectance Infrared Fourier Transform (DRIFT) spectra of each of the three materials after removing them from their columns and drying them under vacuum. Each spectrum is scaled to account for surface C18 coverage and then normalized using the Symmetry methylene stretch peak intensity.

The concentration of strong adsorption sites can be determined by combining nonlinear chromatography with modeling. Figure 4-4 shows experimental and simulated chromatograms for DiI solutions ranging in injected concentration from 1  $\mu\text{M}$  to 300  $\mu\text{M}$  for the three columns. The column lengths varied from 2.5 to 15 cm, so each chromatogram shows a time range of 30% of the retention time of the lowest concentration to provide a qualitative comparison of the amount of tailing. These chromatograms exhibit classic nonlinear tailing: as analyte concentration increases, the leading edge sharpens and shifts to earlier retention times, while the trailing side increasingly tails. The chromatograms are beginning to approach the appearance of nested similar triangles as concentration increases, indicating that the strong adsorption sites are becoming significantly saturated. Figure 4-5 shows chromatograms for the lowest injected concentration, 1  $\mu\text{M}$ , for each of the same three columns, and the peaks are nearly symmetric for the Symmetry and Chromolith columns. Figures 4-4 and 4-5 underscore an important concept in peak tailing; this phenomenon is inherently concentration-dependent, except in the unusual case of kinetic tailing.

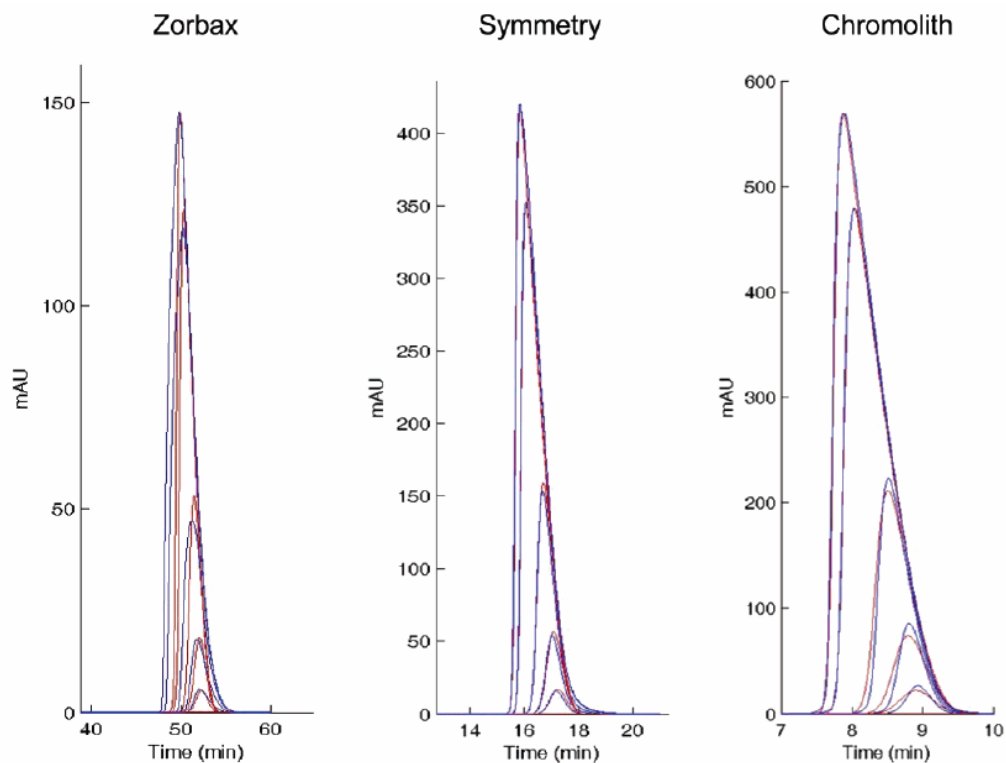


**Figure 4-4.** Chromatograms for DiI at varying concentration from 1 to 300  $\mu\text{M}$  for three columns: a) Zorbax SB300 (L=15 cm), b) Symmetry 300 (L=5 cm), and c) Chromolith (L=2.5 cm). The mobile phase was 90% acetonitrile/10% water with 0.1% TFA and 0.01 M KCl. The column temperature was 20  $^{\circ}\text{C}$ . Experimental chromatograms are in blue and simulated chromatograms are in red.

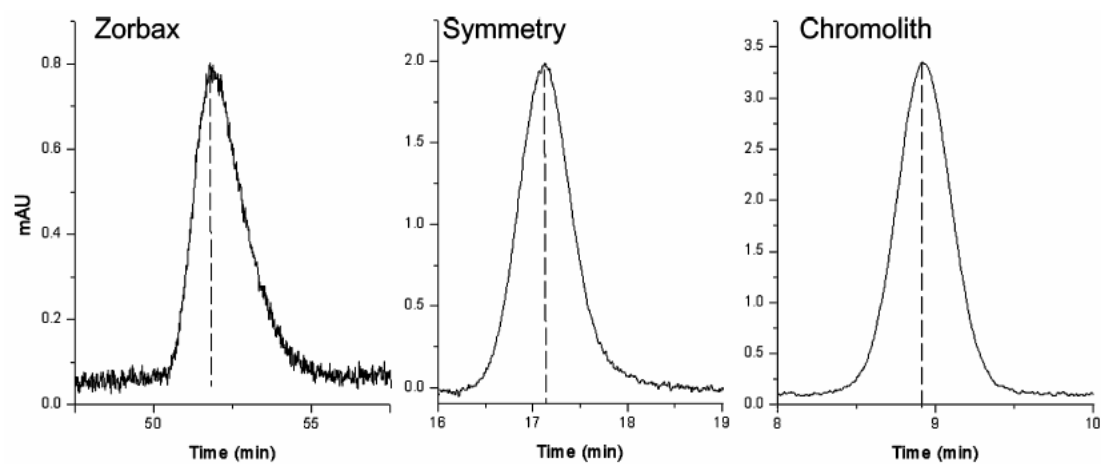


Figure 4-5. Rescaled chromatograms from Figure 4-4 for the lowest concentration of DiI, 1  $\mu$ M, for each for the three columns: a) Zorbax SB300, b) Symmetry 300, and c) Chromolith. A dashed line is drawn through the peak to illustrate peak symmetry.

The equilibrium constant (or partition coefficient) of the strong adsorption sites and their abundance can be determined by computer simulations of the chromatograms. However, the equilibrium constant,  $K$ , cannot be determined unless the condition of  $Kc \rightarrow 1$  is achieved; this is also the condition where significant tailing occurs. In the case of  $Kc \ll 1$ , only a lumped expression for  $\frac{\Gamma_{Strong}}{\Gamma_{Sat, Strong}} * K$  is obtained. Tailing occurs for both the Symmetry and Chromolith columns at the concentration of  $1/K = 10^{-4.5}$  M, and the condition necessary to determine  $K$  is achieved. Each material has an asymmetry factor above unity at this concentration, where the asymmetry factor is the ratio of trailing to leading half-widths at 10% of the peak height. For the weak sites, one cannot reasonably expect to learn  $K$  unless very high injected concentrations are used. Such high concentrations are used in preparative scale chromatography, which has been extensively researched by Guiochon and co-workers<sup>89</sup>.

The computer simulations account for the linear flow rates, the phase ratios, and the Peclet numbers, which were characterized separately. The phase ratios used in this study were determined from the manufacturers' supplied information to be  $8.9 \times 10^4$  and  $6.7 \times 10^4$  m<sup>2</sup>/L (total surface area of silica per volume of mobile phase) for the Chromolith and Symmetry, respectively. The results were determined to be insensitive to the difference in phase ratio. These units avoid any assumption about stationary phase thickness, and they readily allow calculations of strong site surface concentrations in units of mol/m<sup>2</sup>. The plots in Figure 4-4 show the simulated chromatograms plotted with the experimental chromatograms, and these show good agreement for the cases of Symmetry and

Chromolith. However, getting complete fits for the high and low concentrations simultaneously on the Chromolith column was not achieved. Satisfactory simulations for the Zorbax column could not be achieved due to the peak fronting issue discussed earlier. Peak fronting is not included in the computer model and is outside the focus of this work.

The number of strong adsorption sites and the equilibrium constants are two inputs in the computer simulation, and they were varied until a satisfactory match between the experimental and simulated chromatograms was reached. The values obtained from the simulated chromatograms of Figure 4-4, are listed in Table 4-1. The equilibrium constants for the strong adsorption process are comparable for the two columns,  $K=27,000$  and  $30,000$  for the Symmetry and Chromolith materials respectively. This slight difference in  $K$  is insignificant. The surface density of strong adsorption sites is what differs between the two columns:  $2 \times 10^{-9}$  and  $4.5 \times 10^{-9}$  mol/m<sup>2</sup> for the Chromolith and Symmetry materials, respectively.

The concentrations of strong adsorption sites are consistent with both the adhesion measurements and the FTIR results. The FTIR results show the abundance of isolated silanols on the Symmetry material is a factor of two greater than on the Chromolith material. The small abundance of strong sites revealed by the simulation is also consistent with the small abundance of isolated silanols shown in the FTIR spectrum. This reiterates an important concept in peak tailing that was introduced by Köhler and Kirkland<sup>90</sup>; it is the small population of isolated silanols, rather than the numerous associated silanols, that cause tailing.



The Zorbax column exhibits significant fronting at high concentrations, but this is not necessarily a general characteristic of this column. DiI is an unusual solute in that it has a pair of dodecyl chains, and if a DiI molecule adsorbed with its head group oriented toward the silica substrate in a region of sparse coverage of alkyl chains, the dodecyl chains would act as additional stationary phase. This would cause fronting by making adsorption more favorable due to C12-C12 interactions between DiI molecules. Fronting could be a coincidence of the choice of DiI combined with the unusual silane of the Zorbax Stablebond column. This silane has two bulky side chains rather than the methyl side chains of the Symmetry and Chromolith materials.

The adhesion measurement leads to a possible explanation for all of the anomalous behaviors of the Zorbax material: most of the isolated silanols are absent from the flat regions of the surface that are sampled in the adhesive force measurement. Instead, the isolated silanols are apparently concentrated in the pores where adhesive force measurements were not taken. Isolated silanols within the pores would impart a reduced contribution to the adhesion measurement. The AFM topographical images actually allow quite a detailed view of the inside of a pore: the rightmost image of Figure 4-1a shows the junction of two colloidal spheres, which is tantamount to looking into a pore with the third colloidal sphere removed. The image reveals that the junction is not smooth at all: a seam exists where the two colloidal spheres are fused together in a sintering process that increases the rigidity of the material<sup>91</sup>. For reference, the line in the image used to indicate the line scan, is 350 Å, just larger than a 300 Å pore, hence the image is rich in detail below the pore size. Figure 4-6a shows the right most image of

Figure 4-1a, this time with lines going across the junction to indicate where line scans were measured, and the line scans are shown in Figure 4-6b. The line scans show that the junction of the two colloidal spheres has a bump and an indentation. Apparently during the sintering process, the material does not flow smoothly to form the colloid junction. Line scans are shown for five different positions, indicating that the combined bump and indentation in the substrate occurs everywhere that the two colloids are fused. The indentations are on the order of 20 Å wide and 15 Å deep. The indentations are undoubtedly somewhat deeper than they appear, due to convolution with the HiRES tip, which has a 10 Å radius of curvature.

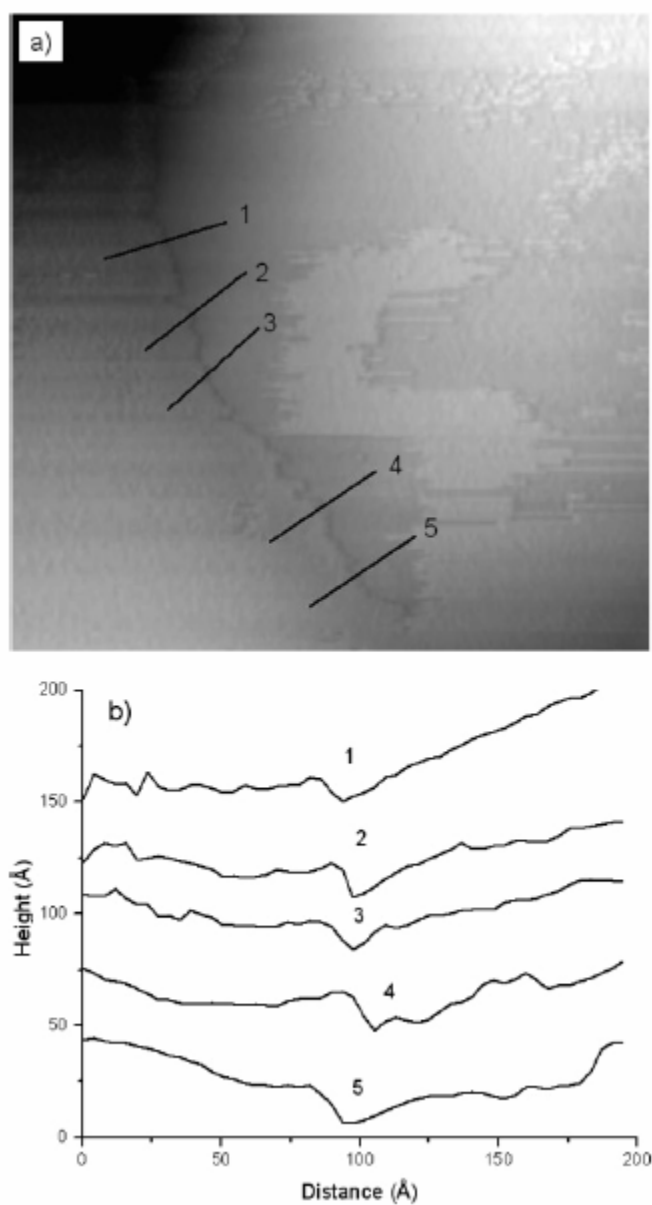


**Figure 4-6 a) AFM image of the junction of two Zorbax colloid particles from Figure 4-1a to depict the positions for multiple line scans. b) Multiple lines scans across the junction, with the numbers corresponding to part a. The traces are artificially offset to facilitate comparison.**

Isolated silanols at the junctions between colloidal spheres could be the cause of tailing and fronting on the Zorbax material, but this is speculative without further experimentation. As speculation, the raised region on the left side of the indentation for each scan in Figure 4-6b gives a concave-out geometry, which would reduce the silane density to make it favorable for the hydrocarbon chains of the dye to cluster. The curvature on the bump is the same as that of a sphere of only 10 Å in diameter. At this molecular size scale, the distances among the hydroxyl groups of the surface silanols would fan out, giving statistically more isolated silanols. It could similarly be possible for isolated silanols to be prevalent at the edges of the nanoscale features on the Chromolith and Symmetry materials that are evident in Figure 4-2. It would be interesting to image these regions by chemical force microscopy to test whether the adhesion is higher in these nanoscale bumps, but such a measurement awaits further advances in atomic force microscopy.

## Conclusions

Ultrahigh topographical resolution has been achieved for commercial chromatographic materials: chemically modified silica gel. The materials are as smooth as glass on the distance scale of less than 100 nm. Adhesive force, FTIR and HPLC results are consistent in showing that Symmetry300 has twice as much adhesion, isolated silanols, and strong adsorption sites, respectively, supporting Köhler and Kirkland's ideas that isolated silanols cause tailing for silica-based chromatographic materials. Despite the nanoscale smoothness of the materials, topography could play a role in promoting

isolated silanols because molecular-scale bumps are present on the surface, and these would increase the distances among silanols perhaps enough to increase the number of isolated silanols. The Zorbax material showed very low adhesion within its flat regions, indicating that silica gel with significantly lower adsorptivity is possible to achieve.

	Chromatography		FTIR	AFM	
Silica Sample	Density (mol/m <sup>2</sup> )	K <sub>s</sub>	Relative A @ 3735 cm <sup>-1</sup>	Fractal Dimension	Adhesion Force (nN)
<b>Zorbax SB300<sup>1</sup></b>	NR <sup>2</sup>	NR <sup>2</sup>	1	2.12 ± 0.05	x = 4.8, s = 0.9, N = 19
<b>Symmetry 300</b>	4.5 x 10 <sup>-9</sup>	27,000	1.4	2.13 ± 0.04	x = 23, s = 1, N = 13
<b>Chromolith</b>	2 x 10 <sup>-9</sup>	30,000	0.8	2.14 ± 0.06	x = 14.1, s = 0.6, N = 18

**Table 4-1. Summary of parameters from HPLC, FTIR and AFM. From HPLC, the surface density of strong adsorption sites and K<sub>s</sub> is the partition coefficient for adsorption to the strong sites. The relative absorbance from FTIR at 3735 cm<sup>-1</sup> corresponds to the isolated silanols. The AFM data include fractal dimension and force of adhesion, where the average (x), standard deviation (s), and number of measurements (N) are listed.**

<sup>1</sup> exhibited peak fronting.

<sup>2</sup> NR (not reported): simulations do not fit well

## CHAPTER 5: SINTERED SILICA COLLOIDAL CRYSTALS WITH FULLY HYDROXYLATED SURFACES

### Introduction:

Silica particles of controlled submicron size and low polydispersity<sup>17</sup> can be deposited on solid substrates to form highly ordered face-centered cubic crystals<sup>92</sup> with thicknesses ranging from two layers to several hundred layers<sup>93</sup>. As a photonic material, a colloidal crystal gives strong Bragg diffraction at a wavelength determined by the particle diameter, refractive index, and crystal thickness<sup>93, 94</sup>. There has been widespread interest in silica colloidal crystals as photonic materials for many years, and this has recently been reviewed<sup>95</sup>. New applications of colloidal crystals are now emerging, such as supports for lipid bilayers<sup>96</sup>, high-surface area substrates for microarrays<sup>97</sup>, patterned supports for microarrays<sup>98, 99</sup> microreactors<sup>100</sup> and media for chemical separations<sup>101-105</sup>. Chemical modification of silica colloidal crystals has been reported using silylation<sup>106</sup>, and silylation followed by atom-transfer radical polymerization<sup>107</sup>.

These many emerging applications place new demands on the chemical characteristics of colloidal crystals. For example, their use as separation media and as substrates for microarrays and lipid bilayers, require that the surfaces have controlled adsorptivity. Silica is well established in the field of chemical separations, including chromatographic silica gel and silica capillaries, because of its controlled adsorptivity. However, simply having a substrate comprised of silica does not guarantee high-performance separations. Subtle differences in surface treatment can result in severe

zone broadening in separations, and nonspecific adsorption to the substrate is always an issue with microarrays<sup>108</sup>. It was a breakthrough made in the 1980's that led to the high quality surface on silica gel that is used today<sup>90</sup>. Considerable processing is also required to improve the surface quality of silica capillaries before use in electrophoresis<sup>109</sup>. To date, there have been no studies specifically addressing the surface properties of silica particles per se. For preparing colloidal crystals, it is known that these silica particles must be calcined to shrink their volumes prior to deposition to avoid large cracks in the final crystal<sup>110</sup>. Furthermore, calcination at different temperatures results in particles with different refractive indices, and the particles with a lower refractive index are known to slowly absorb solvent<sup>111</sup>. One can reasonably assume that the particles have to be solid to prevent unwanted adsorption. Heating to 1050 °C, which causes sintering, results in particles with refractive indices comparable to that of fused silica<sup>111</sup>, indicating that they are solid silica, but simply sintering crystals made from untreated silica colloids results in an unacceptable amount of cracking in the crystal lattice.

Forming colloidal crystals with previously calcined particles and then sintering has not been investigated previously. If the crystal lattice remains intact after sintering the calcined particles, these crystals would likely exhibit high performance in chemical separations due to the reduction in mechanical defects, and in optical applications due to higher refractive indices of the particles.

The purpose of this chapter is to investigate whether the silica particles approach the density of fused silica when crack-free sintered colloidal crystals are made. We combine FTIR, SEM, optical microscopy, UV-visible spectroscopy, and refractive index



measurements using index-matching fluids to characterize the materials. We also investigate the conditions needed to completely rehydroxylate the surfaces of the particles.

#### Sample Preparation:

The Stöber method was used to synthesize the particles<sup>17</sup>. The silica particles were heated to 300, 450, and 550 °C, in succession, for 12 hr at each temperature. After the three calcination steps were complete, the particles were re-suspended in ethanol by sonication, and the suspension was allowed to rest at ambient temperature for 24 hours to allow any aggregates to settle.

We prepared the colloidal crystal by evaporative deposition of a colloidal slurry onto fused silica slides. A colloidal suspension was prepared by sonication of calcined silica particles in ethanol for 2 hours. (0.1 g colloid in 20 mL ethanol). The cleaned slides were placed vertically into 30 mL glass beakers containing approximately 20 mL of the colloidal suspension and incubated under a 100-W incandescent lamp for 20 hours to accelerate the evaporation of ethanol. For FTIR analysis, polished silicon slides, rather than silica slides, were used, but the same processing procedures as for the fused silica substrates were used.

The fused silica slides bearing the silica colloidal crystals were sintered in a furnace at 1050 °C for 12 hours. The crystal was then allowed to cool gradually over a period of 3-4 hours within the furnace. This slow cooling was necessary to avoid sudden, large temperature changes, which might cause cracks in the material. The sintered material was placed in a solution of tetrabutylammonium hydroxide of pH 9.5 at 60 °C for 24

hours. to rehydroxylate the surface. Following the rehydroxylation, the surface was rinsed with deionized H<sub>2</sub>O, 1 M nitric acid, methanol, and then deionized H<sub>2</sub>O, in succession.

To demonstrate that the surface was chemically reactive, a brush layer of polyacrylamide with nominal thickness of 10 nm was grown by atom-transfer radical polymerization<sup>112-115</sup>. The clean sintered material was placed in a 250 mL flask that contained 1.0 mL of (chloromethylphenylethyl)dimethylchlorosilane (Gelest, Morrisville, PA) and 1.0 mL of pyridine in 100 mL of dichloromethane, and the reaction was allowed to proceed overnight at reflux-temperature. The colloidal crystal was modified with polyacrylamide by free radical polymerization with a CuCl/CuCl<sub>2</sub>/Me<sub>6</sub>TREN catalytic system at room temperature, using a previously reported procedure<sup>115</sup>.

Optical micrographs were obtained using a Nikon Eclipse TE2000-U microscope with a Nikon model C-SHG1 mercury lamp power supply, and a Photometrics, Cascade 512B CCD camera. Field-emission SEM images were obtained using a Hitachi S-4500 using Thermo-Norm Digital Imaging/EDS.

## Results and Discussion:

Figure 5-1a shows an optical micrograph for a sintered colloidal crystal, which had been previously calcined. To demonstrate that cracks would be evident on this scale, Figure 5-1b shows the optical micrograph for a colloidal crystal made from the same particles but without any prior calcination. The latter crystal was not sintered, therefore, the cracks evident in the image were the result of shrinkage at room temperature. This is

in stark contrast to the triply calcined materials of Figure 5-1a, which even after sintering, show no cracks that could be resolved by the optical microscopy.

The underlying processes that occur upon calcination and sintering were monitored by FTIR measurements. The infrared spectra corresponding to the As Made, Calcined, and Sintered particles are shown in Figure 5-2. The peaks for the reagents are reduced with progressive heat treatment. The large, broad peak in the O-H stretching region, with a maximum near  $3400\text{ cm}^{-1}$ , corresponds to water on the surface or trapped within the colloid. Based on the relative intensities at this frequency, the calcination step eliminates approximately three times as much water as the sintering step. By the end of the sintering step there is virtually no detectable water. The C-H stretches from  $2800$  to  $2900\text{ cm}^{-1}$  correspond to the ethoxy groups of TEOS. This peak is small, and it disappears after calcination. The broad peak for the hydrogen bonded silanols ( $3600\text{ cm}^{-1}$ ) decreases with calcination and then decreases even further upon sintering. The peak for the isolated silanols ( $3745\text{ cm}^{-1}$ ) becomes sharper and more prominent as the sample is calcined and then sintered. The siloxane peaks resulting from condensation of the silanols are from  $1868$  to  $1990\text{ cm}^{-1}$  in the infrared spectrum<sup>116</sup>, and these are shown in Figure 5-2 to increase upon calcination, and then further upon sintering. Overall, the sintered material has lost almost all water and associated silanols, and its spectrum is dominated by the siloxane peaks, indicating that it has approached the chemical composition of fused silica.

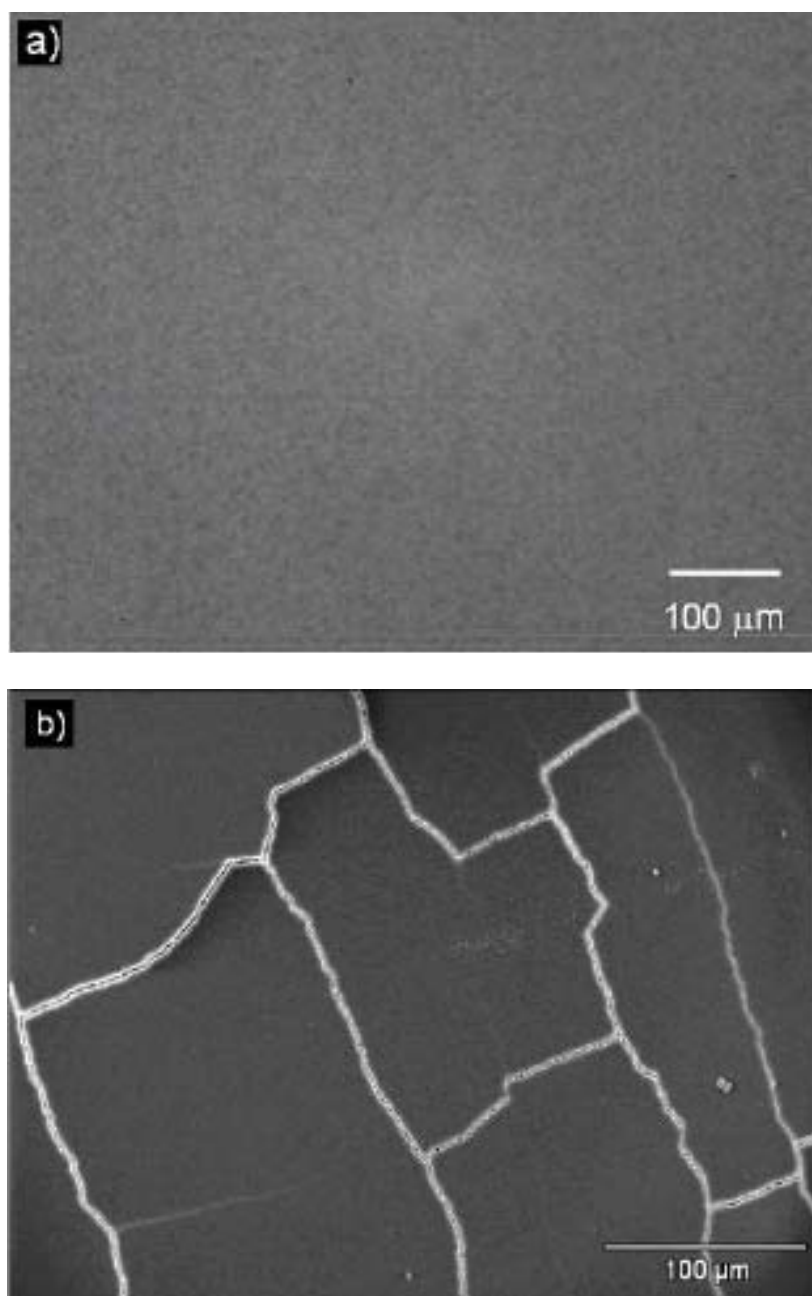


**Figure 5-1.** Optical micrographs of a) sintered silica colloidal crystal with three prior calcination steps, and b) colloidal crystal with neither calcinations nor sintering, shown to illustrate cracks.

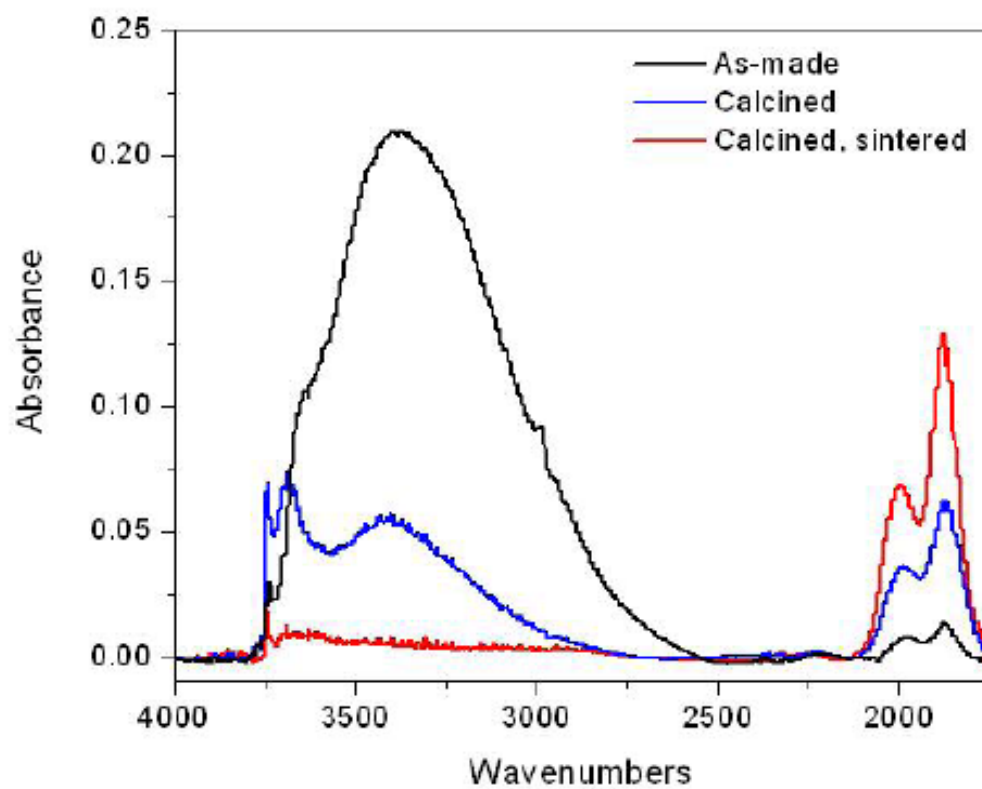


Figure 5-2. FTIR spectra of silica colloidal crystals made using particles with no calcination (As - Made), using calcined particles, and using calcined particles that were sintered after the crystal was formed.

The progressive loss of water shown in the infrared spectrum upon heat treatment should correlate with a corresponding decrease in the sizes of the particles, and this was confirmed by SEM. Figure 5-3 illustrates, from a small section of two SEM images, how scanning electron microscopy was used to measure colloid size. A comparison of as-made and calcined particles shows that the latter are distinctly smaller, as indicated by putting an arrow of the same size on each of the images. For the [111] plane of the fcc lattice, there are rows of particles along one crystal axis that lie along a line. The crystal domains are sufficiently large and sufficiently crystalline that many such lines of five particles in length can be found and measured to determine the colloid diameter with a precision of a few nm. The sizes of the particles, as determined by SEM, at each step in the heating process are listed in Table 5-1. There is a greater decrease in diameter going from As Made to Calcined than there is from Calcined to Sintered. The calculated change in colloid volume is approximately three times higher upon calcination than it is upon sintering, which is in agreement with the relative changes in the intensities of the water peaks in the infrared spectra.

A decreased colloid size is expected to be associated with an increase in colloid density, and therefore an increase in refractive index. The data bear out part of this expectation, as shown in Figure 5-4. The refractive index measurements shown were determined using the method described in Chapter 2. The As Made particles exhibit a distribution of refractive indices, indicating that the material is heterogeneous on the optical scale. The Calcined particles have a lower and better defined refractive index, 1.440, compared to the As Made colloids. The decrease in refractive index suggests that

while the calcination removes water, at least part of the volume is filled by air rather than by silica. Upon sintering, the refractive index increases to a value of 1.454, which approaches the refractive index of fused silica, 1.458. Garcia-Santamaria et al. showed a similar result<sup>111</sup>, but the particles were not treated sequentially in their case, hence it was not previously known if the lower index particles obtained upon calcination could be converted to higher index particles by follow-on higher temperature sintering. Our result plainly shows that the conversion to the higher index colloid is achieved. Using an extension of the Lorentz-Lorenz relation for refractive indices of mixtures<sup>116</sup>, the refractive index of the calcined particles indicates that they are 5% air by volume. The sintered particles are only 0.7% air by volume, meaning that they are nearly equivalent to fused silica.

Sintering differs from calcination in an important way: sintering is performed above 1000 °C, which is sufficient to cause flow of silica on the surface. The existence of fusion points among the particles after sintering is established in the SEM image of Figure 5-5, which shows the divots and blebs remaining after a sintered colloidal crystal was snapped in half. The entire material becomes quite rugged after sintering, being able to survive ultrasonic cleaning for hours. The many attachment points among particles explain why the material is now durable. The flow of silica on the surface during sintering might be responsible for filling in the free volume in the particles.

<b>Material</b>	<b>Refractive Index (<math>\lambda = 589</math> nm)</b>	<b>Colloid Diameter (nm)</b>	<b>Predicted Bragg Peak (nm)</b>	<b>Observed Bragg Peak (nm)</b>
As Made	1.44 – 1.46	$208 \pm 5$	448 - 470	454 (broad)
Calcined	1.439	$197 \pm 8$	417 - 452	425
Sintered	1.454	$188 \pm 10$	393 - 437	414
Rehydroxylated	1.454			409

**Table 5-1. Summary of data for particles after the indicated treatment.**



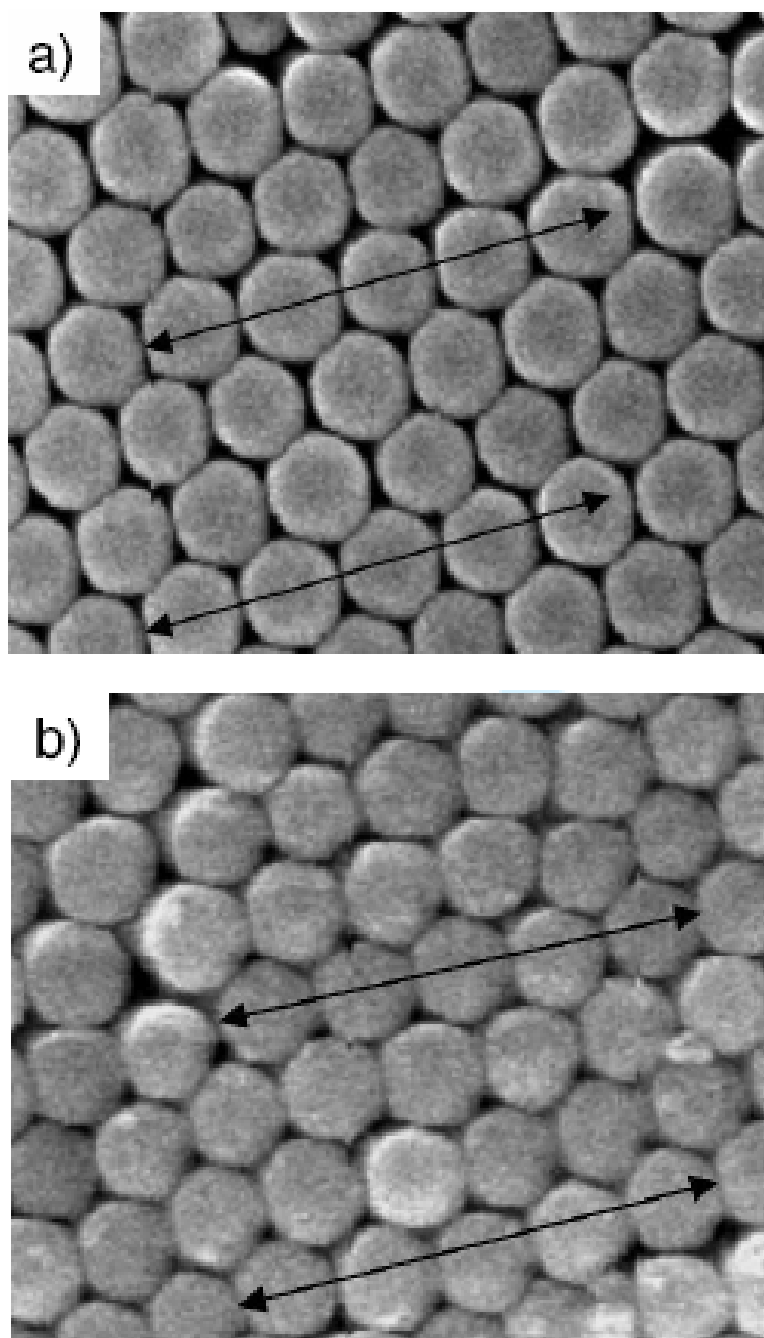


**Figure 5-3.** SEM images of colloidal crystal made from a) As Made particles, and b) Calcined particles. The arrow size is the same in each panel to indicate that the particles in panel b are smaller.

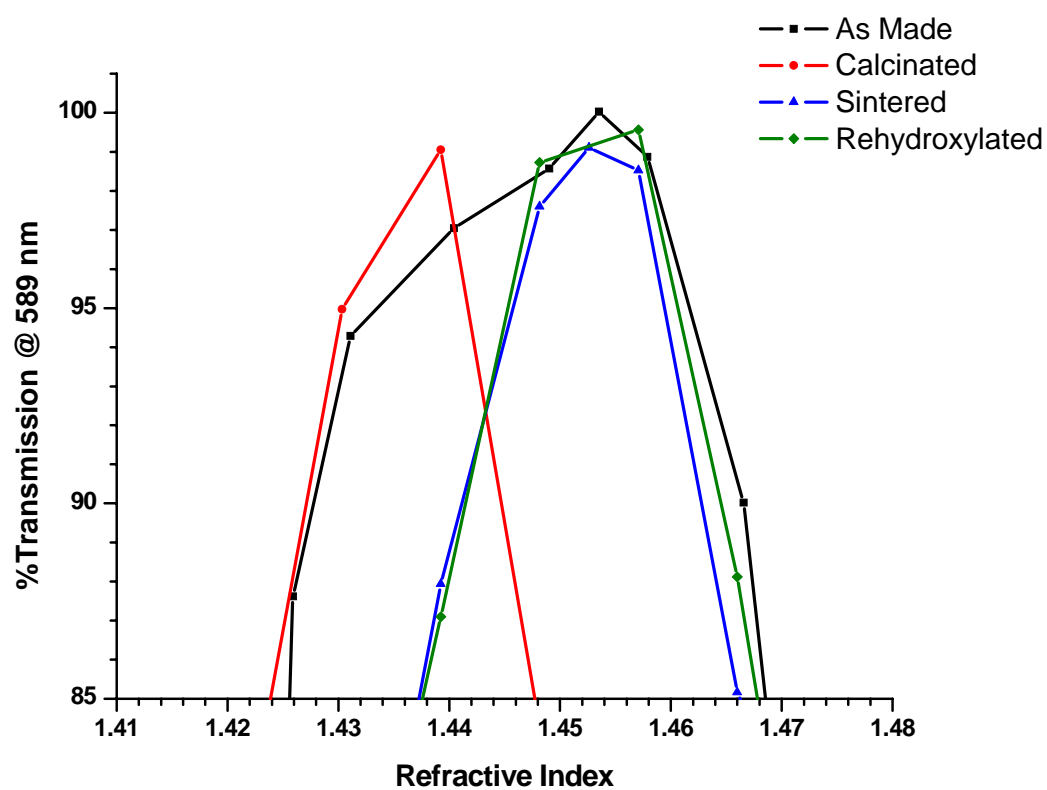
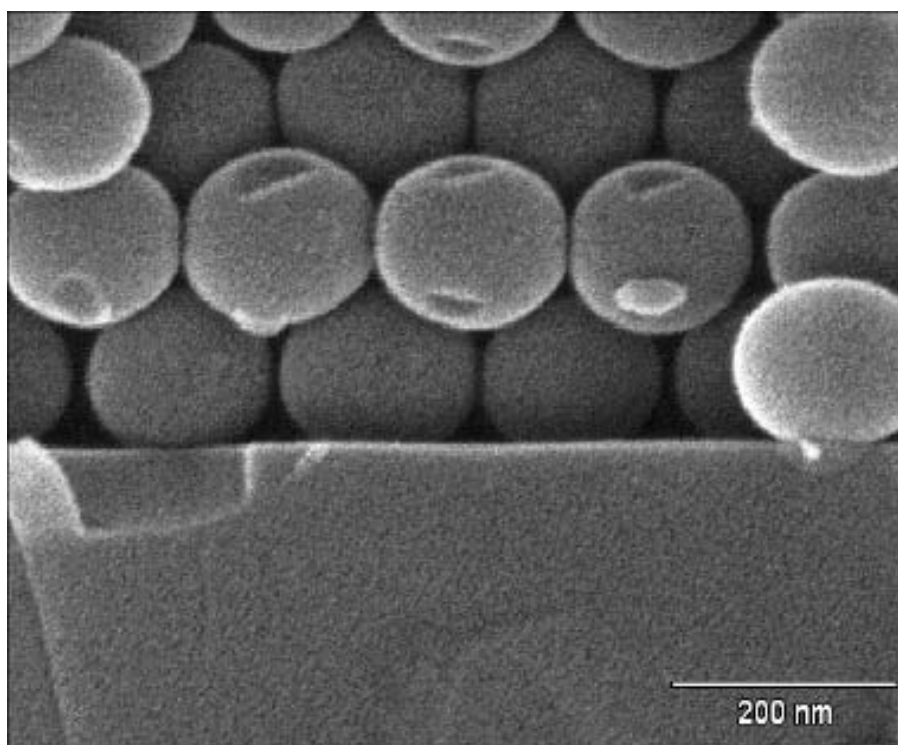


Figure 5-4. Optical transmission measured at 589 nm for colloid slurries as a function of the refractive index of the solvent used for the slurry. Four different preparations of particles were studied, as denoted by the labels in the inset.



**Figure 5-5.** Field-emission SEM micrographs of a sintered silica colloidal crystal showing the attachment points after breaking the crystal.

An independent assessment of refractive index can be obtained by measuring the photonic bandgap, which is a sharp band in the absorption spectra due to Bragg diffraction. For fcc crystals, the lattice spacing,  $d_{111}$ , is  $0.816 \cdot d$ , where  $d$  is the particle diameter<sup>94</sup>. The lattice spacing is related to the peak wavelength for Bragg diffraction,  $\lambda_{peak}$ .

$$m \cdot \lambda_{peak} = 2 \cdot d_{111} \left( n_{eff}^2 - \sin^2 \theta \right)^{1/2} \quad (5-1)$$

In Eq. 5-1,  $m$  is the order of diffraction, which is 1 in this case,  $\theta$  is the angle between the incident light and the normal to the diffraction planes, which is  $0^\circ$  in this case, and  $n_{eff}$  is the mean refractive index of the colloidal crystal. Figure 5-6 shows a comparison of the visible transmission spectra for a colloidal crystal using As Made, Calcinated, and Sintered particles. The Bragg peak is evident in each spectrum, indicating crystalline order. The Bragg peak is broad for the As Made particles, which is consistent with wider distribution of colloid sizes. The Bragg peak shifts 29-nm to the blue upon calcination, and it shifts another 11 nm further to the blue upon sintering. According to Eq. 5-1, this shift is qualitatively consistent with the progressive shrinkage of the particles with heat treatment. One can assess the quantitative agreement between the transmission spectra, the colloid sizes, and the refractive index data by calculating the position of the Bragg peak. The refractive indices of the particles,  $n_{silica}$ , and air,  $n_{air}$ , combine to give  $n_{eff}$ , where the volume fraction of colloid in an fcc lattice is  $0.74^{117}$ .

$$n_{eff}^2 = 0.74 \cdot n_{silica}^2 + 0.26 \cdot n_{air}^2 \quad (5-2)$$

The positions of the observed Bragg peaks are listed in Table 5-1, and they agree well with values calculated using the refractive index data. The observed positions of the Bragg peaks provide independent confirmation of the refractive indices of the particles.

Figure 5-6 shows that sintering slightly reduces the height of the Bragg peak, indicating a small decrease in crystallinity. To assess how crystalline the material is, SEM images for the sintered material are shown in Figure 5-7 over a wide field of view. The material was snapped in half to allow a cross-sectional view. From Figure 5-7a it is evident that the material is quite crystalline, and the crystal planes extend through the depth of the crystal. Figure 5-7b shows the material over a wider range, which shows lines indicating a slight gap in the crystal. These gaps are likely caused by the small shrinkage of the particles, and their presence is consistent with the slightly attenuated Bragg peak.

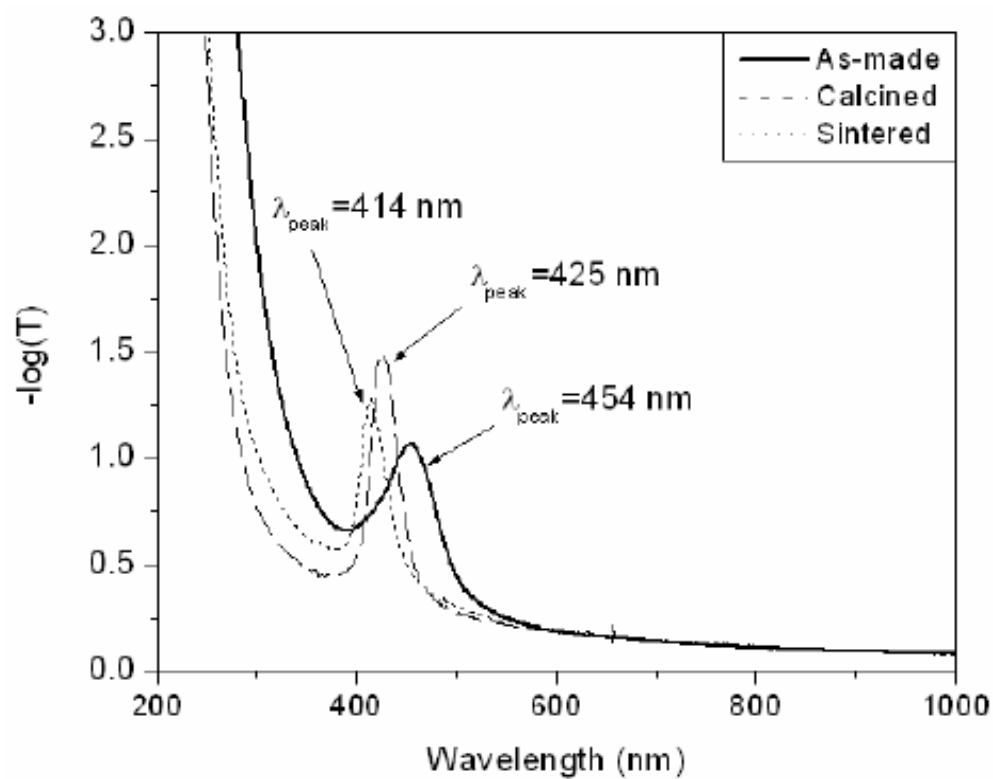
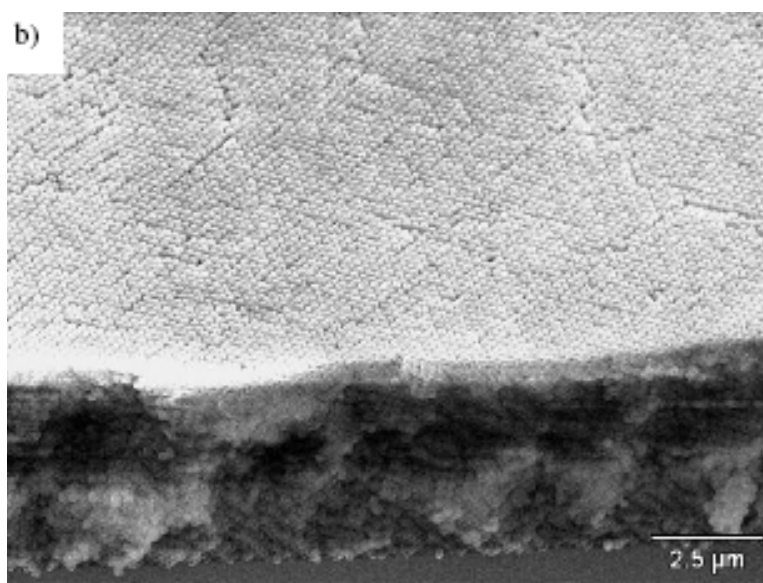


Figure 5-6. Transmission spectra of silica colloidal crystals, including As-Made, Calcined and Sintered, as indicated. The positions of the Bragg peaks are given.



**Figure 5-7. SEM images at two different magnifications for a sintered colloidal crystal snapped in half. a) higher magnification to show the crystal planes, b) lower magnification to show the outlines of domain boundaries.**

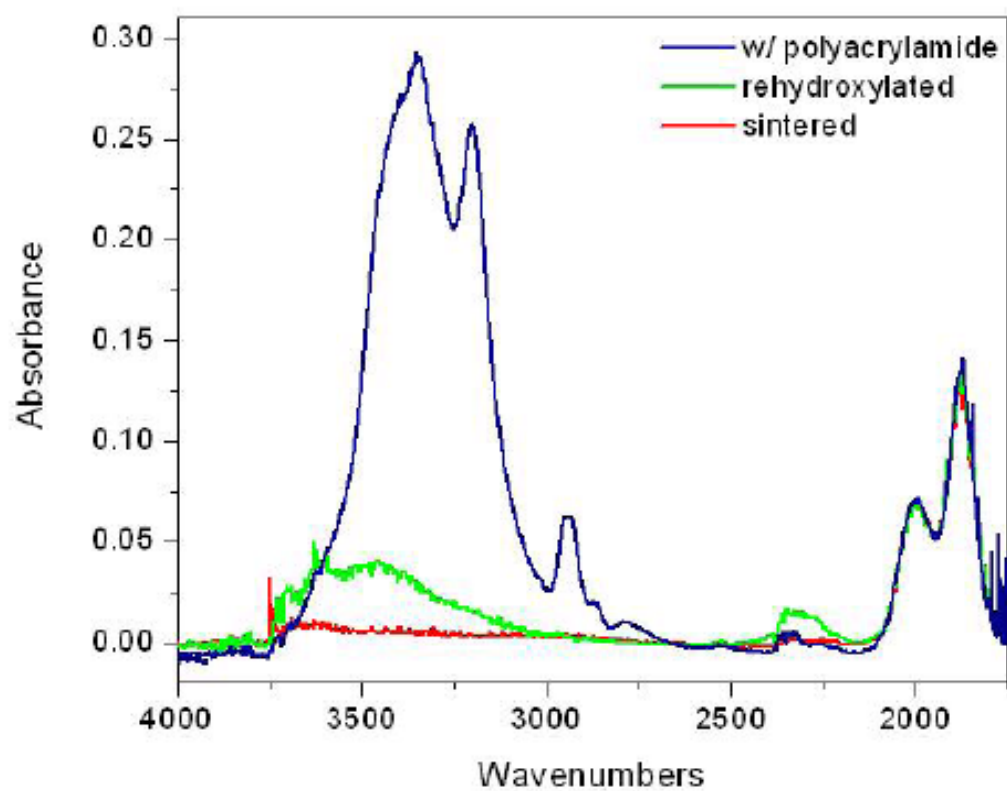


Figure 5-8. Infrared spectra for a colloidal crystal after sintering, after rehydroxylation, and after growth of a polyacrylamide brush layer, as labeled.



Optimal chemical modification of the silica surface via reactive silanes requires complete rehydroxylation of surface siloxanes to surface silanols<sup>63</sup>. This process requires a relatively aggressive chemical treatment involving extended submersion in a mildly basic, aqueous solution at elevated temperatures. To demonstrate that the sintered silica crystal particles can be suitably modified in such a manner, rehydroxylation of the sintered colloidal crystal was preformed to convert surface siloxanes to surface silanols. Figure 5-8 shows infrared spectra of a sintered colloidal crystal before and after rehydroxylation. The infrared spectrum for the sintered colloidal crystal is shown for reference. The spectra confirm that rehydroxylation provided a large gain in the peak area for hydrogen-bonded silanols centered at  $3600\text{ cm}^{-1}$ . The amount of water adsorbed to this newly hydrophilic surface also increases, as shown by the broad band centered at  $3300\text{ cm}^{-1}$ . The peak for the isolated silanols has become virtually undetectable, indicating that the surface is now fully hydroxylated. The infrared spectra thus establish that the surface silanols are regenerated, and these surface silanols are presumably available for reactions to chemically modify the colloidal crystal surfaces for end-applications.

To demonstrate that these particles can be chemically modified without compromising the integrity of the crystal, a chlorosilane bearing a benzyl chloride group was reacted with the surface to serve as an initiator for atom-transfer radical polymerization of acrylamide<sup>114, 118, 119</sup>. The resulting infrared spectrum of the polyacrylamide modified colloidal crystal is shown in Figure 5-8. New peaks related to the polymer include the C-H stretch region near  $2900\text{ cm}^{-1}$ , which arise from the polymer

backbone, are evident, as well as a peak from the N-H stretch at  $3200\text{ cm}^{-1}$ . The spectrum indicates that there is water solvating the hydrophilic polymer chains.

The Bragg peak of a colloidal crystal after rehydroxylation and after chemical modification were monitored, and the spectra are shown in Figure 5-9. The UV-visible spectrum for a sintered colloidal crystal before chemical modification is also shown for reference. Upon rehydroxylation, the Bragg peak shifts to the blue. This shift can either be due to a decrease in the refractive index of the particles due to base etching the insides of the particles, or to a slight decrease on colloid size, but not density, due to removal of silica from the particle exterior. To distinguish the cause of the blue shift, the refractive indices of the particles were measured, and the results are included in Figure 5-4. These show no detectable reduction in the refractive index, indicating that the base only reacts with the surface of the silica particles, not the bulk. Using Eq. 5-2, the 5 nm shift corresponds to a drop in the volume fraction of silica from 0.74 for an fcc lattice to 0.72 upon removal of silica from the spheres. This corresponds to etching 5 nm of silica from the surface. The spectrum for polymer modified colloidal crystals indicates that this loss is offset by addition of a 5 nm polyacrylamide layer<sup>118</sup>, which has a refractive index similar to that of silica<sup>120</sup>.

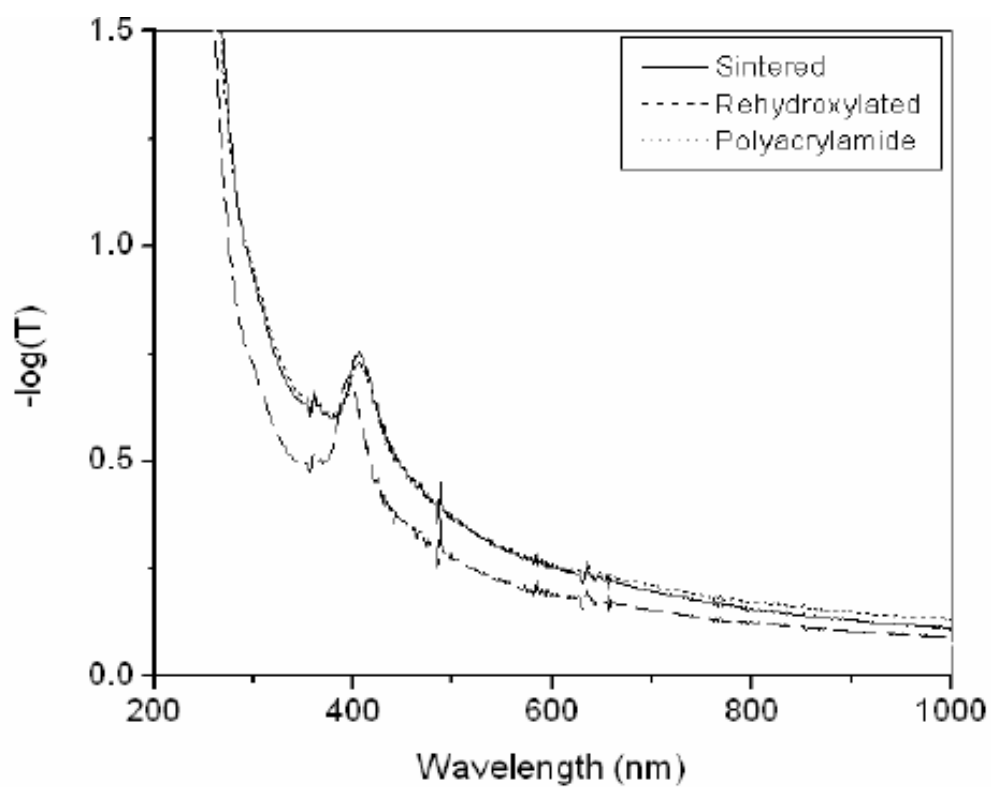


Figure 5-9. UV-visible transmission spectra for a colloidal crystal after sintering (solid line), after base treatment to rehydroxylate the surface (dashed line) and after growth of a polyacrylamide brush layer (dotted line). The small spikes, e.g., at 490 nm, are artifacts.

### Conclusions:

The silica particles in sintered silica colloidal crystals are shown to have a refractive index approaching the composition of fused silica, despite being made from calcined particles having a lower refractive index. Rehydroxylation of the surface is shown to restore the surface silanols for subsequent silylation, without etching the interiors of the particles. Overall, the chemical modification of silica particles required many steps in processing, and the Bragg peak in the final material demonstrates that crystalline order remains intact after all of these steps. This ability to chemically modify the silica extends the range of applications for silica colloidal crystals, including use as separation media and high-surface area capture materials for microarrays.

## CHAPTER 6: DETERMINING THE TOPOGRAPHICAL AND CHEMICAL PROPERTIES OF NON-POROUS SILICA COLLOIDS USING AFM AND FTIR

### Introduction:

Silica is the most widely used substrate material for liquid chromatography. Chapter 4 describes work done on three commercial silica products to determine the effect of substrate topography on peak tailing and broadening of basic analytes<sup>10</sup>. Agilent Zorbax and Waters Symmetry are gels of 3.5 or 5  $\mu\text{m}$  particles composed of  $\sim 100$  nm, non-porous colloids. Unlike the relatively smooth non-porous colloids of the Agilent Zorbax, the Waters Symmetry material has been chemically treated to create a rougher surface. The third sample in the study was a monolithic silica, Merck Chromolith. Recently, these monolithic products have become an important chromatographic stationary phase substrate. The cover story of the December 11, 2006 *Chemical and Engineering News* looked at the benefits to chromatographic separations that these monolithic silica substrates have brought. According to the article, these materials, "...are being touted by manufacturers and users for the enhanced speed and thoroughness with which they can separate complex mixtures of biological molecules."

Even though silica has been used for decades as a chromatographic substrate and the monolithic products are receiving high praise, there are still problems to be resolved and breakthroughs to be made in the manufacture of these products.

All three of the materials mentioned; Agilent Zorbax, Waters Symmetry, and Merck Chromolith showed concentration dependent tailing and broadening of a cationic dye,

1,1'-didodecyl-3,3',3'-tetramethylindocarbocyanine perchlorate (DiIC<sub>12</sub> or simply DiI) in our previous study. This tailing and broadening is caused by isolated silanols on these silica products, so despite all of the advances, an issue that has been around since the inception of liquid chromatography has not been resolved.

Surface features and topography have been investigated to determine whether they are factors leading to the presence of isolated silanols. In our study of the commercial silica products, we speculated that isolated silanols were likely hidden in seams between the ~100 nm silica colloids that combine to form the micron sized silica gel particles<sup>10</sup>. We also determined that these products have nanoscale topographical features similar to the polishing marks and pits seen on the fused silica coverslips studied in previous works. DiI was shown to be particularly absorptive to these features in previous works and could reasonably be expected to be as absorptive on these features on the corresponding features on the commercial silica products.

Another clue about the effect of topography on the presence of isolated silanols can be seen in the work of Kamiya et. al. where they used FTIR to show in part the effect of particle diameter, and therefore radius of curvature, on the IR spectrum<sup>11</sup>. Their work showed that as the particles decrease in diameter, the isolated silanol peak, which is not present at all in the spectrum of 230 nm particles, increases as the particle diameter decreases until it is very prominent in the 8 nm particle spectrum. As the particles become smaller, the curvature of the surface increases and the distance between silanol groups increases. They showed that a 0.17 Å increase in separation led to ~28% reduction in the attractive potential between adjacent silanols.

All of these works provide evidence that surface topography plays an important role in the formation of isolated silanols, which are the root cause of peak tailing and broadening of basic analytes in liquid chromatography.

This chapter describes the work done to characterize the topographical and chemical characteristics of silica colloids as they are calcined, defined as heating well below the melting temperature of silica (600°C in this case), and sintered, defined as heating to near the melting temperature of silica (900°C in this case). These effects are characterized using AFM, FTIR, and UV-Vis. Since subsequent modification of the silica surface with alkylsilanes requires hydroxyl groups on the colloid surface, AFM and FTIR data were also taken after rehydroxylating the surface.

The importance of silica colloidal crystals was discussed in Chapter 5, and a more thorough investigation of each step is necessary in order to optimize the process and final crystal. A perusal of the literature on calcination and sintering of silica will show that there are almost as many methods as authors.

The measurements in this chapter provide detailed quantitative information about silica colloids as they are processed and also provide additional information about the location of isolated silanols.

#### Sample Preparation:

Sample substrates for the AFM and FTIR experiments were silicon slides approximately 25 mm x 25 mm cut from a single 4" silicon wafer obtained from Wafer World Inc. The silicon slides were cleaned by pre-wetting them with 1 mL, 99.5% trifluoroacetic acid (TFA) obtained from EMD and then soaking overnight in

concentrated (69.6%) nitric acid obtained from Mallinkrodt. The TFA and  $\text{HNO}_3$  were used as received.

#### Silica Preparation:

The silica colloids were prepared using the method first described by Stöber et. al.<sup>17</sup> and later extended by Bogush et al<sup>18</sup>. Absolute ethanol was obtained from AAPER Alcohol and Chemical Company, tetraethoxysilane (TEOS) from Geleste, and 2 M  $\text{NH}_3$  in ethanol from Aldrich. All chemicals were used as received without further purification. The 18.2 M $\Omega$  water was obtained from a Millipore, Milli Q, Gradient A10 benchtop water purifier. Prior to use, the water and  $\text{NH}_3$  were filtered using a syringe and 0.2  $\mu\text{m}$  pore syringe filter.

A solution of 81 mL absolute ethanol, 44 mL water, and 175 mL  $\text{NH}_3$ /ethanol was made in an Erlenmeyer flask. The solution was stirred at ambient temperature throughout the reaction. A second solution of 20 mL TEOS and 30 mL absolute ethanol was added in a single pour to the stirring solution and allowed to react overnight in a covered flask.

Two stepwise additions were done to increase the size of the silica colloids. Each previous solution was stirred while 12.3 mL TEOS and 2 mL water were added, and after each addition, the solution was allowed to stir overnight. The volume ratio provided a 2:1 water/TEOS molar ratio.

The colloids recovered at the end of this process were the “As Made” particles.



Three successive calcinations (heating at 600 °C for 12 hours) were done to completely dry the colloids. The colloids recovered at the end of this process were the “C3X” particles.

A final sintering (heating at 900 °C for 12 hours) was done after the final calcination step. These colloids were the “Sintered” particles.

Rehydroxylation was accomplished by soaking the Sintered sample in 18.2 MΩ water adjusted to pH 10 overnight at a temperature of 30 °C. The pH was adjusted with 1.0 M tetrabutylammonium hydroxide in water, from Sigmal-Aldrich. The sample was then rinsed thoroughly with 18.2 MΩ water, dried in a stream of nitrogen, and then placed in an ozone plasma cleaner for 10 minutes to remove any residual organics.

For the As Made and C3X particles, separate samples were made for each AFM measurement. Samples for topographic measurements were made by suspending the particles in ethanol, depositing 200 μL of the suspension on a silicon slide, and letting the ethanol evaporate.

The evaporative deposition method did not work for adhesion force measurements, which had to be done in water to avoid capillary effects. The colloidal crystal structure for As Made and C3X particles simply fell apart when exposed to water, so a portion of these colloids was placed on double-sided tape attached to the silicon substrate. The adhesive of the tape was sufficient to anchor the particles so adhesive force measurements could be made in water.

The Sintered sample was produced by heating a crystal formed by depositing the C3X colloids on a silicon slide. For the adhesive force measurements, the sintered sample did

not require the double-sided tape since the colloidal crystal was structurally rigid and did not fall apart when exposed to water. Both topographic and adhesive measurements were done on this single sample.

For the transmission FTIR measurements, a single sample of the As Made particles was prepared using the previously described method. All of the heating steps and rehydroxylation were done on this sample, and FTIR measurements were taken on this single sample after each step in the process. Following each heating step and before taking an FTIR measurement, the sample was cleaned in an ozone plasma cleaner for 10 minutes.

To maintain consistency in measurements, a single blank silicon slide was used throughout the FTIR measurements. This blank was cut from the same wafer as the sample slide and underwent identical treatment to the sample slide.

The refractive index measurements were made in the manner described in Chapter 2. For the timed sintering study, all samples were heated from room temperature to 900°C at a rate of 10°C per minute. The length of the sintering process was the time the sample remained at 900°C. For example, 0 hours of sintering indicates that the sample immediately began to cool back to room temperature after reaching 900°C, while 2 hours of sintering indicate the sample remained at 900°C for two hours before starting to cool back to room temperature.

## Results and Discussionn:

Figure 6-1 shows each of the samples on scan sizes stretching over three orders of magnitude. The 10  $\mu\text{m}$  scans clearly show the ordering these particles undergo as the

ethanol evaporates. This packing is not perfect however, and large cracks, changing packing patterns, and missing particles within the crystal lattice are all in evidence at this scale. The 1  $\mu\text{m}$  scans show that there is no large-scale structure on the surface of the individual particles at any stage in the process. The only clear evidence of surface structure is a number of basins on the As Made sample at the 100 nm scale. These basins are 1 – 2 nm in depth and resemble features previously discussed in Chapter 4. The smooth structure of the surfaces resembles the non-porous, 100 nm colloids used by Agilent in the production of their Zorbax RX product.

Gwyddion was used on a well-ordered portion of each sample to determine particle diameter using the method described in Chapter 2. Within the 95<sup>th</sup> percent confidence interval, the particles are  $538 \pm 9$  nm,  $500 \pm 5$  nm, and  $501 \pm 9$  nm for the As Made, C3X, and Sintered samples, respectively. A summary of statistics for the various samples is shown in Table 6-1. These results are a 2-4 percent relative standard deviation, demonstrating the usefulness of the Stöber Method in producing monodisperse silica colloids.

Calcinating the As Made particles three times resulted in a 38 nm loss in diameter which corresponds to a volume reduction of 14%. This volume reduction is the result of water being expelled from the interior of the siloxane matrix, which forms the bulk of the particle. The C3X and Sintered colloids are statistically identical in size, indicating that three calcination iterations are sufficient to completely remove all water trapped within the silica lattice during the initial growth process. This result was different than for the calcined samples discussed in Chapter 5. In that case, there was a measurable decrease in

diameter going from calcined to sintered. However, the calcination method was different in the two studies, and, unlike the method used in this study, the calcination method described in Chapter 5 was simply not sufficient to remove all of the water from the siloxane matrix.

While sintering did not result in any further reduction in size, it did have considerable affect on the presence and location of isolated silanols as will be discussed later.

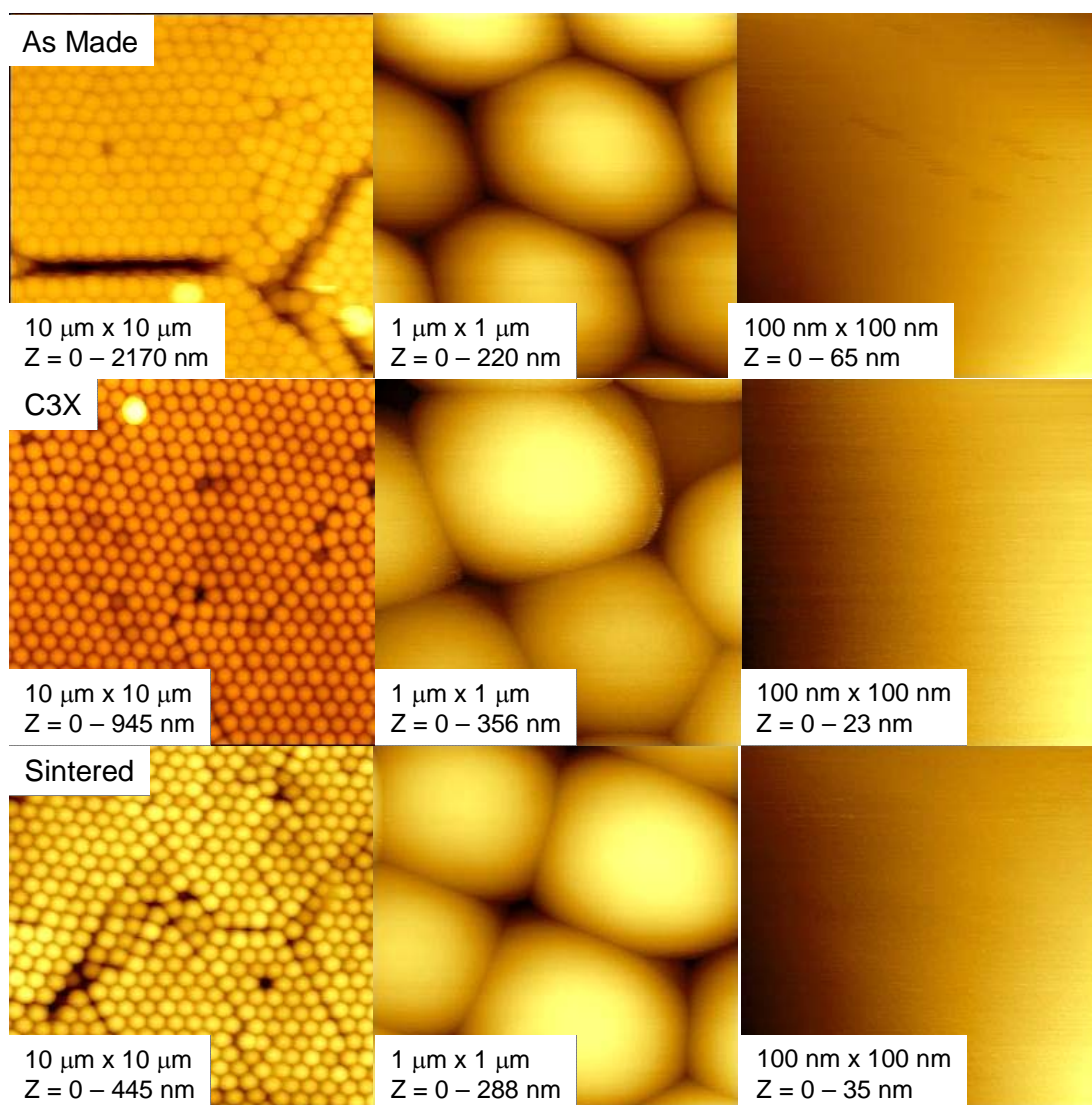


**Figure 6-1. AFM images of each of the three samples on scales ranging over three orders of magnitude: As Made, C3X, and Sintered. The scan size and z-scales are indicated in each panel.**

Silica Sample	AFM		FTIR of Isolated Silanols	
	Diameter (nm)	Adhesion Force (pN)	Frequency (cm <sup>-1</sup> )	Ratio
As Made	538 ± 9	1600 ± 300	3742	2.52 x 10 <sup>-3</sup>
C3X	500 ± 5	700 ± 130	3747	2.27
Sintered	501 ± 9	0 ± 10 <sup>a</sup>	3748	9.58
Rehydroxylated	-	600 ± 63	3743	3.62 x 10 <sup>-1</sup>

**Table 6-1. Summary of statistics for As Made, C3X, and Sintered particles. The AFM data include particle diameter and force of adhesion. This data is at the 95th percent confidence interval. The FTIR data shows frequency and abundance of isolated silanols relative to the associated silanol peak maximum near 3660 cm<sup>-1</sup>.**

Because of uncertainty in the cantilever spring constant, adhesion force values should be considered relative rather than absolute.

**a No detectable adhesion force within the electrical noise of the measurement**

Figure 6-2 shows the associated and isolated silanol region of the FTIR spectra for the silica at each step in the processing. Summary values for the isolated silanol peak frequency and abundance relative to the associated silanol peak maximum are given in Table 6-1. The isolated silanol peak blue shifts to higher frequencies as the As Made particles are calcined and then sintered, and there is a slight red shift following rehydroxylation. The blue-shifting of the isolated silanol can be interpreted as the siloxane matrix becoming progressively stiffer and stiffer as the sample is first calcined and then sintered. The ratio of isolated silanols to associated silanols increases as the As Made particles are calcined and then sintered, and then decreases after rehydroxylation. The frequency shift of the peak and relative sizes of the isolated and associated silanol peaks can be seen in more detail in Figure 6-3, which shows the isolated and associated silanol region from Figure 6-2 on an expanded scale. The As Made particles have virtually no isolated silanol peak, and the prominent isolated silanol peak that is present during the calcination and sintering steps disappears again after rehydroxylation; in both of these cases the very small signal from the isolated silanols indicates that they have been transformed into associated silanols.

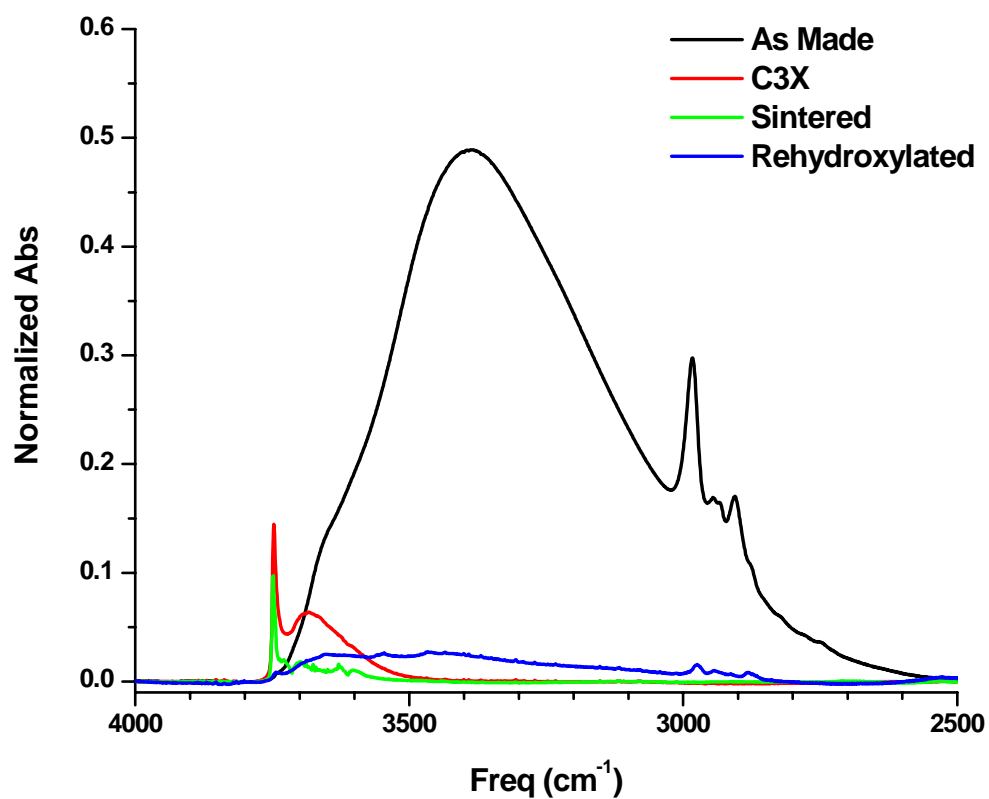


Figure 6-2. FTIR spectra of As Made, C3X, Sintered, and Rehydroxylated silica sample showing a broad water peak at approximately 3400 cm<sup>-1</sup>, a broad associated silanol peak at approximately 3600 cm<sup>-1</sup>, and much narrower isolated silanol peak at approximately 3745 cm<sup>-1</sup>.



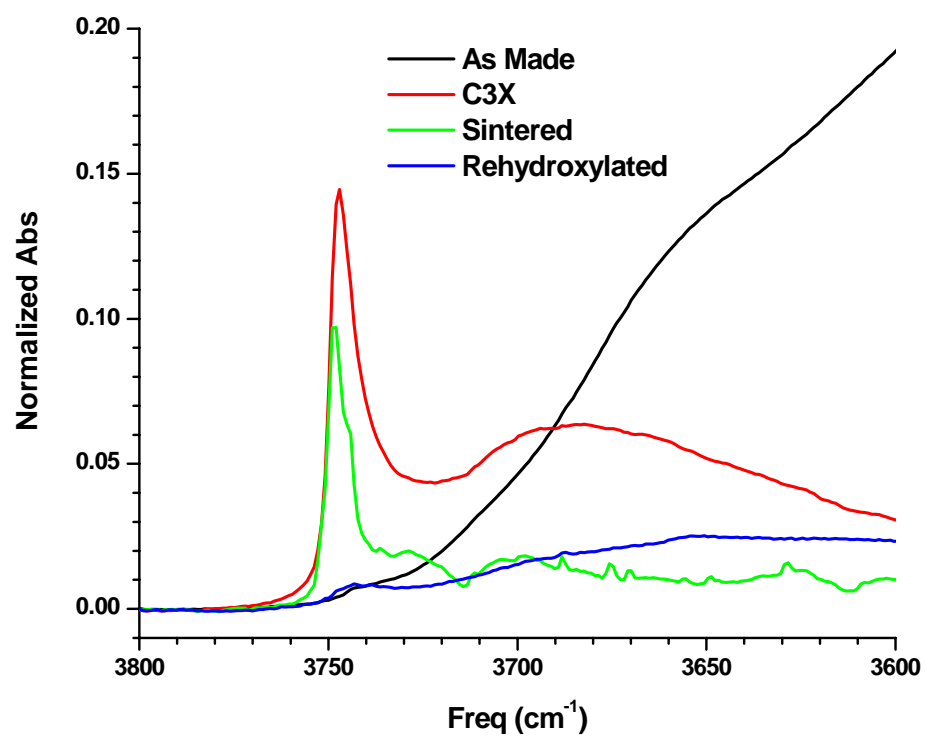


Figure 6-3. Expanded scale of figure 6-2 showing isolated and associates silanol peaks for As Made, C3X, Sintered, and Rehydroxylated sample.

The adhesive force measurements, shown in Table 6-1, show a definite trend. The force decreases as the As Made particles are first calcined and then sintered. The As Made sample has an adhesion force on the same order as the Agilent Zorbax RX particles, which is not surprising considering the very similar topography of the non-porous regions of each type of silica. The adhesive force is reduced by roughly  $\frac{1}{2}$  by the three calcination iterations. Following the sintering step at 900 °C, the adhesive force is reduced to zero, within the measurement sensitivity of the instrument ( $\sim \pm 10$  pn). For the Sintered sample, several measurements were taken at widely separated locations on different particles, and no detectable adhesive force was ever measured. This indicates that there are no silanols remaining on a portion of the colloid surface that is accessible to the AFM tip. After rehydroxylation at 30°C for 24 hours, the adhesive force had recovered to nearly the C3X value.

The adhesive force measurement is the attraction between surface silanols and –OH groups on the AFM cantilever tip, so, if the isolated silanols were being probed by the adhesive force measurements, increasing isolated silanols should be expected to result in increasing adhesive force. However, the adhesive force actually decreased as the silica was calcined and then sintered, in direct opposition to the increasing abundance of isolated silanols as measured by FTIR. The sintered sample, which has the greatest abundance of isolated silanols, actually has no detectable adhesive force.

This is further evidence that the isolated silanols are not isotropically distributed over the surface of the silica colloids. For the sintered silica, FTIR shows that there are no associated silanols remaining on the silica, so the isolated silanols are the only species

available for adhesive force interaction with the AFM probe. The AFM data show that no adhesive force interactions occur. The adhesive force for an isolated silanol is expected to be much stronger than for an associated silanol, so it can be inferred that the AFM probe is simply not encountering any isolated silanols as it probes the sintered surface.

This can be explained with the speculation from our 2006 *Analytical Chemistry* paper<sup>10</sup> and the results of Kamiya et. al.<sup>11</sup> The isolated silanols are located in seams formed when the colloids are fused together upon sintering. These seams have regions with high local curvature that lead to the formation of isolated silanols. Even after sintering, the bulk of the colloid surface does not have the high local curvature shown by Kamiya and coworkers to be necessary for the formation of isolated silanols. In addition to the very large radius of curvature for these particles, the AFM data of the particle surfaces do not show any evidence of nanoscale topographical features as were seen on the commercial silica products studied previously<sup>10</sup>.

Williams, Han, and Beebe showed in their 1996 Langmuir paper<sup>121</sup> that adhesive force measurements were not simply the result of a single interaction between the surface and AFM probe but that several points of interaction were involved with a single measurement. Additionally, the number of these interactions followed a Poisson distribution, and the single bond strength and number of bonds could be determined by taking a sufficient number of measurements. The single bond strength is simply the ratio of the measurement variance to the mean;  $F_{adh} = \frac{\sigma^2}{\mu_{adh}}$ , and the average number of

bonds is the mean of the adhesive force measurements divided by the single bond

adhesive force;  $N_{adh} = \frac{\mu_{adh}}{F_{adh}}$ .

Using these results and the data from Table 1 for the As Made, C3X, and Rehydroxalated samples, the single bond adhesive force and average number of bonds is 165.7 pN and 9.7, 134.4 pN and 5.1, and 94.0 pN and 6.4, respectively.

To obtain enough data for a valid statistical analysis, two new samples were made and larger data sets were collected. Two crystals of the C3X particles were made, and one was sintered for 3 hours and another sintered for six hours. They were then rehydroxylated under identical conditions and adhesive force measurements were taken. Eighty measurements were taken for the sample sintered for 3 hours, and 294 measurements were taken for the sample sintered for 6 hours. Rather than making measurements on several different particles as was done for the As Made, C3X, Sintered, and Rehydroxylated samples; measurements were done at a single point on one particle. Figure 6-4 shows the histograms of the raw adhesive force and the average number of bonds for the two samples, and the Poisson distribution is evident in both data sets.

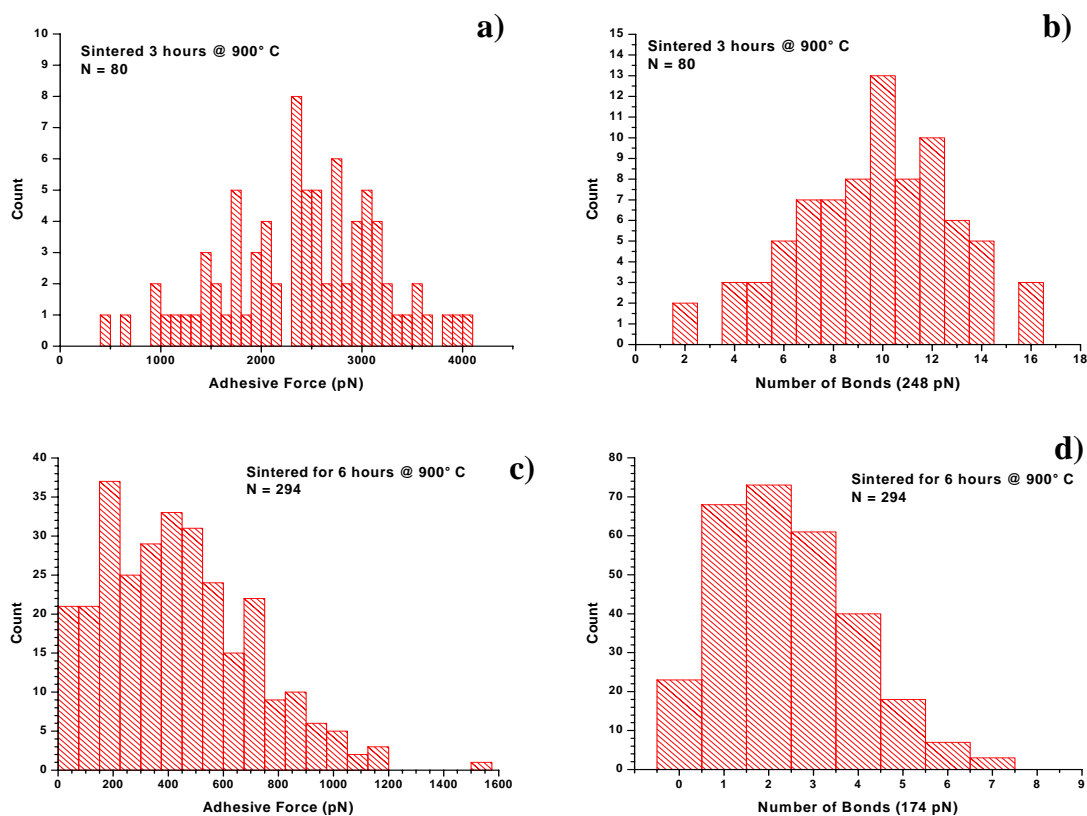


**Figure 6-4.** Adhesive force measurement data for rehydroxylated silica colloids that had been sintered for 3 hours and 6 hours. Images a) and c) show the histograms for the raw measurement data for the 3 hour and 6 hours sintering respectively. Images b) and d) show histograms for the number of bonds formed between the AFM probe and the silica surface. The average number of bonds assumes a single bond adhesive strength of 248 pN for the 3 hour sintering sample and 174 pN for the sample sintered for 6 hours.

Because of uncertainty in the cantilever spring constant, the adhesive force should be considered a relative and not absolute value.

The single bond strength was calculated using the nominal cantilever spring constant provided by the manufacturer, but the actual value of the spring constant can vary by a factor of 8, so this value can be used for comparison but should not be taken as an absolute. Also, numerous repetitive force measurements could result in the spring constant changing over the course of the measurements. To obtain accurate adhesive force measurements in this manner, the spring constant must be determined and monitored for change throughout the measurements. Despite these limitations, these measurements provide information of the relative strength of the adhesive force as the particles undergo processing.

After rehydroxylation, the isolated silanol signal is reduced to nearly zero because the surface silanols have become fully associated. This is demonstrated by the reappearance of the adhesive force and the red shifting of the isolated silanol peak. Further reaction of the rehydroxylated surface with an alkyl silane results in the reappearance of the isolated silanol peak as the associated silanols become modified. Sterically inaccessible regions, such as the seams between colloids could result in silanols not being modified because the alkyl silane can't reach them. Regions where the alkyl silane reaction is incomplete or the local curvature reduces the interaction between neighboring silanols lead to the reformation of isolated silanols.

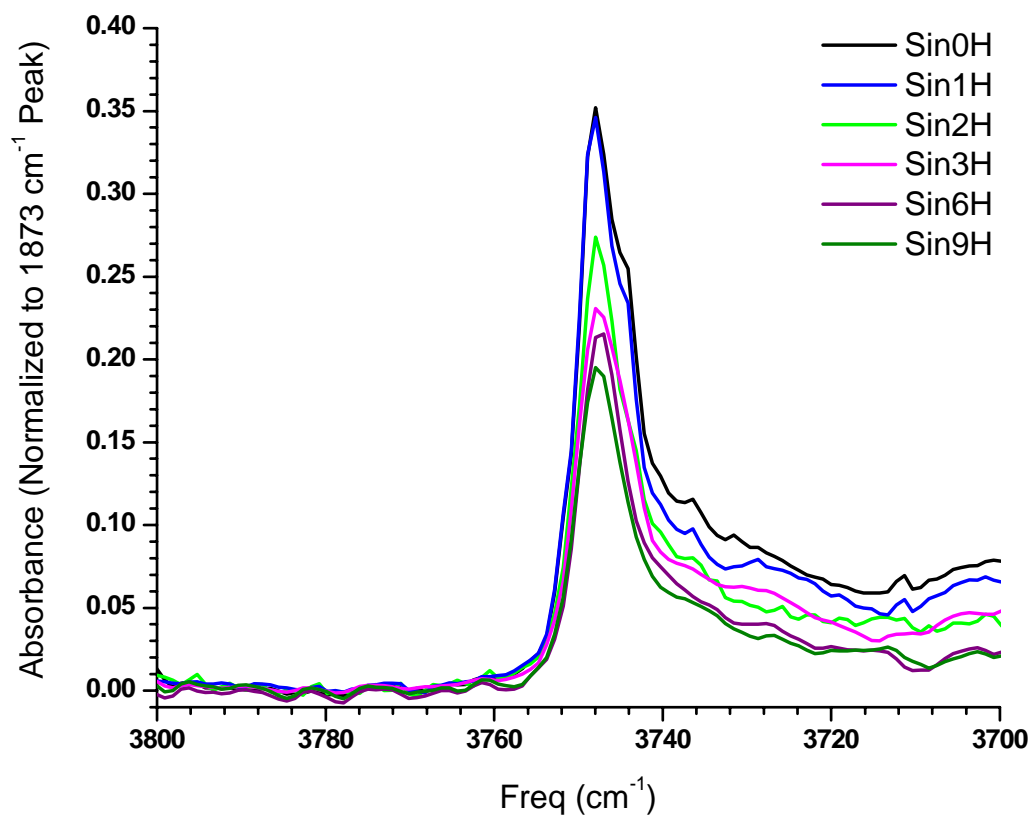


Figure 6-5. Isolated silanol spectra for samples with sintering times ranging from 0 – 9 hours. All samples were ramped from room temperature to 900 °C at 10 °C/min and held at that temperature for the time indicated before cooling to room temperature. Increased sintering time leads to a smaller isolated silanol peak.

Another question to be answered was how much time was necessary for the colloids to become fully sintered, meaning their refractive index approached that of fused silica. Measurements were made on samples that had been sintered for times ranging from 0 to 6 hours. The time that the silica colloids remained at 900°C had an effect on how well ordered the siloxane matrix became. Figure 6-5 shows the affect of sintering time on the isolated silanol peak. This reduction in the size of the isolated silanol peak can be explained by considering the disorder in the siloxane matrix that remains after the removal of trapped water. Longer sintering time provides more time for the disordered matrix to rearrange and reduces the number of sites where silanols are not converted to siloxanes.

Further evidence for time is a necessary consideration in sintering can be seen in Figure 6-6. It shows the %Transmission at 589 nm versus sintering time of the samples. The method used to make these measurements was described in Chapter 2. All of the measurements were done in a solvent mixture adjusted so that the refractive index matched that of the fully sintered samples reported in Chapter 5 ( $n = 1.454$ ). This provides a quantitative measure of how close the sample is to being fully sintered. The Sin0H sample already has a %Transmission value of 93%, and the %Transmission value of the Sin2H sample is already above 99% indicating that it is nearly as well ordered as a sample that was sintered overnight.

The work in Chapter 5 on the properties of silica colloidal crystals reported on the refractive indices of the silica colloids. The colloids that were calcinated in the manner described in that chapter have an index of refraction of 1.440, which is somewhat lower



than for fused silica, and this indicates that voids are left behind when the water is driven off by calcination. Based on the diameter change after sintering, those calcined colloids also contained a small volume of water trapped within the colloid as well. The sintering step leads to all of the water being expelled, to siloxane bonds being formed in these voids, and to colloids with an index of refraction of 1.454. This is very close to the index of refraction for fused silica, 1.458.

Measurements done in this study indicate that the refractive index of silica colloids sintered for six hours at 900°C have a refractive index of 1.452, indicating that six hours is sufficient to completely sinter the sample.

As sintering transforms silanols into siloxanes, there are fewer and fewer silanols, and eventually, all that remain are the isolated silanols. As the sintering time is increased, the siloxane matrix can rearrange and previously isolated silanols are able to form siloxane bonds. This process can continue until the siloxane matrix has reached its maximum density, but even at this point isolated silanols are present.

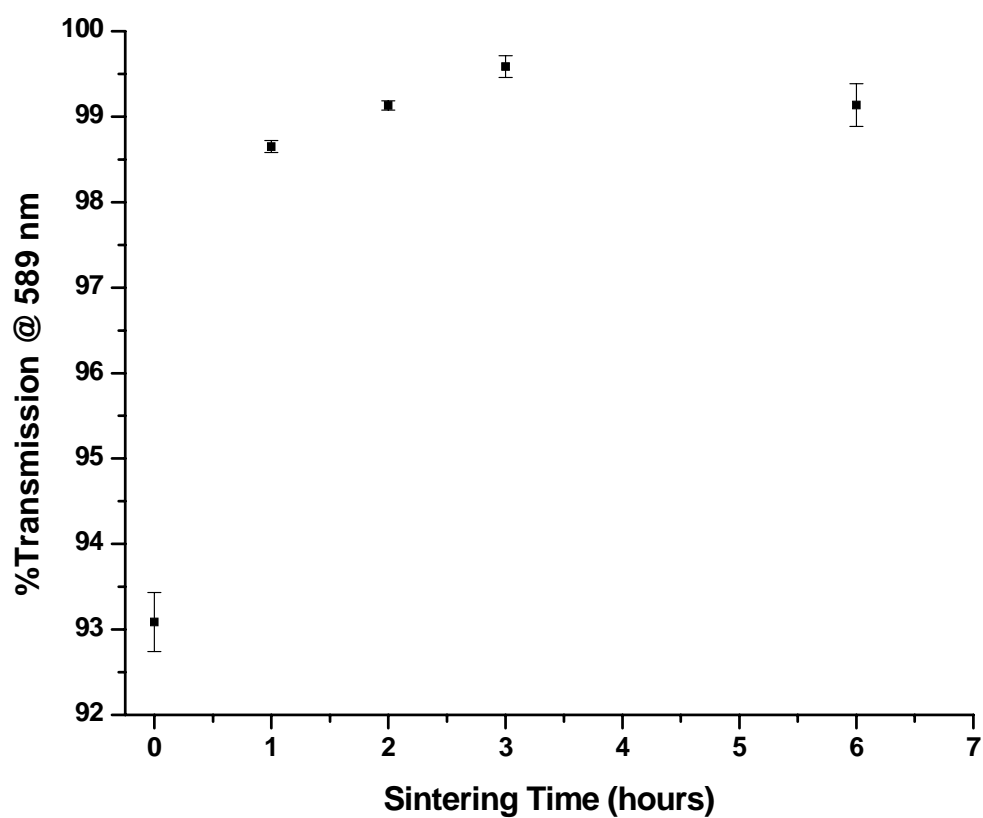


**Figure 6-6.** Graph showing the %Transmission at 589 nm versus hours of sintering for silica colloids in a solvent with a refractive index of 1.454. This is the refractive index of fully sintered silica colloids as reported in Chapter 5. As the refractive index of the colloids approaches that of the solvent, the %Transmission approaches 100.

## Conclusion

Topographical and surface chemistry of non-porous silica colloids was followed from initial production through calcination, sintering, and rehydroxylation steps.

These experimental results provide quantitative information about the change in volume, surface adhesive force, and isolated silanol abundance as the colloids are processed by a number of heating and rehydroxylation steps. Adhesive force measurements were shown to probe the associated silanols, and multiple bonds between the AFM probe and surface were demonstrated. AFM and FTIR data show that three successive, overnight calcination steps done at 600°C were sufficient to completely remove any trapped water from the siloxane matrix. FTIR and UV-Vis data indicate that after sintering the colloids for three hours at 900°C, their refractive index approaches that of colloids sintered overnight, and after six hours the colloids are almost fully sintered.

## CHAPTER 7: HIGH-SPEED ELECTROSEPARATIONS INSIDE SILICA COLLOIDAL CRYSTALS

### Introduction:

Colloidal crystals have attracted intense interest as photonic materials<sup>18, 93</sup>, chemical sensors<sup>122</sup>, perm-selective modifiers for electrodes<sup>101</sup>, and porous supports for lipid bilayers<sup>96</sup>. Here we report their use as a medium for chemical separations. They exhibit fast mass transport. They have the ability to withstand high electric fields, and their surfaces can be chemically modified in the same way as silica gel.

There is a demand for much higher speed and miniaturization in separations. Capillary electrophoresis can be performed on very fast<sup>123, 124</sup> time scales, but the separations lack high selectivity. Reversed-phase HPLC is more selective, but it is slower than electrophoresis because the flow rate, to maintain equilibrium, cannot exceed the rate of analyte diffusion between mobile and stationary phases. Faster HPLC is achieved using smaller ( $< 2 \mu\text{m}$ ), nonporous particles<sup>125</sup>, but this requires ultrahigh pressure and long column lengths due to the low surface areas. Monoliths of either silica<sup>126, 127</sup> or polymer<sup>128</sup> offer smaller diffusion distances to increase separation speed without sacrificing surface area or requiring high pressures.

In this work, crystals of nonporous, 200 nm colloids are studied as media that offer both high surface area and much smaller dimensions for analyte diffusion in the mobile phase. Their performance is compared with a commercial silica monolith. We demonstrate the separation of three cationic, hydrophobic dyes in 6 s, over a separation

length of 1 mm, using a C18 stationary phase, with an electric field strength of 1000 V/cm. We also demonstrate the separation of three peptides in 10 s over a 6 mm separation length. The results reveal marked improvement in peak width over chromatographic monoliths.

A 20  $\mu\text{m}$  thick crystal was made of 200 nm diameter silica colloids by vertical deposition onto a fused silica slide<sup>18</sup>. Colloids were calcined at 600 °C before deposition<sup>110</sup>. The crystal was hardened by sintering at 900 °C and then rehydroxylated to regenerate the surface silanol groups<sup>63</sup>. The material was silylated with  $\text{ClSi}(\text{CH}_3)_2(\text{CH}_2)_{17}\text{CH}_3$ , then endcapped with  $\text{ClSi}(\text{CH}_3)_3$ . The resulting medium should therefore have negligible electro-osmotic flow. A 1.5 cm - 2 mm strip of this material was assembled into a device depicted in Figure 7-1, which was used for separations.

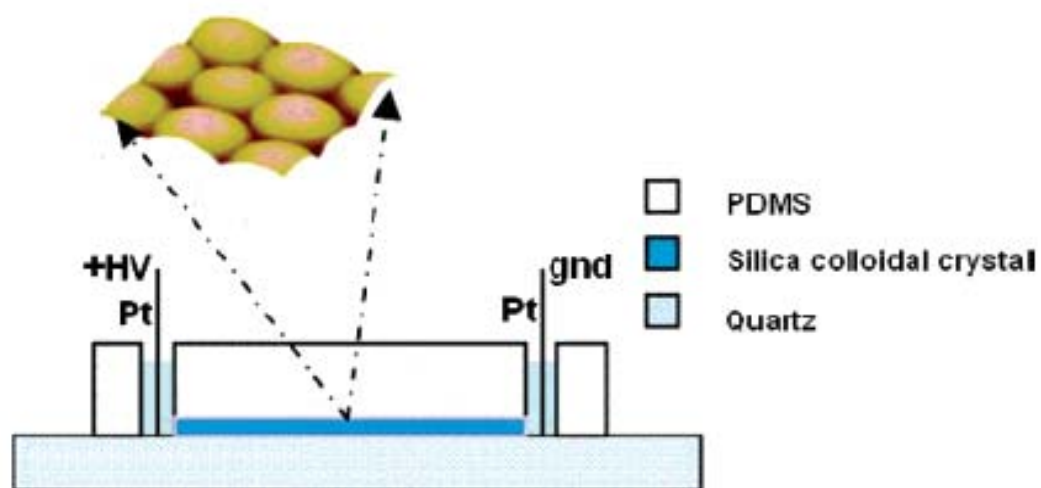


**Figure 7-1. Schematic.** The silica colloidal crystal was covered tightly with a 5 mm thick PDMS sheet. Appropriately spaced reservoirs for solvent and analyte addition were cut from the PDMS sheet. The insert is an AFM image of the 200 nm silica spheres. An inverted fluorescence microscope monitored the migration of the dyes.

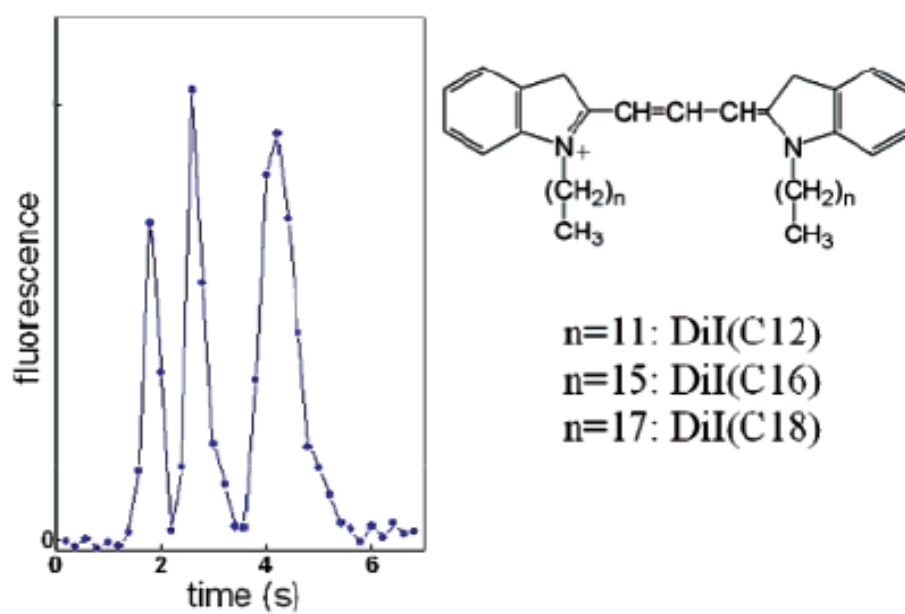


Figure 7-2. Separation of three DiIs through 1 mm of colloidal crystal using 90:10 (v/v) MeOH:water, 0.1% TFA, and a field strength of 1000 V/cm.

## Results and Discussion:

Three structurally similar dyes, DiIC12, DiIC16, and DiIC18, were used as analytes. These have the same singly charged headgroup, but differ in the lengths of their dual hydrocarbon chains. Electrokinetic injection was used: the dye mixture was put into the reservoir, 50 V/cm was applied for 5 s, then the voltage was turned off and the sample replaced with mobile phase. This differs from electrochromatography<sup>129</sup> in that there is no actual flow of the “mobile” phase. Figure 7-2a shows the separation of the three DiI species. Peaks for the three components are baseline-resolved in the 1 mm separation length in 6 s, using a field strength of 1000 V/cm. A priori, the separation could occur either by electrophoresis or by differential adsorption.

Since there is no flow of the mobile phase, the separation must be electrically driven. Therefore, the velocity of the analyte is determined by its electrophoretic velocity,  $v_e = \mu_e \cdot E$ , and the fraction of time,  $f$ , that the analyte:

$$v = \mu_e \cdot E \cdot f$$

spends in the mobile phase over the course of the separation. The fraction of time spent in the mobile phase depends on the capacity factor,  $k'$ , which is the ratio of moles of analyte in the stationary phase to moles of analyte in the mobile phase. Since a time-average and an ensemble average are equivalent,  $k'$  is also the ratio of time spent in the stationary and mobile phases.

$$k' = \frac{\text{time}_{\text{stat}}}{\text{time}_{\text{mob}}}$$



Combining these two equations, shows that the fraction of time spent in the mobile phase is  $1/(1+k')$ .

$$\frac{1}{1+k'} = \frac{time_{mob}}{time_{mob} + time_{stat}} = f$$

By substitution, the migration velocity,  $v_m$ , of the analyte has contributions from both electrophoretic mobility,  $\mu_e$ , and capacity factor,  $k'$  as shown in Equation 6-1.

$$v_m = \mu_e E / (1 + k') \quad (6-1)$$

The electrophoretic mobility of the three DiI species, measured in this mobile phase by capillary electrophoresis, are  $4.7 \times 10^{-6} \text{ cm}^2/(\text{V}\cdot\text{s})$  for DiIC12 and  $4.4 \times 10^{-6} \text{ cm}^2/(\text{V}\cdot\text{s})$  for DiIC16 and DiIC18. The small differences in electrophoretic mobility are not enough to account for the large differences in migration time, therefore, we conclude that the separation is mainly achieved through reversed phase adsorption.

An important figure of merit in evaluating a new medium for separations is the peak variance,  $\sigma^2$ , normalized for column length,  $L$ , which is referred to as the plate height,  $H$ . Smaller  $H$  indicates a better medium. Equation 6-2 gives a simple relation between plate height and separation velocity,  $v$ , which is the van Deemter

$$H = A + C \cdot v \quad (6-2)$$

equation for moderate to high velocities. The  $A$  term is a measure of the uniformity of the medium. A heterogeneously packed medium would have a distribution of path lengths leading to increased peak variance and so a larger plate height. Because it is so well ordered, the colloidal crystal is expected to have a very narrow distribution of path lengths. The  $C$  term is a measure of how slow the mass transport is through the medium,

including diffusion through the mobile phase to reach the stationary phase. The colloidal crystal is expected to have much faster mass transport because the particles are 10-fold smaller than those typically used in HPLC.

A van Deemter plot for DiIC12 in the colloidal crystal is shown in Figure 7-3. For comparison, the van Deemter plot is shown for a commercial monolithic column, Merck Chromolith, which has a 2.5 cm length and the same chemically modified surface. Since there is no solvent flow with the colloidal crystal, velocity for the van Deemter plot was determined by measuring the velocity of an unretained dye, Rhodamine 6G. This dye marker elutes with the system peak in HPLC, and in the separation of Figure 7-2, this dye would elute at 0.9 s.

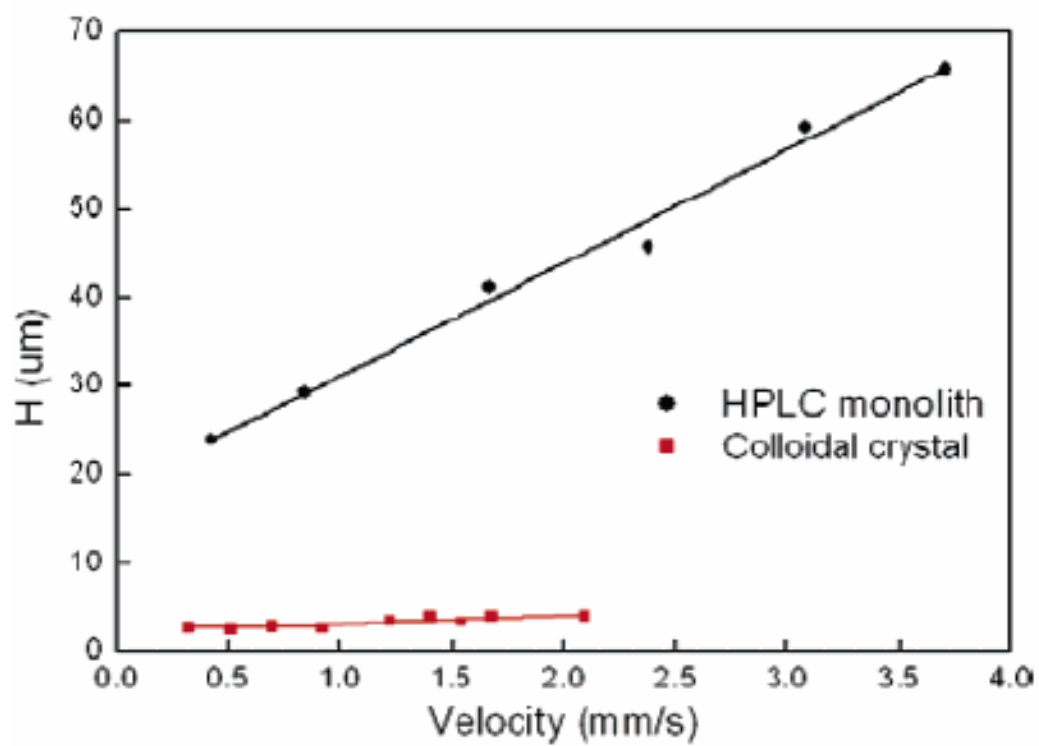


Figure 7-3. van Deemter plots for Merck Chromolith (●) and the colloidal crystal (■). The same mobile phase was used as for Figure 7-2.

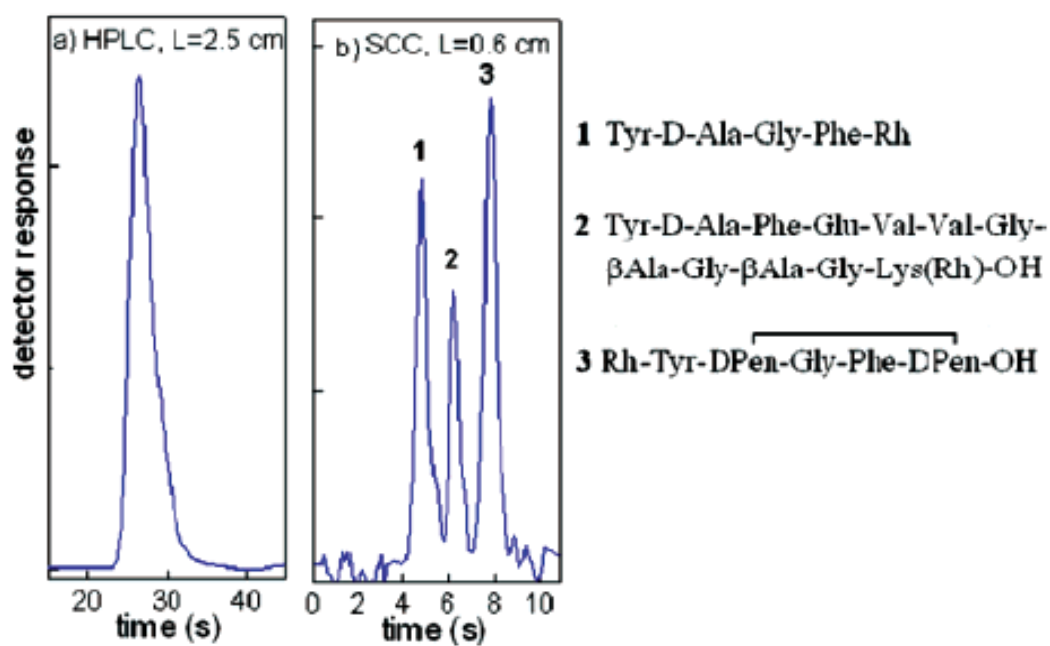


Figure 7-4. Separation by (a) HPLC and (b) the silica colloidal crystal of three peptides whose structures are shown to the right. The same mobile phase as in Figure 7-2 was used for both separations.

The van Deemter plots for the two materials differ markedly, with the colloidal crystal exhibiting much smaller, more favorable plate heights at all velocities. The  $A$  term for the colloidal crystal is  $2.4\ \mu\text{m}$ , while  $A$  is  $19\ \mu\text{m}$  for the Merck Chromolith. The injected width contributes negligibly in both cases<sup>110</sup>. The  $C$  term is also remarkably smaller for the colloidal crystal:  $1.2\ \text{ms}$  for the colloidal crystal versus  $12.8\ \text{ms}$  for the Merck Chromolith. The size of the  $C$  term limits the speed of separations, and the much lower  $C$  term for the colloidal crystal is thus significant for the potential use of colloidal crystals in fast separations. The colloidal crystal thus achieves the expected large decreases in both  $A$  and  $C$  to give much lower peak variance than the high quality HPLC monolith.

As mentioned earlier, both adsorption and electrophoresis contribute to migration rate, as was shown by Eq 7-1. This dual selectivity could be advantageous for peptide separations, where small, hydrophilic peptides coelute in HPLC. Figure 7-4 shows a separation of a mixture of three peptides, each labeled with Rhodamine dye, in 90:10 (v/v) MeOH:H<sub>2</sub>O and 0.1% trifluoroacetic acid (TFA). The peptide sequences are shown in Figure 7-4, written left-to-right from the N- to C-terminus and indicating the end bearing the rhodamine label (Rh). Peptides 1 and 2 each have a +2 charge, while peptide 3 has a +1 charge. The three peptides are shown to coelute in HPLC at  $1\ \text{mL/min}$  (Figure 7-4a). The tail in the chromatogram of Figure 7-4a is from peptide 3 eluting slightly later than peptides 1 and 2. However, the three peptides are well resolved by the colloidal crystal in less than  $10\ \text{s}$  at  $800\ \text{V/cm}$  (Figure 7-4b). The elution times track the electrophoretic mobilities<sup>127</sup>. A separation length of  $6\ \text{mm}$  was used for the colloidal

crystal. The low peak variance per length is consistent with the van Deemter plot of Figure 7-3.

#### Conclusions:

This work reports the first use of colloidal crystals for chemical separations. The results reveal that electrically driven transport achieves highly efficient separation of charged analytes. A separation based on differences in adsorptivity is demonstrated in Figure 7-1, and a separation based on differences in electrophoretic mobility is demonstrated in Figure 7-4. The results show greatly reduced peak width and greatly increased speed of mass transport compared to the commercial monolithic stationary phase. The short distance of 1 mm for a reversed-phase separation is unprecedented.

While they are preliminary, these results demonstrate that a better understanding of the flow mechanics, stationary phase structure and chemical properties, and colloidal crystal processing can lead to significant improvements in chromatographic separations.

## REFERENCES

1. Karger, B. L.; Snyder, L. R.; Horvath, C., *An Introduction to Separation Science*. Wiley-Interscience: New York, 1973.
2. Bailey, F.; Brittain, P. N., High-efficiency liquid chromatography in pharmaceutical analysis. *Journal of Chromatography* **1973**, 83, 431-7.
3. Stella, C.; Rudaz, S.; Mottaz, M.; Carrupt, P.-A.; Veuthey, J.-L., Analysis of basic compounds at high pH values by reversed-phase liquid chromatography. *Journal of Separation Science* **2004**, 27, (4), 284-292.
4. Cox, G. B., The influence of silica structure on reversed-phase retention. *Journal of Chromatography A* **1993**, 656, (1-2), 353-67.
5. Nawrocki, J., The silanol group and its role in liquid chromatography. *Journal of Chromatography A* **1997**, 779, (1 + 2), 29-71.
6. Fornstedt, T.; Zhong, G.; Guiochon, G., Peak tailing and mass transfer kinetics in linear chromatography. *Journal of Chromatography, A* **1996**, 741, (1), 1-12.
7. Fornstedt, T.; Zhong, G.; Guiochon, G., Peak tailing and slow mass transfer kinetics in nonlinear chromatography. *Journal of Chromatography, A* **1996**, 742, (1+2), 55-68.
8. Gotmar, G.; Fornstedt, T.; Guiochon, G., Peak tailing and mass transfer kinetics in linear chromatography. Dependence on the column length and the linear velocity of the mobile phase. *Journal of Chromatography, A* **1999**, 831, (1), 17-35.
9. Wirth, M. J.; Ludes, M. D.; Swinton, D. J., Spectroscopic Observation of Adsorption to Active Silanols. *Analytical Chemistry* **1999**, 71, (18), 3911-3917.
10. Legg, M. A.; Wirth, M. J., Probing topography and tailing for commercial stationary phases using AFM, FT-IR, and HPLC. *Analytical Chemistry* **2006**, 78, (18), 6457-6464.
11. Kamiya, H.; Mitsui, M.; Takano, H.; Miyazawa, S., Influence of particle diameter on surface silanol structure, hydration forces, and aggregation behavior of alkoxide-derived silica particles. *Journal Of The American Ceramic Society* **2000**, 83, (2), 287-293.
12. Ettre, L. S.; Zlatkis, A., *75 Years of Chromatography: A Historical Dialogue*. Elsevier Scientific Publishing Company: Amsterdam, 1979; Vol. 17.

13. Scott, R. P. W., *Techniques and Practice of Chromatography*. Marcel Dekker, Inc.: New York, 1995; Vol. 70.
14. Giddings, J. C., *Unified Separation Science*. Wiley: New York, 1991.
15. Iler, R. K., *The Chemistry of Silica: Solubility, Polymerization, Colloid and Surface Properties and Biochemistry*. 1979; 866 pp.
16. Wikipedia Silicon dioxide. <http://en.wikipedia.org/wiki/Silica> (19 December 2006),
17. Stöber, W.; Fink, A.; Bohn, E., Controlled Growth Of Monodisperse Silica Spheres In Micron Size Range. *Journal Of Colloid And Interface Science* **1968**, 26, (1), 62-69.
18. Bogush, G. H.; Tracy, M. A.; Zukoski, C. F., Preparation of Monodisperse Silica Particles - Control of Size and Mass Fraction. *Journal of Non-Crystalline Solids* **1988**, 104, (1), 95-106.
19. Nozawa, K.; Gailhanou, H.; Raison, L.; Panizza, P.; Ushiki, H.; Sellier, E.; Delville, J. P.; Delville, M. H., Smart control of monodisperse Stober silica particles: effect of reactant addition rate on growth process. *Langmuir* **2005**, 21, (4), 1516-23.
20. Golshan-Shirazi, S.; Guiochon, G., The equilibrium-dispersive model of chromatography. *NATO ASI Series, Series C: Mathematical and Physical Sciences* **1992**, 383, (Theoretical Advancement in Chromatography and Related Separation Techniques), 35-59.
21. Golshan-Shirazi, S.; Guiochon, G., The ideal model of chromatography. *NATO ASI Series, Series C: Mathematical and Physical Sciences* **1992**, 383, (Theoretical Advancement in Chromatography and Related Separation Techniques), 1-33.
22. Golshan-Shirazi, S.; Guiochon, G., Review of the various models of linear chromatography, and of their solutions. *NATO ASI Series, Series C: Mathematical and Physical Sciences* **1992**, 383, (Theoretical Advancement in Chromatography and Related Separation Techniques), 61-92.
23. Guiochon, G.; Lin, B. C., *Modeling for Preparative Chromatography*. Academic Press: San Diego, 2003; 342 pp.
24. Wirth, M. J.; Smith, E. A.; Anthony, S. R., Measurement and simulation of tailing zones of a cationic dye in analytical-scale reversed phase chromatography. *Journal of Chromatography, A* **2004**, 1034, (1-2), 69-75.



25. Nussbaumer, R. J.; Halter, M.; Tervoort, T.; Caseri, W. R.; Smith, P., A simple method for the determination of refractive indices of (rough) transparent solids. *Journal of Materials Science* **2005**, 40, (3), 575-582.
26. Nečas, D.; Klapetek, P. *Gwyddion*, Czech Metrology Institute: 2004 - 2005.
27. Rasband, W. S. *ImageJ*, U. S. National Institutes of Health, Bethesda, Maryland, USA: 1997 - 2005.
28. Ambrose, W. P.; Basche, T.; Moerner, W. E., Detection And Spectroscopy Of Single Pentacene Molecules In A Para-Terphenyl Crystal By Means Of Fluorescence Excitation. *Journal of Chemical Physics* **1991**, 95, (10), 7150-7163.
29. Jett, J. H.; Keller, R. A.; Martin, J. C.; Marrone, B. L.; Moyzis, R. K.; Ratliff, R. L.; Seitzinger, N. K.; Shera, E. B.; Stewart, C. C., High-Speed Dna Sequencing - An Approach Based Upon Fluorescence Detection of Single Molecules. *Journal of Biomolecular Structure & Dynamics* **1989**, 7, (2), 301-309.
30. Peck, K.; Stryer, L.; Glazer, A. N.; Mathies, R. A., Single-Molecule Fluorescence Detection - Auto-Correlation Criterion And Experimental Realization With Phycoerythrin. *Proceedings of the National Academy of Sciences of the United States of America* **1989**, 86, (11), 4087-4091.
31. Shera, E. B.; Seitzinger, N. K.; Davis, L. M.; Keller, R. A.; Soper, S. A., Detection of Single Fluorescent Molecules. *Chemical Physics Letters* **1990**, 174, (6), 553-557.
32. Whitten, W. B.; Ramsey, J. M.; Arnold, S.; Bronk, B. V., Single-Molecule Detection Limits In Levitated Microdroplets. *Analytical Chemistry* **1991**, 63, (10), 1027-1031.
33. Bopp, M. A.; Meixner, A. J.; Tarrach, G.; ZschokkeGranacher, I.; Novotny, L., Direct imaging single molecule diffusion in a solid polymer host. *Chemical Physics Letters* **1996**, 263, (6), 721-726.
34. Dickson, R. M.; Norris, D. J.; Tzeng, Y. L.; Moerner, W. E., Three-dimensional imaging of single molecules solvated in pores of poly(acrylamide) gels. *Science* **1996**, 274, (5289), 966-969.
35. Ruiter, A. G. T.; Veerman, J. A.; GarciaParajo, M. F.; vanHulst, N. F., Single molecule rotational and translational diffusion observed by near-field scanning optical microscopy. *Journal of Physical Chemistry A* **1997**, 101, (40), 7318-7323.

36. Schmidt, T.; Schutz, G. J.; Baumgartner, W.; Gruber, H. J.; Schindler, H., Imaging of single molecule diffusion. *Proceedings of the National Academy of Sciences of the United States of America* **1996**, 93, (7), 2926-2929.
37. Schutz, G. J.; Schindler, H.; Schmidt, T., Single-molecule microscopy on model membranes reveals anomalous diffusion. *Biophysical Journal* **1997**, 73, (2), 1073-1080.
38. Xu, X. H.; Yeung, E. S., Direct measurement of single-molecule diffusion and photodecomposition in free solution. *Science* **1997**, 275, (5303), 1106-1109.
39. Ambrose, W. P.; Goodwin, P. M.; Martin, J. C.; Keller, R. A., Single-Molecule Detection And Photochemistry On A Surface Using Near-Field Optical-Excitation. *Physical Review Letters* **1994**, 72, (1), 160-163.
40. Betzig, E.; Chichester, R. J., Single Molecules Observed By Near-Field Scanning Optical Microscopy. *Science* **1993**, 262, (5138), 1422-1425.
41. Macklin, J. J.; Trautman, J. K.; Harris, T. D.; Brus, L. E., Imaging and time-resolved spectroscopy of single molecules at an interface. *Science* **1996**, 272, (5259), 255-258.
42. Trautman, J. K.; Macklin, J. J., Time-resolved spectroscopy of single molecules using near-field and far-field optics. *Chemical Physics* **1996**, 205, (1-2), 221-229.
43. Trautman, J. K.; Macklin, J. J.; Brus, L. E.; Betzig, E., Near-Field Spectroscopy Of Single Molecules At Room-Temperature. *Nature* **1994**, 369, (6475), 40-42.
44. Xie, X. S.; Dunn, R. C., Probing Single-Molecule Dynamics. *Science* **1994**, 265, (5170), 361-364.
45. Nie, S. M.; Chiu, D. T.; Zare, R. N., Probing Individual Molecules With Confocal Fluorescence Microscopy. *Science* **1994**, 266, (5187), 1018-1021.
46. Nie, S. M.; Chiu, D. T.; Zare, R. N., Real-Time Detection Of Single-Molecules In Solution By Confocal Fluorescence Microscopy. *Analytical Chemistry* **1995**, 67, (17), 2849-2857.
47. Trabesinger, W.; Schutz, G. J.; Gruber, H. J.; Schindler, H.; Schmidt, T., Detection of individual oligonucleotide pairing by single-molecule microscopy. *Analytical Chemistry* **1999**, 71, (1), 279-283.
48. Wirth, M. J.; Swinton, D. J., Single-Molecule Probing of Mixed-Mode Adsorption at a Chromatographic Interface. *Analytical Chemistry* **1998**, 70, (24), 5264-5271.

49. Dickson, R. M.; Cubitt, A. B.; Tsien, R. Y.; Moerner, W. E., On/off blinking and switching behaviour of single molecules of green fluorescent protein. *Nature* **1997**, 388, (6640), 355-358.
50. Jung, G.; Wiehler, J.; Gohde, W.; Tittel, J.; Basche, T.; Steipe, B.; Brauchle, C., Confocal microscopy of single molecules of the green fluorescent protein. *Bioimaging* **1998**, 6, (1), 54-61.
51. Panzer, O.; Gohde, W.; Fischer, U. C.; Fuchs, H.; Mullen, K., Influence of oxygen on single molecule blinking. *Advanced Materials* **1998**, 10, (17), 1469-1472.
52. Yip, W. T.; Hu, D. H.; Yu, J.; Vanden Bout, D. A.; Barbara, P. F., Classifying the photophysical dynamics of single- and multiple-chromophoric molecules by single molecule spectroscopy. *Journal of Physical Chemistry A* **1998**, 102, (39), 7564-7575.
53. Yokota, H.; Ishii, Y.; Yanagida, T., Blinking and its effect on single molecule FRET measurements. *Biophysical Journal* **2001**, 80, (1), 150A-150A.
54. Klodzinska, E.; Moravcova, D.; Jandera, P.; Buszewski, B., Monolithic continuous beds as a new generation of stationary phase for chromatographic and electro-driven separations. *Journal of Chromatography A* **2006**, 1109, (1), 51-59.
55. Kroeff, E. P.; Owens, R. A.; Campbell, E. L.; Johnson, R. D.; Marks, H. I., Production Scale Purification Of Biosynthetic Human Insulin By Reversed-Phase High-Performance Liquid-Chromatography. *Journal of Chromatography* **1989**, 461, 45-61.
56. Gritti, F.; Guiochon, G., Physical origin of peak tailing on C18-bonded silica in reversed-phase liquid chromatography. *Journal of Chromatography, A* **2004**, 1028, (1), 75-88.
57. McCalley, D. V., Effect of buffer on peak shape of peptides in reversed-phase high performance liquid chromatography. *Journal of Chromatography, A* **2004**, 1038, (1-2), 77-84.
58. McCalley, D. V., Study of overloading of basic drugs and peptides in reversed-phase high-performance liquid chromatography using pH adjustment of weak acid mobile phases suitable for mass spectrometry. *Journal of Chromatography, A* **2005**, 1075, (1-2), 57-64.
59. Sunseri, J. D.; Cooper, W. T.; Dorsey, J. G., Reducing residual silanol interactions in reversed-phase liquid chromatography - Thermal treatment of silica before derivatization. *Journal of Chromatography A* **2003**, 1011, (1-2), 23-29.

60. Neue, U. D.; Phoebe, C. H.; Tran, K.; Cheng, Y.-F.; Lu, Z., Dependence of Reversed-Phase Retention of Ionizable Analytes on pH, Concentration of Organic Solvent and Silanol Activity. *J. Chromatography A* **2001**, 925, 49-67.
61. Stanley, B. J.; Krance, J.; Roy, A., Determination of the thermodynamic contribution to peak asymmetry of basic solutes in reversed-phase liquid chromatography. *Journal of Chromatography A* **1999**, 865, (1-2), 97-109.
62. Kohler, J.; Chase, B. D.; Farlee, R. D.; Vega, A. J.; Kirkland, J. J., Comprehensive Characterization of Some Silica-Based Stationary Phases for High-Performance Liquid Chromatography. *Journal of Chromatography* **1986**, 352, 275-305.
63. Kohler, J.; Kirkland, J. J., Improved Silica-Based Column Packings for High-Performance Liquid-Chromatography. *Journal of Chromatography* **1987**, 385, 125-150.
64. Wirth, M. J.; Swinton, D. J.; Ludes, M. D., Adsorption and Diffusion of Single Molecules at Chromatographic Interfaces. *Journal of Physical Chemistry B* **2003**, 107, (26), 6258-6268.
65. Smith, E. A.; Wirth, M. J., pH dependence of tailing in reversed-phase chromatography of a cationic dye: measurement of the strong adsorption site surface density. *Journal of Chromatography, A* **2004**, 1060, (1-2), 127-134.
66. Hansen, R. L.; Harris, J. M., Total internal reflection fluorescence correlation spectroscopy for counting molecules at solid/liquid interfaces. *Analytical Chemistry* **1998**, 70, (13), 2565-2575.
67. Elson, E. L.; Magde, D., Fluorescence Correlation Spectroscopy .1. Conceptual Basis And Theory. *Biopolymers* **1974**, 13, (1), 1-27.
68. Magde, D.; Elson, E. L.; Webb, W. W., Fluorescence Correlation Spectroscopy .2. Experimental Realization. *Biopolymers* **1974**, 13, (1), 29-61.
69. Magde, D.; Webb, W. W.; Elson, E., Thermodynamic Fluctuations In A Reacting System - Measurement By Fluorescence Correlation Spectroscopy. *Physical Review Letters* **1972**, 29, (11), 705-&.
70. Brand, L.; Eggeling, C.; Zander, C.; Drexhage, K. H.; Seidel, C. A. M., Single-molecule identification of Coumarin-120 by time-resolved fluorescence detection: Comparison of one- and two-photon excitation in solution. *Journal of Physical Chemistry A* **1997**, 101, (24), 4313-4321.
71. Fan, F. R. F.; Kwak, J.; Bard, A. J., Single molecule electrochemistry. *Journal of the American Chemical Society* **1996**, 118, (40), 9669-9675.

72. Guenard, R. D.; King, L. A.; Smith, B. W.; Winefordner, J. D., Two-channel sequential single molecule measurement. *Analytical Chemistry* **1997**, 69, (13), 2426-2433.
73. Haab, B. B.; Mathies, R. A., Single-Molecule Fluorescence Burst Detection Of Dna Fragments Separated Capillary Electrophoresis. *Analytical Chemistry* **1995**, 67, (18), 3253-3260.
74. Kettner, R.; Tittel, J.; Basche, T.; Brauchle, C., Optical Spectroscopy And Spectral Diffusion Of Single Dye Molecules In Amorphous Spin-Coated Polymer-Films. *Journal of Physical Chemistry* **1994**, 98, (27), 6671-6674.
75. Soper, S. A.; Shera, E. B.; Martin, J. C.; Jett, J. H.; Hahn, J. H.; Nutter, H. L.; Keller, R. A., Single-Molecule Detection Of Rhodamine-6g In Ethanolic Solutions Using Continuous Wave Laser Excitation. *Analytical Chemistry* **1991**, 63, (5), 432-437.
76. Talon, H.; Fleury, L.; Bernard, J.; Orrit, M., Fluorescence Excitation Of Single Molecules. *Journal of the Optical Society of America B-Optical Physics* **1992**, 9, (5), 825-828.
77. Wirth, M. J.; Ludes, M. D.; Swinton, D. J., Analytic solution to the autocorrelation function for lateral diffusion and rare strong adsorption. *Applied Spectroscopy* **2001**, 55, (6), 663-669.
78. Ludes, M. D.; Anthony, S. R.; Wirth, M. J., Fluorescence Imaging of the Desorption of Dye from Fused Silica versus Silica Gel. *Analytical Chemistry* **2003**, 75, (13), 3073-3078.
79. Ludes, M. D.; Wirth, M. J., Single-molecule resolution and fluorescence imaging of mixed-mode sorption of a dye at the interface of C18 and acetonitrile/water. *Analytical Chemistry* **2002**, 74, (2), 386-393.
80. Dokou, E.; Zhang, L. P.; Barteau, M. A., Comparison of atomic force microscopy imaging methods and roughness determinations for a highly polished quartz surface. *Journal of Vacuum Science & Technology B* **2002**, 20, (6), 2183-2186.
81. Zhong, Z. M.; Lowry, M.; Wang, G. F.; Geng, L., Probing strong adsorption of solute onto cis-silica gel by fluorescence correlation imaging and single-molecule spectroscopy under RPLC conditions. *Analytical Chemistry* **2005**, 77, (8), 2303-2310.
82. Bardo, A. M.; Collinson, M. M.; Higgins, D. A., Nanoscale properties and matrix-dopant interactions in dye-doped organically modified silicate thin films. *Chemistry of Materials* **2001**, 13, (8), 2713-2721.

83. Fu, Y.; Ye, F. M.; Sanders, W. G.; Collinson, M. M.; Higgins, D. A., Single molecule spectroscopy studies of diffusion in mesoporous silica thin films. *Journal of Physical Chemistry B* **2006**, 110, (18), 9164-9170.
84. Higgins, D. A.; Collinson, M. M., Gaining insight into the nanoscale properties of sol-gel-derived silicate thin films by single-molecule spectroscopy. *Langmuir* **2005**, 21, (20), 9023-9031.
85. Higgins, D. A.; Collinson, M. M.; Saroja, G.; Bardo, A. M., Single-molecule spectroscopic studies of nanoscale heterogeneity in organically modified silicate thin films. *Chemistry of Materials* **2002**, 14, (9), 3734-3744.
86. McCain, K. S.; Hanley, D. C.; Harris, J. M., Single-molecule fluorescence trajectories for investigating molecular transport in thin silica sol-gel films. *Analytical Chemistry* **2003**, 75, (17), 4351-4359.
87. Mei, E.; Bardo, A. M.; Collinson, M. M.; Higgins, D. A., Single-molecule studies of sol-gel-derived silicate films. Microenvironments and film-drying conditions. *Journal of Physical Chemistry B* **2000**, 104, (43), 9973-9980.
88. Cabral, J. L.; Bandilla, D.; Skinner, C. D., Pore size characterization of monolith for electrochromatography via atomic force microscopy studies in air and liquid phase. *Journal of Chromatography A* **2006**, 1108, (1), 83-89.
89. Dondi, F.; Guiochon, G.; Editors, *Theoretical Advancement in Chromatography and Related Separation Techniques. (Proceedings of the NATO Advanced Study Institute on Theoretical Advancement in Chromatography and Related Separation Techniques, Ferrara, Italy, August 18-30, 1991.)* [In: *NATO ASI Ser., Ser. C*, 1993; 383]. 1992; 640 pp.
90. Koehler, J.; Kirkland, J. J., Improved silica-based column packings for high-performance liquid chromatography. *Journal of Chromatography* **1987**, 385, 125-50.
91. Iler, R. K.; Kirkland, J. J. Macroporous microspheroids and a process for their manufacture. United States Patent 4070286, 1978.
92. Miguez, H.; Meseguer, F.; Lopez, C.; Mifsud, A.; Moya, J. S.; Vazquez, L., Evidence of FCC crystallization of SiO<sub>2</sub> nanospheres. *Langmuir* **1997**, 13, (23), 6009-6011.
93. Jiang, P.; Bertone, J. F.; Hwang, K. S.; Colvin, V. L., Single-crystal colloidal multilayers of controlled thickness. *Chemistry of Materials* **1999**, 11, (8), 2132-2140.

94. Bertone, J. F.; Jiang, P.; Hwang, K. S.; Mittleman, D. M.; Colvin, V. L., Thickness dependence of the optical properties of ordered silica-air and air-polymer photonic crystals. *Physical Review Letters* **1999**, 83, (2), 300-303.
95. Koenderink, A. F.; Johnson, P. M.; Lopez, J. F. G.; Vos, W. L., Three-dimensional photonic crystals as a cage for light. *Comptes Rendus Physique* **2002**, 3, (1), 67-77.
96. Brozell, A. M.; Muha, M. A.; Sanii, B.; Parikh, A. N., A class of supported membranes: Formation of fluid phospholipid bilayers on photonic band gap colloidal crystals. *Journal of the American Chemical Society* **2006**, 128, (1), 62-63.
97. Zheng, S. P.; Zhang, H.; Ross, E.; Van Le, T.; Wirth, M. J., Silica colloidal crystals for enhanced fluorescence detection in microarrays. *Analytical Chemistry* **2007**, 79, (10), 3867-3872.
98. Choi, W. M.; Park, O. O., Micropatterns of colloidal assembly on chemically patterned surface. *Colloids And Surfaces A-Physicochemical And Engineering Aspects* **2006**, 277, (1-3), 131-135.
99. Park, J.; Moon, J.; Shin, H.; Wang, D.; Park, M., Direct-write fabrication of colloidal photonic crystal microarrays by ink-jet printing. *Journal of Colloid and Interface Science* **2006**, 298, (2), 713-719.
100. Das, M.; Zhang, H.; Kumacheva, E., Microgels: Old materials with new applications. *Annual Review Of Materials Research* **2006**, 36, 117-142.
101. Newton, M. R.; Bohaty, A. K.; White, H. S.; Zharov, I., Chemically modified opals as thin permselective nanoporous membranes. *Journal Of The American Chemical Society* **2005**, 127, (20), 7268-7269.
102. Newton, M. R.; Morey, K. A.; Zhang, Y. H.; Snow, R. J.; Diwekar, M.; Shi, J.; White, H. S., Anisotropic diffusion in face-centered cubic opals. *Nano Letters* **2004**, 4, (5), 875-880.
103. Zeng, Y.; Harrison, D. J., Self-Assembled Colloidal Arrays as Three-Dimensional Nanofluidic Sieves for Separation of Biomolecules on Microchips. *Analytical Chemistry* **2007**, 79, 2289 - 2295.
104. Zheng, S.; Ross, E.; Legg, M. A.; Wirth, M. J., High-speed electroseparations inside silica colloidal crystals. *Journal of the American Chemical Society* **2006**, 128, (28), 9016-9017.

105. Cichelli, J.; Zharov, I., Chiral Permselectivity in Surface-Modified Nanoporous Opal Films. *Journal of the American Chemical Society* **2006**, 128, (25), 8130-8131.
106. Zhang, J.; Gassmann, M.; He, W. D.; Wan, F.; Chu, B., Reversible thermo-responsive sieving matrix for oligonucleotide separation. *Lab On A Chip* **2006**, 6, (4), 526-533.
107. Schepelina, O.; Zharov, I., Polymer-modified opal nanopores. *Langmuir* **2006**, 22, (25), 10523-10527.
108. Koehler, J.; Chase, D. B.; Farlee, R. D.; Vega, A. J.; Kirkland, J. J., Comprehensive characterization of some silica-based stationary phases for high-performance liquid chromatography. *Journal of Chromatography* **1986**, 352, 275-305.
109. Kohr, J.; Engelhardt, H., Characterization Of Quartz Capillaries For Capillary Electrophoresis. *Journal Of Chromatography A* **1993**, 652, (2), 309-316.
110. Chabanov, A. A.; Jun, Y.; Norris, D. J., Avoiding cracks in self-assembled photonic band-gap crystals. *Applied Physics Letters* **2004**, 84, (18), 3573-3575.
111. Garcia-Santamaria, F.; Miguez, H.; Ibisate, M.; Meseguer, F.; Lopez, C., Refractive index properties of calcined silica submicrometer spheres. *Langmuir* **2002**, 18, (5), 1942-1944.
112. Huang, X.; Doneski, L. J.; Wirth, M. J., Surface-Confined Living Radical Polymerization for Coatings in Capillary Electrophoresis. *Analytical Chemistry* **1998**, 70, (19), 4023-4029.
113. Huang, X.; Wirth, M. J., Surface-Initiated Radical Polymerization on Porous Silica. *Analytical Chemistry* **1997**, 69, (22), 4577-4580.
114. Huang, X.; Wirth, M. J., Surface Initiation of Living Radical Polymerization for Growth of Tethered Chains of Low Polydispersity. *Macromolecules* **1999**, 32, (5), 1694-1696.
115. Xiao, D.; Wirth, M. J., Kinetics of Surface-Initiated Atom Transfer Radical Polymerization of Acrylamide on Silica. *Macromolecules* **2002**, 35, (8), 2919-2925.
116. Li, W. B.; Segre, P. N.; Gammon, R. W.; Sengers, J. V.; Lamvik, M., Determination Of The Temperature And Concentration-Dependence Of The Refractive-Index Of A Liquid-Mixture. *Journal Of Chemical Physics* **1994**, 101, (6), 5058-5069.



117. Mittleman, D. M.; Bertone, J. F.; Jiang, P.; Hwang, K. S.; Colvin, V. L., Optical properties of planar colloidal crystals: Dynamical diffraction and the scalar wave approximation. *Journal of Chemical Physics* **1999**, 111, (1), 345-354.
118. Huang, X. Y.; Doneski, L. J.; Wirth, M. J., Surface-confined living radical polymerization for coatings in capillary electrophoresis. *Analytical Chemistry* **1998**, 70, (19), 4023-4029.
119. Huang, X. Y.; Wirth, M. J., Surface-initiated radical polymerization on porous silica. *Analytical Chemistry* **1997**, 69, (22), 4577-4580.
120. *Polymer handbook*. CRC Press: 1995.
121. Williams, J. M.; Han, T. J.; Beebe, T. P., Determination of single-bond forces from contact force variances in atomic force microscopy. *Langmuir* **1996**, 12, (5), 1291-1295.
122. Goponenko, A. V.; Asher, S. A., Modeling of stimulated hydrogel volume changes in photonic crystal Pb<sup>2+</sup> sensing materials. *Journal of the American Chemical Society* **2005**, 127, (30), 10753-10759.
123. Jacobson, S. C.; Culbertson, C. T.; Daler, J. E.; Ramsey, J. M., Microchip structures for submillisecond electrophoresis. *Analytical Chemistry* **1998**, 70, (16), 3476-3480.
124. Plenert, M. L.; Shear, J. B., Microsecond electrophoresis. *Proceedings of the National Academy of Sciences of the United States of America* **2003**, 100, (7), 3853-3857.
125. MacNair, J. E.; Patel, K. D.; Jorgenson, J. W., Ultrahigh pressure reversed-phase capillary liquid chromatography: Isocratic and gradient elution using columns packed with 1.0- $\mu$ m particles. *Analytical Chemistry* **1999**, 71, (3), 700-708.
126. Luo, Q. Z.; Shen, Y. F.; Hixson, K. K.; Zhao, R.; Yang, F.; Moore, R. J.; Mottaz, H. M.; Smith, R. D., Preparation of 20- $\mu$ m-i.d. silica-based monolithic columns and their performance for proteomics analyses. *Analytical Chemistry* **2005**, 77, (15), 5028-5035.
127. Leinweber, F. C.; Lubda, D.; Cabrera, K.; Tallarek, U., Characterization of silica-based monoliths with bimodal pore size distribution. *Analytical Chemistry* **2002**, 74, (11), 2470-2477.
128. Xie, S.; Allington, R. W.; Svec, F.; Frechet, J. M. J., Rapid reversed-phase separation of proteins and peptides using optimized 'moulded' monolithic poly(styrene-co-divinylbenzene) columns. *Journal of Chromatography A* **1999**, 865, (1-2), 169-174.

129. Vegavri, A.; Guttman, A., Theoretical and nomenclatural considerations of capillary electrochromatography with monolithic stationary phases. *Electrophoresis* **2006**, 27, (3), 716-725.